Numerical Models of Lithosphere Removal in the Sierra Nevada de Santa Marta, Colombia

by

David Quiroga

A thesis submitted in partial fulfillment of the requirements for the degree of

Master of Science

in

Geophysics

Department of Physics

University of Alberta

Abstract

The Sierra Nevada de Santa Marta (SNSM) in northern Colombia, is one of the highest coastal mountains in the world with a maximum height of more than 5.7 km. Geophysical measurements report that there is a high Bouguer gravity anomaly (>+130 mGal) in the region, indicating that the mountain does not have a crustal root. Previous studies attributed the support of the mountain to the underthrusting buoyant Caribbean plateau or to elastic stresses within the continental lithosphere. However, thermo-chronological studies report a recent uplift episode (in the last 2 Ma) that does not have a clear driving force. This thesis proposes that this region experienced a localized lithosphere removal event, whereby the dense lower lithosphere sank into the mantle as a drip, resulting a thin crust and lithosphere and causing surface uplift.

To test this hypothesis, 2D and 3D numerical models are developed using the software ASPECT. The models examine the dynamics of a lithosphere drip and the associated observations, including surface topography, gravity anomaly and surface heat flow. The general model setup has a four-layer structure consisting of an upper crust, lower crust, mantle lithosphere and sublithospheric mantle. There is an initially thickened crust in the middle of the domain, representing the SNSM. This induces a perturbation in the lower lithosphere which is gravitationally unstable and undergoes foundering. The first 2D models are used to define a reference setup, by testing the effect of initial crustal root thickness, lateral compression rate, perturbation width, and plastic rheology parameters. Subsequent 2D models consist of modifications of the reference and explore the effects of crustal root eclogitization, lithosphere rheology, upper crustal density, initial crustal thickness and lateral compression. In the preferred 2D model, the surface first undergoes subsidence, but post-removal non-isostatic forces induce uplift rates above 0.2 mm/yr for about 1 Ma, holding a region of high topography (3.3 km) and a maximum positive Bouguer gravity anomaly of +103 mGal, consistent with SNSM observations. Additional calculations show that lithosphere removal generates a low seismic wave velocity anomaly under the Moho (-5% and -8% for V_s and V_p, respectively) and potentially inducing lower crustal and upper mantle melting. The final set of models uses a simplified 3D geometry with a perturbation in the mantle lithosphere but without an initially thickened crust to show that a 3D drip is wider and is associated with up to 66% less subsidence and positive gravity anomalies that are up to 112% higher than an equivalent 2D model.

The models show that lithosphere removal is a viable explanation for the origin of the SNSM. The removal event could have occurred either very recently (<2 Ma ago), potentially explaining a recent uplift episode, or earlier (50-40 Ma ago), possibly affecting the Paleocene-Eocene magmatism in this region, if phenomena that have not been considered in the models (e.g., elastic support, support from the Caribbean slab) can maintain the high elevation and gravity anomaly to the present. In either case, lithosphere removal would have affected the continental lithosphere structure. This work shows that local lithosphere geodynamics may have played an important role in the geological history of the SNSM, northern Colombia, and the Caribbean. The insights and quantitative predictions from the numerical models provide

important constraints for future studies of this complex region.

Acknowledgments

Research supported by an NSERC Discovery Grant. Models were run thanks to the resources provided by WestGrid (www.westgrid.ca) and Compute Canada (www.computecanada.ca). Special thanks to the Computational Infrastructure for Geodynamics (geodynamics.org) which is funded by the National Science Foundation under award EAR-0949446 and EAR-1550901 for supporting the development of ASPECT.

Contents

List of Tables

List of Figures

Chapter 1: Introduction

1.1 An Unusual Mountain in Northern Colombia

The Sierra Nevada de Santa Marta (SNSM) in northern Colombia is one of the highest coastal mountains in the world, with a maximum height of about 5.7 km (Figure 1.1*a*). This triangular shaped mountain range is isolated from the rest of the Andes Cordillera, and yet it has the highest peak in the Colombian territory. Early geophysical observations in the region have shown that there is an atypical Bouguer gravity anomaly of more than +130 mGal in the area (e.g., Case and Macdonald, 1973) (Figure 1.1*b*). This is unexpected because the crustal root that normally compensates the load of high mountains should produce a negative gravity anomaly. Consequently, some authors agree that the massif must lack isostatic balance missing an Airy-type crustal root (e.g., Ceron-Abril, 2008; Montes et al., 2005; Villagómez et al., 2011). This then raises questions about how the high elevation massif is mechanically supported and why is there no crustal root.

In some studies, it has been proposed that the southward underthrusting of the buoyant Caribbean plateau and oceanic seamounts could provide support for the topography (e.g., Case and Macdonald, 1973; Montes et al., 2005). Case and Macdonald (1973) suggest that the crust must be relatively thin, and that there is an excess of mass under the mountain, suggesting that the lower crust or mantle should be unusually close to the surface. On the other hand, Montes et al. (2005) propose that the force of the Caribbean slab could create upward displacement of the interface between the crust and the mantle (i.e., the continental Moho), generating the gravity anomaly. The latter authors agree that there must be no crustal root under the massif, and that an unexpectedly thin crust is required to explain the magnitude of the Bouguer gravity anomaly. For example, Montes et al. (2005) suggest that 8 km of Moho relief relative to adjacent areas would account for the gravity anomaly observed.

Later, Arnaiz-Rodríguez and Audemard (2014) proposed that the high topography may be due to a rigid and strong lithosphere based on elastic thickness estimations in the Maracaibo block (MB), which is the region enclosed by the Oca Fault (OF) and the Santa Marta - Bucaramanga fault (SMBF) in the lower right zone in Figure 1.1*a*, it extends further towards Venezuela, and is bounded at the east by the Boconó fault. For instance, Arnaiz-Rodríguez and Audemard (2014) estimate elastic thickness values of more than 26 km in the region of the SNSM. This agrees with elastic thickness calculations in South America by Tassara et al. (2007), which report values of 30 to 40 km in northern Colombia. However, while the presence of a rigid lithosphere could provide mechanical support, it does not explain the high magnitude positive Bouguer gravity anomaly, meaning that there must be an additional phenomenon accounting for an excess of mass.

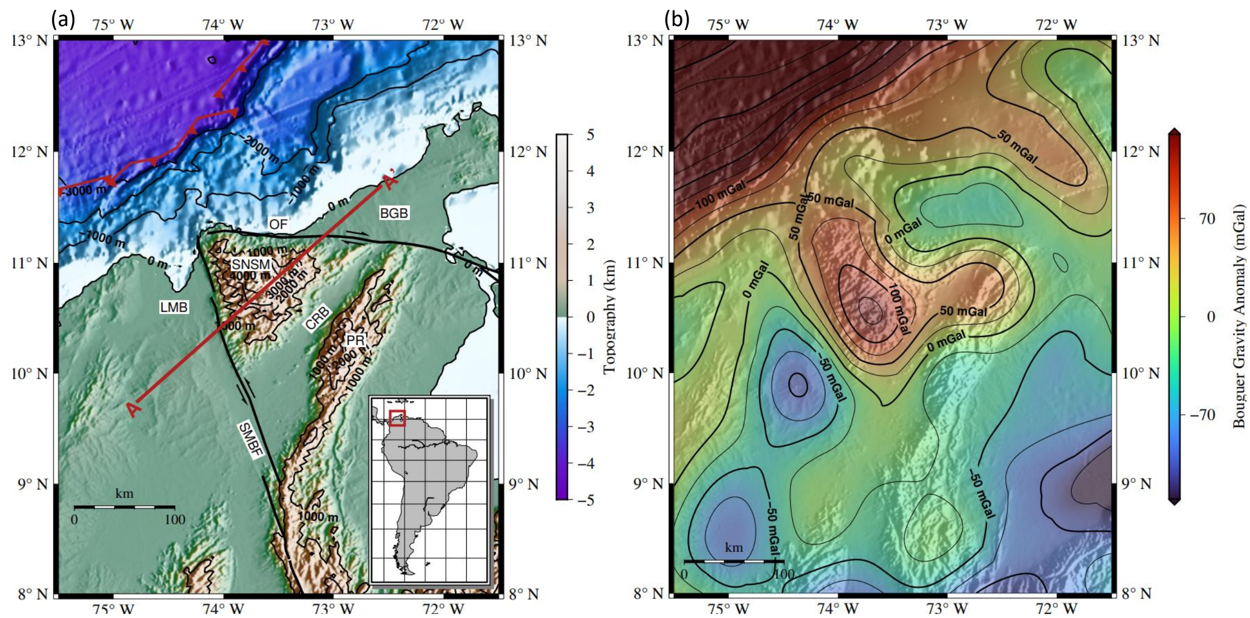

Figure 1.1: (a) Topographic map of the study region in northern Colombia. Profiles of topography and gravity anomaly from A to A′ are used to compare the models with observations. BGB: Baja Guajira Basin, OF: Oca Fault, SNSM: Sierra Nevada de Santa Marta, LMB: Lower Magdalena Basin, CRB: Cesar-Rancheria Basin, PR: Perijá Range, SMBF: Santa Marta-Bucaramanga Fault. (b) Bouguer gravity anomaly map from the EIGEN-GL04C Global gravity field model (Förste et al., 2008).

Moreover, studies by Quintero et al. (2019), Salazar et al. (2017), and Vargas et al. (2009), suggest that the lithosphere is relatively hot. This is supported by observations of high surface heat flow in the region. For example, Quintero et al. (2019) report a surface heat flow of 60 to 80 $\frac{mW}{m^2}$, and Sanchez-Rojas and Palma (2014) state that the massif is characterized by a heat flow of more than 100 $\frac{mW}{m^2}$. Aside, crustal thickness estimations reported by Sanchez-Rojas and Palma (2014), coupling deep wide-angle seismic refraction sections, Moho depth from receiver functions, and surface geology, suggest a locally thin crust in the SNSM region (i.e., <35 km). For instance, surface heat flow would be enhanced if the SNSM lithosphere is thin and underlain by hot sub-lithospheric mantle. Conversely, low surface heat flow would be expected if the SNSM is directly underlain by an underthrusting Caribbean slab, which could be thermally insulating. Additionally, Villagómez et al. (2011) report a recent and fast uplift episode (about 2 Ma ago) which is not correlated with a major tectonic event and does not have an identified driving force. This implies that there must be an additional mechanism producing vertical motions in the region.

This thesis explores the idea that the above observations can be explained by gravitational lithosphere thinning. Lithospheric dripping is considered because it is a mechanism that is known to drive surface uplift, producing symmetric topographies (e.g., Göğüş and Pysklywec, 2008; Wang and Currie, 2017; Wang et al., 2014) and could simultaneously result in lithospheric or crustal thinning. This mechanism has been proposed to explain unusual surface expressions in various mountain ranges such as the Canadian Cordillera (western Canada) and the Sierra Nevada California (e.g., Bao et al., 2014; Saleeby et al., 2012). Lithosphere removal via drips occurs through the downward growth of perturbations in cold and dense mantle lithosphere. It can be generated during crustal shortening (Houseman et al., 1981) or by the gravitational instability of magmatic/metamorphic eclogite present in crustal roots (Wang et al., 2014). Because the SNSM region has been subjected to significant shortening, crustal thickening could have fostered metamorphic crustal root eclogitization, simultaneously producing a mantle lithosphere instability. Furthermore, as shown below, this region experienced arc magmatism in the past and therefore the high-density eclogites/arclogites would make the crustal root prone to founder, explaining its absence. By removing the dense lower lithosphere, this mechanism could provide the driving force for recent uplift in the SNSM, providing at the same time additional dynamic support for the high elevations.

This study includes both 2D and 3D numerical models to investigate if the local observations of surface topography, gravity anomaly, and surface heat flow can be explained by lithosphere removal. Firstly, since a key part of this study is to compare model predictions of the gravity anomaly with observed data, a modelling method to estimate the Bouguer gravity anomaly of 2D density structures is developed and tested.

The first models consist of simple drips triggered by a convective instability in 2D. In this case, there is a downward growth of a perturbation in the interface between two layers in which the denser material sinks. The latter models explore the overall drip dynamics and the effect of the advection mechanism of the modelling software on the gravity anomaly calculations. Further parameter tests in a 2D geometry are included to find a suitable setup to produce realistic models of lithosphere removal. These tests assume that previous shortening produced lithosphere thickening in the region of the mountain, resulting in an initially thickened crustal fragment and an instability in the mantle lithosphere. The models include tests of the initial thickness of the crustal root, rate of lateral compression, width of the mountain region, and the configuration for a viscous-plastic rheology. These results are used to produce 2D models of lithosphere removal for the SNSM studying the effect of different lithosphere rheologies and the density of crustal rocks in the mountain region. Additionally, because crustal thickness has a significant effect on the gravity anomaly, and because the latter is strongly dependent on the initial thickness and the subsequent amount of lateral compression (and shortening), systematic tests of these parameters are included to understand their effects. Subsequent post processing includes calculations of the non-isostatic topography (isolating the dynamic contribution to surface deflections), and estimations for melting patterns and seismic wave velocities in the upper mantle, as other observations that could be used to identify lithosphere removal. Finally, a set of 3D models explore limitations of the use of 2D modelling geometries for a 3D setting such as the SNSM. The models presented examine the role of lithosphere elasticity and shallow frictional-plastic deformation patters produced by a 3D drip. The complete set of models in this work, provide valuable constraints and insights that could be useful to determine if there has been a lithosphere removal episode in the region of the SNSM, and also provide insights into the surface expressions of lithosphere removal that may be applicable to other areas.

1.2 Geologic/Tectonic Background

This section provides a summary of the geology and tectonics of the study area. The SNSM is part of the larger crustal fragment known as the Maracaibo block (MB). Its NW corner is $\sim$100 km away from the tectonic margin between the Caribbean and South American plates. At the present, there is oblique convergence oriented to the South East at a rate of 10-20 mm/year, producing underthrusting and shallow subduction of the Caribbean plate under South America. For example, Freymueller et al. (1993) report a rate of 17mm/year, with components of $\pm$7mm/year to the South and $\pm$10mm/year to the East. Regional seismological studies agree that the Caribbean plate subducts (or underthrusts) the South American plate at a shallow angle ($<30°$) (suggesting a region of flat slab subduction), and then steepens at some point into the continent (e.g., Cornthwaite et al., 2021; Londoño et al., 2020; Taboada et al., 2000; Van Der Hilst and Mann, 1994; Vargas, 2020).

The SNSM massif is bounded by major faults and basins (Figure 1.1*a*). At the north, the SNSM is limited by the right lateral Oca fault and the Baja Guajira basin. At the southwest, it is bounded by the left lateral Santa Marta-Bucaramanga fault and the Lower Magdalena basin. Finally, to the southeast, it is bounded by the Cesar-Rancheria basin and the Perijá range. The Santa Marta-Bucaramanga and Oca faults exceed 200 km in length and have experienced significant lateral displacements since the Paleocene (110 km and 65 km, respectively), followed by significant vertical displacements (e.g., Case and Macdonald, 1973; Tschanz et al., 1974), while the surrounding basins have stored sediments that were eroded from the mountain (e.g., Bayona et al., 2011).

The SNSM is commonly divided into three geo-tectonic provinces following the separation proposed by Tschanz et al. (1974). These are: The Sierra Nevada, Sevilla, and Santa Marta provinces. According to Ramírez et al. (2020), the older rocks in the SNSM are located in both the Sevilla province (The Buriticá and Los Muchachitos gneisses) and the Sierra Nevada province (Los Mangos granulite and Dibulla gneiss), constituting the Precambrian metamorphic basement, which is often referred to as the Grenvillian basement (e.g., Sanchez and Mann, 2015).

The basement is overlain by Paleozoic metamorphic and sedimentary units (e.g., El Encanto orthogneiss and the Devonian-Carboniferous sequences of Cuchilla de Carbonal, respectively) and late Triassic-Early Jurassic sedimentary rocks (e.g., Los Indios formation). As noted by Tschanz et al. (1974), the latter rocks are mostly covered by outcropping Jurassic igneous bodies, for which Ramírez et al. (2020) reported intermediate to felsic compositions and mafic intrusions. The results in Quandt et al. (2018) show that these are continental arc plutons, indicating a Jurassic magmatic arc.

The evolution of NW South America after the Late Cretaceous was significantly influenced by the collision of the Caribbean large igneous province with South America, which according to Spikings et al. (2015), started 75 Ma ago. Generally, it is agreed that this was a diachronous collision that continued progressively towards the north during the westward displacement of the South American plate relative to the Caribbean plate (e.g., Bayona et al., 2011; Pindell and Dewey, 1982; Pindell et al., 2005; Pindell et al., 2006). This collision was followed by the onset of the shallow subduction of the Caribbean plate under Northern South America in the early Paleocene (Villagómez et al., 2011). This produced magmatism in the NW corner of the SNSM, forming the Santa Marta batholith and other arc-type plutons (Cardona et al., 2010). The latter magmatic bodies intrude the Santa Marta metamorphic belt and together these form the Santa Marta province (Tschanz et al., 1974).

Villagómez et al. (2011) show that there has been a period of exhumation registered in the rock record with duration of ∼12.5 Ma at a rate above 0.5 mm/yr after the late Eocene for which it is difficult to assign a driving force. Moreover, Villagómez et al. (2011) conclude that there must have been very fast and recent uplift (in the previous 2 Ma) producing the observed topographies in the SNSM because, while it is located in a highly erosive region where high exhumation is expected, there is absence of exhumation in the last 16 Ma. The latter indicates that there must be an additional mechanism that produced recent uplift without allowing enough time for erosion to produce exhumation.

1.3 Objectives

The main purpose of this thesis is to test the hypothesis that the observations of high topography, positive Bouguer gravity anomaly and high surface heat flow in the region can be explained by an episode of lithosphere removal. This involves the accomplishment of the following objectives:

- Use numerical models to study the dynamics of lithosphere removal and obtain constraints for the magnitudes of topography, Bouguer gravity anomaly, surface heat flow, lithosphere rheology, characteristic deformation and uplift/subsidence rates produced by lithosphere removal in the context of the SNSM.

- Based on a comparison of model predictions with SNSM observations, provide time constrains for an episode of lithosphere removal in the SNSM, and the associated evolution of surface expressions.

- Use models to assess the seismic velocity structure and the associated melting patterns produced during and after lithosphere removal. These provide additional evidence that could be used in future studies to confirm if lithosphere removal has taken place in the study region.

- Explore differences in the surface expressions of lithosphere removal in 2D and 3D geometries to provide insights for the general dynamics of 3D lithosphere drips (and associated shallow deformation) because effects of 3D may be important for a localized region like the SNSM.

1.4 Thesis Outline

The first chapter of this work includes introductory remarks about the unexplained geological/geophysical observations in the region of the Sierra Nevada de Santa Marta (Colombia) that can potentially indicate recent lithosphere removal, and background information of the geologic and tectonic context of the study region. It also presents the objectives of this thesis.

Chapter 2 consists of the theoretical framework, including the governing equations and mathematical formulation for the numerical modelling codes used in this work, and the gravity anomaly modelling. The latter includes tests of the developed gravity anomaly algorithm with a previous modelling approach, and the theoretical solution for simple shapes.

Chapter 3 contains initial models of simple drips triggered by a convective instability in the mantle lithosphere, exploring their general behaviour, and implications of the advection strategy of the modelling software in the evolution of the modelled surface expressions.

Chapter 4 includes a set of models with parameter modifications to understand their effect and to find a suitable modelling setup with realistic parameters for a lithosphere drip. Parameter variations test the effect of the initial lithosphere thickness and width of the mountain region, lateral compression rate and the configuration to model brittle-plastic deformation.

Chapter 5 consists of numerical models of lithosphere removal for the study region, testing the effect of lithosphere rheology, crustal density, lateral compression rate and initial crustal root thickness. The purpose of these models is to study the evolution of surface observables of topography, Bouguer gravity anomaly and heat flow, and to understand the geological and geophysical implications of lithosphere removal for the SNSM. Results are compared and evaluated with respect to existing observations to determine if they can be explained by lithosphere removal.

Chapter 6 includes models of radially symmetric (axis-symmetric) drips in a 3D geometry triggered by a convective instability. These models explore the difference in dynamics and the resultant surface expressions of lithosphere removal between 2D and 3D drips. Also, models test the effect of crustal strength, elasticity and shallow plastic deformation in 3D drips.

Finally, chapter 7 includes the concluding remarks and recommendations for future work.

Chapter 2: Methodology

2.1 Mathematical Formulation

The models presented in this thesis are computed using the ASPECT code version 2.2.0 (Bangerth et al., 2020a) using the Boussinesq approximation formulation which assumes that variations in density are negligible except for their buoyancy effect. Additionally, 2D models assume plain strain conditions. The governing equations are incompressible mass conservation (2.1), momentum conservation (2.2), and the heat conservation (2.3) equations:

$$\nabla \cdot \mathbf{v} = 0 \tag{2.1}$$

$$-\nabla \cdot [2\eta\dot{\boldsymbol{\varepsilon}}] + \nabla P = -\alpha\rho_0\Delta T\mathbf{g} \tag{2.2}$$

$$\rho_0 C_p \left(\frac{\partial T}{\partial t} + \mathbf{v} \cdot \nabla T\right) - \nabla \cdot k\nabla T = \rho_0 H \tag{2.3}$$

where, $\mathbf{v}$ is the velocity field, P is the dynamic pressure, α is a constant thermal expansion coefficient, ρ_0 is the reference density, ΔT is the temperature difference relative to the reference temperature, $\mathbf{g}$ is the gravitational acceleration, C_p is the specific heat capacity, k is the thermal conductivity, H is the radiogenic heat production, $\dot{\boldsymbol{\varepsilon}}$ is the strain rate tensor:

$$\dot{\boldsymbol{\varepsilon}} = \frac{1}{2}\left(\nabla\mathbf{v} + \nabla\mathbf{v}^{\mathbf{T}}\right) \tag{2.4}$$

and η is an effective viscosity, which has a different formulation depending on the rheology assumed for the materials in the simulation (e.g., viscous Newtonian, viscous non-Newtonian, viscoplastic, viscoelastic) as explained in section 2.3. Note that equation 2.2 does not include the inertia term following the infinite Prandtl number approximation, which is commonly used in geodynamic models, considering that velocities in mantle convection occur over long timescales (millions of years) and mantle flows are characterized by a low Reynolds number. (See details in Gassmöller et al., 2020)

Additionally, materials are represented by compositional fields c_i, and their physical properties are displaced in space solving the advection equation (2.5) for each compositional field used (see details in Heister et al., 2017):

$$\frac{\partial c_i}{\partial t} + \mathbf{v} \cdot \nabla c_i = 0 \tag{2.5}$$

2.2 Theoretical framework

This thesis uses the previous mathematical formulation (in the ASPECT code) to model the dynamics of the lithosphere and upper mantle assuming that these are continuous media (materials do not have holes or void spaces). Consequently, motion within the continuum is restricted such that it only allows displacements that do not create voids. This behaviour is mathematically described by the mass conservation equation (2.1), implying that material displacements in any region of the medium should compensate one another to maintain its continuity. The assumption of a continuum results in a fluid-like mechanical behaviour that is suitable to model the mantle and lithosphere of the Earth because rocks behave like viscous fluids over long time scales (i.e., millions of years) (e.g., Schubert et al., 2001).

Numerical models constitute a discrete representation of physical properties (e.g., pressure, temperature, density, velocity, etc.) in a continuum, and their evolution in space and time according to a given set of initial and boundary conditions. Consequently, geodynamic simulations require modelling the driving forces that produce deformation within materials. The momentum conservation equation (2.2) provides a mathematical description of the force balance in each point of the continuous media, and accounts for the action of internal and external forces. However, the mechanical behaviour of rocks in the continuum and their dynamics is usually dependent on temperature-dependent physical properties such as density and viscosity. As a consequence, it is necessary to model the transport of heat and the way it affects temperature through its advection, conduction, and internal production. Based on the principle that energy is conserved in a closed system (such as the domain of a numerical model), heat transport is mathematically described by the equation of heat conservation (2.3). The whole system of equations (2.1-2.3) constitutes the theoretical framework of thermo-mechanical convection used in geodynamic numerical models of the Earth.

2.3 Lithosphere Rheology

2.3.1 Viscous Rheology

Rheology is the study of how materials deform or flow under applied stresses. A key step in geodynamic numerical modelling is to characterize rock rheology to model its deformation mechanisms. This thesis follows the common approach which assumes that rock deformation occurs through dislocation creep. This mechanism is dominant at high stresses, and consists of the non-reversible deformation of crystalline materials through the displacement of dislocations (or imperfections in the crystal lattice structure) inside the minerals that conform the rocks. This assumption dismisses other important rock deformation mechanisms such as diffusion creep, but has been used extensively in previous studies (e.g., Beaumont et al., 2010; Currie et al., 2015; Krystopowicz and Currie, 2013) which show that it is a good approximation for a large scale, including the lithosphere and the upper mantle. Also, it is a convenient simplification because it saves the computational cost of coupling diffusion and dislocation creep dynamically, and facilitates the stability of the models.

The stress-strain rate relationship for dislocation creep (2.6) is parameterized through a power law derived from experimental studies with different rock types or mineral assemblages (e.g., Gleason and Tullis, 1995; Karato and Wu, 1993) and has the following general form for plain strain conditions:

$$\sigma_s = A_{ps}^{\frac{-1}{n}} \dot{\varepsilon}_s^{\frac{1}{n}} e^{\frac{(E+PV)}{nRT}} \tag{2.6}$$

where σ_s is the maximum shear stress, A_{ps} is a pre-exponential factor scaled to plane strain,

$\dot{\varepsilon}_s$ is the maximum shear strain rate, n is the stress exponent, E is the activation energy, V is the activation volume and R is the ideal gas constant. This constitutive relation is commonly applied to numerical models by computing an effective viscosity (2.7) using the following relationship:

$$\eta_{eff} = \frac{\sqrt{\boldsymbol{\sigma}'_{II}}}{2\sqrt{\dot{\boldsymbol{\varepsilon}}'_{II}}} = \frac{\sigma_s}{2\dot{\varepsilon}_s} \tag{2.7}$$

where, η_{eff} is the effective viscosity, and $\boldsymbol{\sigma}'_{II}$ and $\dot{\boldsymbol{\varepsilon}}'_{II}$ are the second invariants of the deviatoric stress and strain rate tensors, respectively. The combination of (2.6) and (2.7) results in equation (2.8):

$$\eta_{eff} = \frac{1}{2} A_{ps}{}^{\frac{-1}{n}} \dot{\boldsymbol{\varepsilon}}'^{\frac{1-n}{2n}}_{II} e^{\frac{E+PV}{nRT}} \tag{2.8}$$

which is used in the governing equations (2.1-2.3) to model temperature dependent viscous rheologies assuming deformation driven by dislocation creep.

2.3.2 Viscoplastic Rheology

Even though viscous rheologies are suitable to describe deformation by solid state creep in most of the lithosphere and upper mantle, significant portions of the lithosphere exhibit frictional-plastic yielding especially at shallower levels. Plastic behaviour is a non-reversible type of deformation characteristic of solids, which occurs when applied stresses exceed a yield stress. Plasticity is commonly observed in rocks and produces localized deformation along shear zones at shallow depths, under the brittle regime (e.g., Gerya, 2019).

In this work, plastic behaviour is included in numerical models by using the Drucker Prager yield criterion (2.9), which in 2D is described by the following equation:

$$\sigma_y = P sin\,(\phi) + C cos\,(\phi) \tag{2.9}$$

where σ_y is the yield stress, P is the hydrostatic pressure, ϕ is the angle of internal friction, and C is the cohesion. The internal friction angle and cohesion vary depending on the rock type. These parameters describe the frictional-plastic behaviour of rocks and are usually experimentally determined.

The ASPECT code uses the viscosity re-scaling method detailed in Kachanov (2004), in which the effective viscosity (resulting from viscous rheologies) is scaled back to a limiting value (2.10):

$$\eta_y = \frac{\sigma_y}{2\dot{\varepsilon}} \tag{2.10}$$

where η_y is the yielding viscosity and $\dot{\varepsilon}$ is the strain rate, when viscous stresses exceed the yield stress defined in (2.9). In the numerical models this is reflected as a localized weakening in fault-alike zones where viscous stresses reach the yield stress.

2.3.3 Viscoelastic Rheology

Another type of deformation that is characteristic of solids is elastic behaviour. This is a reversible type of deformation that is present in the lithosphere of the Earth. The stress-strain relationship for a viscoelastic rheology is based on the assumption that the total strain rate (2.11) is the result of a viscous strain rate and an elastic strain rate as in the following equation:

$$\dot{\varepsilon}' = \dot{\varepsilon'}^{visc} + \dot{\varepsilon'}^{el} = \frac{1}{2\eta}\sigma' + \frac{1}{2\mu}\frac{D\sigma'}{Dt} \tag{2.11}$$

where $\dot{\varepsilon'}^{visc}$ is the viscous part of the deviatoric strain rate, $\dot{\varepsilon'}^{el}$ is the elastic part of the deviatoric strain rate, η is the viscosity, μ is the elastic shear modulus, and $\frac{D\sigma'}{Dt}$ is the co-rotational time derivative of the deviatoric stress (Kaus & Becker, 2007) or the Jaumann co-rotational stress rate which contains the time derivative of the deviatoric stress and terms that account for rotation (Bangerth et al., 2020b).

When elasticity is included in the numerical models in ASPECT, an elastic effective viscosity η_{eff} is formulated as in (2.12):

$$\eta_{eff} = \eta \frac{\Delta t^e}{\Delta t^e + \tau_M} \tag{2.12}$$

where η is the actual viscosity, Δt^e is the modelling elastic time step, and τ_M is the relaxation time, which is the quotient between the actual viscosity and the shear modulus μ:

$$\tau_M = \frac{\eta}{\mu} \tag{2.13}$$

Additionally, the right-hand side of the momentum conservation equation (2.2) is modified by including (2.14)

$$F^e = -\frac{\eta_{eff}}{\mu \Delta t^e}\sigma' \tag{2.14}$$

where F^e is the elastic force term that opposes to the applied stresses and accounts for reversible deformation, and σ' is the deviatoric stress.

2.4 Gravity Modelling

In this work, the Bouguer gravity anomaly is calculated from the 2D density structure of the numerical models as an additional observable to examine the surface expressions of lithosphere removal. For this, an element mesh approach is used where the contribution of each element in the modelling domain is approximated as the anomaly of a finite slab, as described in Telford et al. (1990). Then, the total anomaly at each observation point along the profile at the ground surface (x_k) is calculated as the sum of the contribution of all the elements in the 2D domain (2.15):

$$\Delta g_k = 2G dz \Delta\rho \sum_{i=1}^{m} \sum_{j=1}^{n} \left[tan^{-1}\left(\frac{dx - |x_k - x_i|}{z_j}\right) + tan^{-1}\left(\frac{|x_k - x_i|}{z_j}\right)\right] \tag{2.15}$$

where, k is an index for the observation points at the ground surface, i and j are horizontal and vertical indices for the elements in the modelling domain, dx and dz are the horizontal and vertical dimensions of a given element respectively, G is the universal gravity constant, $\Delta\rho$ is the density difference with respect to the reference, $|x_k - x_i|$ is the horizontal distance between a given element at j and the observation point k along the profile, z_j is the element depth, m and n correspond to the number of elements horizontally and vertically respectively, and Δg_k represents the gravity anomaly at a given observation point.

The Bouguer plate correction is considered by altering the shallow density structure as follows: On one hand, if the 2D structure has positive topographies (i.e., mountains) the surface is clipped to the ground level (i.e., 0 km elevation). On the other hand, if the 2D structure has negative topographies (i.e., topographic depressions, basins) the density in the elements between the topography and the ground level is calculated as the average density in the surrounding elements. The reference density structure is taken as the average column of the non-disturbed lithosphere and upper mantle in each model at each time step.

Before applying to the geodynamic models, the method is tested by comparing the modelled gravity anomalies with the theoretical formulations in the cases of a cylinder aligned along strike (2.16), and a finite horizontal slab (2.17) (e.g., Telford et al., 1990), with the following equations:

$$\Delta g = 2\pi G r^2 \Delta\rho \frac{z}{x^2 + z^2} \tag{2.16}$$

$$\Delta g = 2Gt\Delta\rho \left[tan^{-1}\left(\frac{L-x}{h}\right) + tan^{-1}\left(\frac{x}{h}\right)\right] \tag{2.17}$$

where, L represents the horizontal length of the slab, t is its thickness, and h is its depth. Also, r represents the radius of the cylinder, and z represents its depth. Additionally, the gravity anomaly is calculated using the approach developed by Talwani et al. (1959), to compare the accuracy of the method proposed with another algorithm.

2.4.1 Cylinder Test

The synthetic data for the cylinder test consists of a uniform 400×200 element mesh in a domain with horizontal and vertical dimensions of 400 km and 200 km, respectively (element resolution of 1 km). The background material has a density of 2800 kg/m^3 and there is a cylinder with radius and density of 20 km and 3100 kg/m^3 respectively, with its centre at a distance of 200 km along the profile. Figure 2.1 shows the modelled and theoretical gravity anomalies for a buried cylinder at depths of 50, 40, 30, and 20 km.

This numerical method gives gravity values that are consistent with the theoretical values.

There is a maximum misfit of 2.73% (right on top of the cylinder) when the centre of the cylinder is located at a depth of 20 km, calculated using equation (2.18):

$$\%Error = \frac{|\Delta g_{numerical} - \Delta g_{theoretical}|}{|\Delta g_{theoretical}|} \times 100\% \quad (2.18)$$

where $\Delta g_{numerical}$ and $\Delta g_{theoretical}$ are the numerical and theoretical gravity anomalies right above the cylinder, respectively.

For comparison, the calculations using the algorithm proposed by Talwani et al. (1959) produce a misfit of 5.54% relative to the theoretical values for the same case (Figure 2.1d).

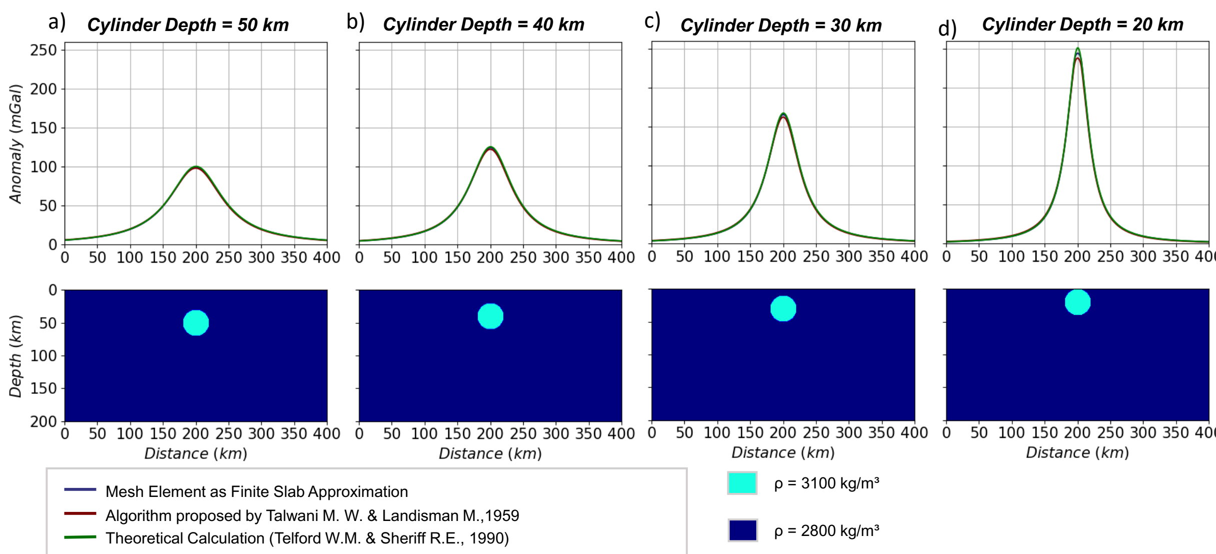

Figure 2.1: Modelled and theoretical 2D gravity anomalies for a buried cylinder with a radius of 20 km and a density 3100 kg/m^3, embedded in a terrain with a density of 2800 kg/m^3, at depths of a) 50, b) 40, c) 30, and d) 20 km. The gravity anomaly is modelled using both the approach proposed in this study (mesh element as finite slab approximation) and the approach from Talwani et al. (1959).

2.4.2 Finite Slab Test

The finite slab test uses a 2D domain with the same dimensions and elements than the cylinder test. Figures 2.2 and 2.3 show the modelled and theoretical gravity anomalies for horizontal slabs of lengths of 20, 30, 40, 50, and 100 km.

The background material also has a density of 2800 kg/m^3 but in this case, a horizontal slab with a thickness of 20 km and a density of 3100 kg/m^3 is embedded at a distance of

200 km along the profile. The length L of the slab is varied to explore the effect of density perturbations at the sides of the domain.

These results show consistency between the gravity values, with a maximum misfit of 4.45% for the slab with length of 100 km (using equation 2.18 for the gravity anomaly above the centre of the slab). For comparison, the calculations using the algorithm proposed by Talwani et al. (1959) produce a misfit of 5.98% for the same slab length (Figure 2.3b). The error increases closer to the lateral boundaries because these are artificial features of the numerical models which do not represent physical phenomena. Consequently, boundary effects are a limitation of this approach. However, the density anomalies in the models presented in this thesis are localized in the middle of the domain where boundary effects are negligible.

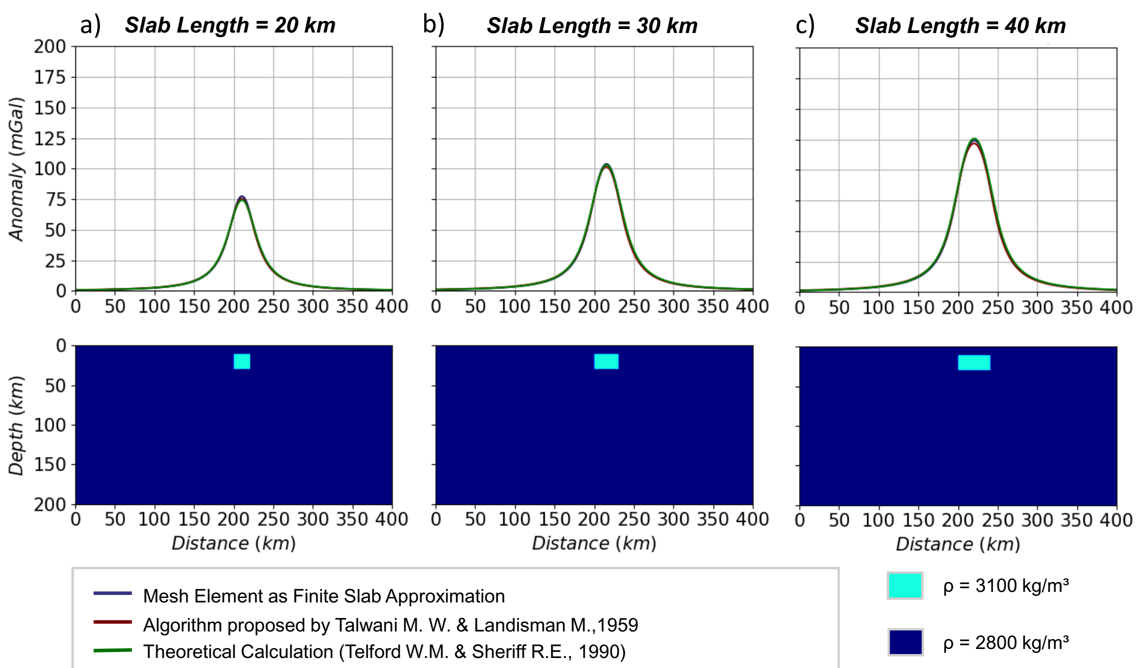

Figure 2.2: Modelled and theoretical 2D gravity anomalies for a buried finite slab with a thickness of 20 km, a density of 3100 kg/m^3, and lengths of a) 20, b) 30, and b) 40 km, embedded in a terrain with a density of 2800 kg/m^3. The gravity anomaly is modelled using both the approach proposed in this study (mesh element as finite slab approximation) and the approach from Talwani et al. (1959).

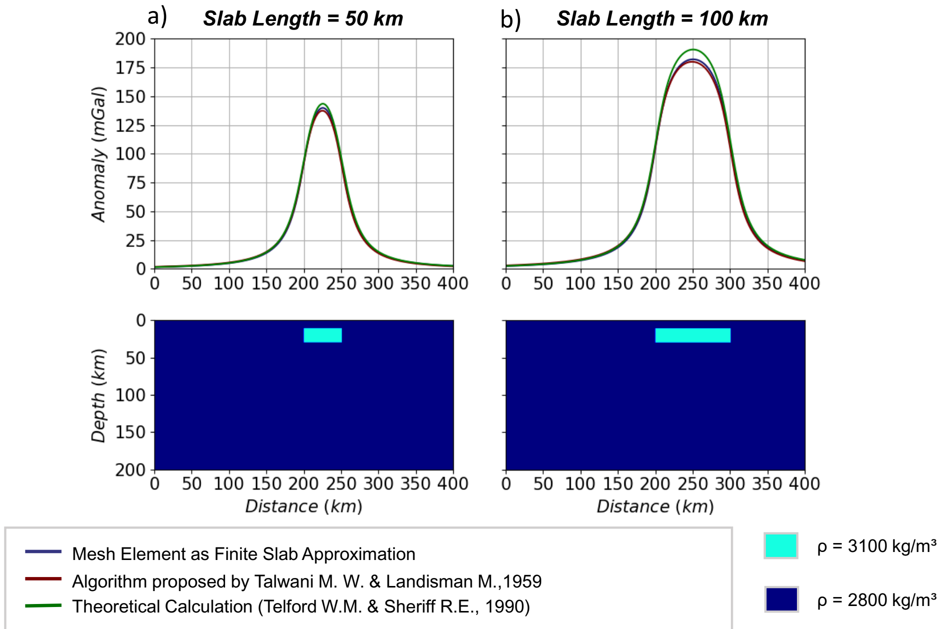

Figure 2.3: Modelled and theoretical 2D gravity anomalies for a buried finite slab with a thickness of 20 km, a density of 3100 kg/m^3, and lengths of a) 50, and b) 100 km, embedded in a terrain with a density of 2800 kg/m^3. The gravity anomaly is modelled using both the approach proposed in this study (mesh element as finite slab approximation) and the approach from Talwani et al. (1959).

2.4.3 Convergence Test

The method proposed in this Chapter is tested for convergence using the density structure of a cylinder embedded at a depth of 50 km (same density structure in Figure 2.1a). The convergence test is also computed for the algorithm by Talwani et al., 1959 as a reference. In this test the calculations use different element resolutions starting from 5 up to 1 km per element. Since the elements in the mesh are square, the vertical and horizontal resolution is always the same.

Figure 2.4a shows the value of the modelled gravity anomaly in the middle of the domain (above the cylinder) with different resolutions showing convergence as the mesh becomes finer. Figure 2.4b shows the percent error of the numerical results in 2.4a with respect to the theoretical value using equation (2.18). These results show that if the mesh has element lengths below 4 km there is less than 1% error in the numerical gravity anomaly calculations using the method proposed.

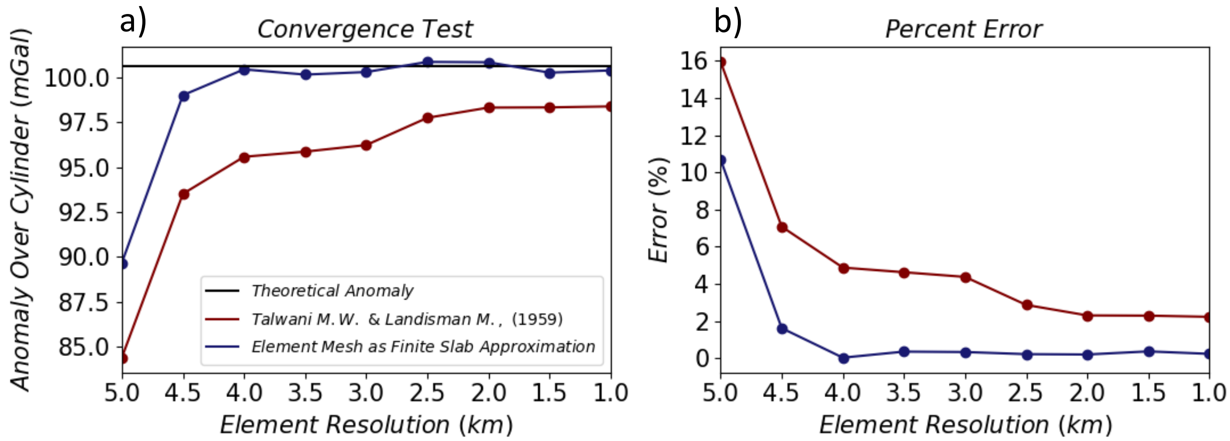

Figure 2.4: Resolution convergence test for the gravity anomaly method proposed (mesh element as finite slab approximation) compared to the method by Talwani et al. (1959). This test uses calculations of the anomaly of a cylinder with a radius of 20 km embedded at a depth of 50 km (as in Figure 2.1a) with different element resolutions. In all the cases the elements in the mesh are square (same spatial resolution vertically and horizontally). a) Gravity anomaly in the middle of the domain right over of the cylinder (also the maximum gravity anomaly in all the cases) with different element resolutions showing convergence as the mesh becomes finer. b) Percent error of the numerical calculations with respect to the theoretical value of the gravity anomaly in the middle of the domain.

2.4.4 Summary

The gravity anomaly calculations could produce misfits up to 2.8% or 4.5% when the studied density anomaly is either very shallow or very close to the side boundary of the model domain, respectively. This behaviour is also observed in the results using the approach from Talwani et al. (1959), which produces a slightly higher error with respect to the theoretical gravity anomalies (1% higher on average). The mesh element as finite slab approach produces errors under 5% caused by boundary effects, but when the density anomaly is at a distance from the boundaries, and the element lengths are lower than 4 km, the error is under 1% (the numerical result converges to the theoretical solution). This shows that gravity calculations are accurate enough for the purpose of this study because the objective is to provide first order approximations that characterize the general behaviour, rather than producing a precise fit of the Bouguer gravity anomaly. Aside, the density alterations in the models presented in this thesis are commonly located in the centre of the modelling domain (at a distance from the lateral boundaries), and at depths corresponding to the upper mantle (> 40 km). The approach presented provides a method to determine the first order gravity anomaly produced by the 2D density structures of geodynamic models.

Chapter 3: Preliminary Models

3.1 Introduction

The lithosphere removal ("dripping") of a convective instability consists of the downward growth of a gravitational perturbation in the lower lithosphere, leading to its complete descent. This is commonly produced by its higher density compared to the sub-lithosphere mantle due to its lower temperature. This type of lithosphere removal has been extensively investigated in previous modelling studies using different software and numerical formulations (e.g., Göğüş and Pysklywec, 2008; Houseman et al., 1981; Houseman and Gemmer, 2007; Kaus and Becker, 2007; Wang et al., 2014). A common interest in most of the previous studies has been to understand and constrain the surface expressions produced by this type of dynamic mechanism.

Similarly, one of the objectives of this work is to investigate the dynamics of lithosphere dripping and the effects on Bouguer gravity anomaly and surface topography. Hence, the set of models presented in this chapter aims to test how these surface observables change in models with different numerical implementations. Specifically, the main interest is to test the gravity anomaly calculations using the method described in section 2.4, based on geodynamic models for codes with different advection mechanisms. This is because the gravity calculations depend on the density structure, and the latter depends on the formulation used to displace material properties in space in the numerical (geodynamic) models.

This chapter includes a set of three 2D models (set N), of the lithosphere and upper mantle, designed to induce a standard and simplified mantle lithosphere drip. These models are computed using the finite element codes ASPECTv2.2.0 (Bangerth et al., 2020a) and SOPALE (Fullsack, 1995). On one hand, the SOPALE code uses a marker-in-cell method to displace material properties. On the other hand, the ASPECT code can use two methods. In the first approach, the advection equation is solved over compositional fields that trace the materials (equation 2.5). Alternatively, ASPECT can also use a marker-based method known as advection with active particles. These possibilities are used to identify their general effect on the results, and specifically, their influence on the modelled Bouguer gravity anomaly and surface topography.

3.2 Modelling Setup

The setup used for the models presented is shown in Figure 3.1. The models have a three layered structure including a crust (40 km thick), mantle lithosphere (40 km thick) and sublithospheric mantle, in a 2D domain with both width and length of 375 km. Additionally, the drip is triggered by a rectangular mantle lithosphere perturbation with a width of 125 km and amplitude of 40 km.

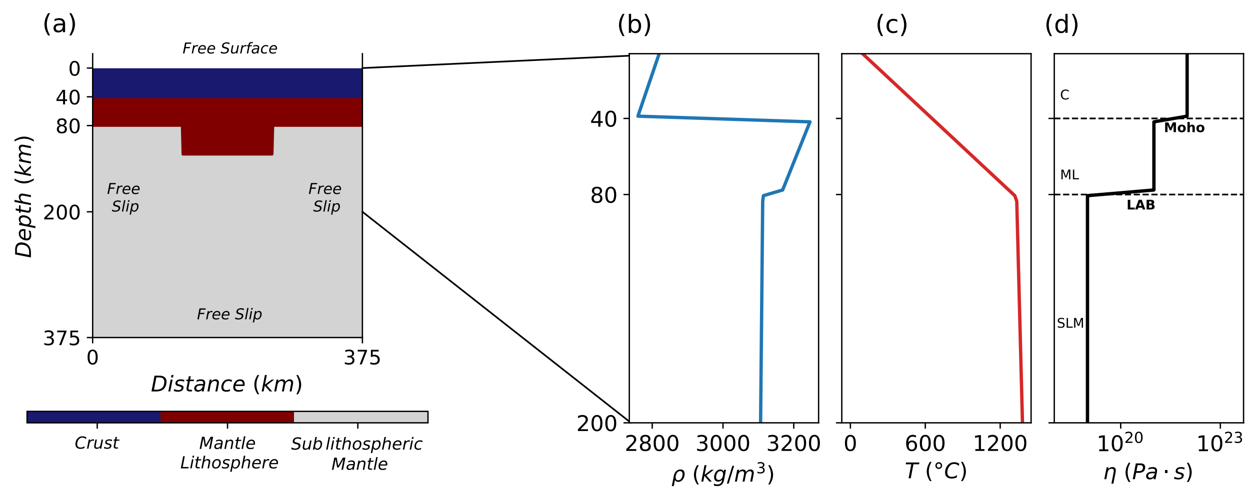

Figure 3.1: (a) Initial model geometry for the preliminary models. (b) Temperature dependent density structure and (c) initial geotherm for the region outside of the lithosphere perturbations. The continental geotherm is stretched in the thickened region, keeping the Moho temperature constant. (d) Reference viscosity structure showing three isoviscous layers corresponding to the crust, mantle lithosphere and sub-lithospheric mantle.

The boundary conditions for the sides and the bottom of all the models are of free slip. The top boundary of models N1 and N2 is a free surface which allows for topographic variations produced by the mantle-lithosphere dynamics and the top boundary for model

N3 has free slip conditions. Each of the layers has a constant viscosity and temperature dependent density:

$$\rho = \rho_0(1 - \alpha\Delta T) \tag{3.1}$$

where ρ_0 is the reference density, α is the thermal expansion coefficient, and ΔT is the temperature difference with respect to the surface temperature $T_0 = 273$ K. Table 3.1 gives the reference density and viscosity used for each material. All materials use the same thermal parameters, with the values given in table 3.2.

Table 3.1: Material parameters for each layer in the models presented in this chapter.

Layer	**Reference Density** (kgm^{-3})	**Viscosity** $(Pa \cdot s)$
Crust	2800	1×10^{22}
Mantle lithosphere	3300	1×10^{21}
Sub-lithospheric Mantle	3250	1×10^{19}

The initial temperature conditions are set using a standard continental conductive geotherm (e.g., Schubert et al., 2001) with thermal conductivity of 2.25 $\frac{W}{mK}$, surface heat flow of 37.46 $\frac{mW}{m^2}$, and no heat production, with a mantle adiabat with temperature potential of 1573 K and adiabatic gradient of 0.4 $\frac{K}{km}$ (Figure 3.1c). The lithosphere thickness and therefore the depth of the lithosphere-asthenosphere boundary corresponds to the depth at which the mantle adiabat crosses the conductive geotherm. In the models of this chapter the latter intersection occurs at a depth of 80 km and at a temperature of 1605 K. The thermal boundary conditions use the initial temperature in all boundaries as fixed values in which the maximum temperature is 1837 K (for the bottom boundary at 660 km), and the minimum temperature is 273 K (for the surface).

The SOPALE model (model N1) has a 120×120 Eulerian mesh, where each element has a resolution of 3.10 km$\times$ 3.10 km, together with a uniformly spaced Lagrangian grid with 721×361 nodes. In this code, the material properties are carried in the Lagrangian nodes, which are advected with the velocity field. The dominating material (majority) among the Lagrangian nodes (markers) within each cell, is assigned to each of the Eulerian elements together with its properties. These properties are then used in solving the governing equations (2.1 - 2.3) for the Eulerian mesh. On the other hand, the ASPECT model (model N2) uses a 128 × 128 element mesh where the resolution per element is 2.93 km × 2.93 km. The element resolution in the SOPALE and ASPECT models is chosen to be as similar as possible, keeping square elements. However, resolutions can not be exactly equal due to limitations in the codes. The ASPECT model that uses the active particles method (model N3) uses a total of 450000 particles which are randomly distributed in the modelling domain. These particles carry the material properties and these are assigned to the elements of the global mesh using the cell average criterion.

Table 3.2: Common thermal parameters used in all the models presented in this chapter.

Parameter	**Value**	**Units**
Specific heat (C_p)	1250	$J\ kg^{-1}\ K^{-1}$
Thermal conductivity (k)	2.25	$W\ m^{-1}\ K^{-1}$
Heat production (H)	0	$W\ kg^{-1}$
Surface heat flow (q_0)	37.46	m$W\ m^{-2}$
Thermal expansion coefficient (α)	3.5×10^{-5}	K^{-1}
Adiabatic gradient	$0.4{\times}10^{-3}$	$K\ m^{-1}$
Adiabatic temperature potential (Reference at the surface)	1573	K

3.3 Advection Mechanisms and Drip Observables

In this section, the results of the models of set N are discussed. These models use the same setup (Figure 3.1) with comparable mesh resolutions, and differ only in the software used and corresponding advection mechanism. Model N1 is computed in SOPALE using the marker-in-cell method, model N2 is computed in ASPECT using the advection equation, and model N3 is computed in ASPECT using the active particles method. Snapshots of the modelling results are shown in Figure 3.2 and the time series of the corresponding surface topography (H) and Bouguer gravity anomaly (Δg_B) are shown in Figure 3.3. During the drips the mantle lithosphere at the sides is entrained and pulled to the central region where it sinks, producing crustal contraction in the central region and extension at the sides. Figure 3.2 shows that the drips in models N2 and N3 (computed in ASPECT) descend slightly faster than the drip in model N1 (SOPALE). However, the difference in drip velocity does not produce significant changes in the timescales of the evolution of surface observables, as shown in the trends in Figure 3.3.

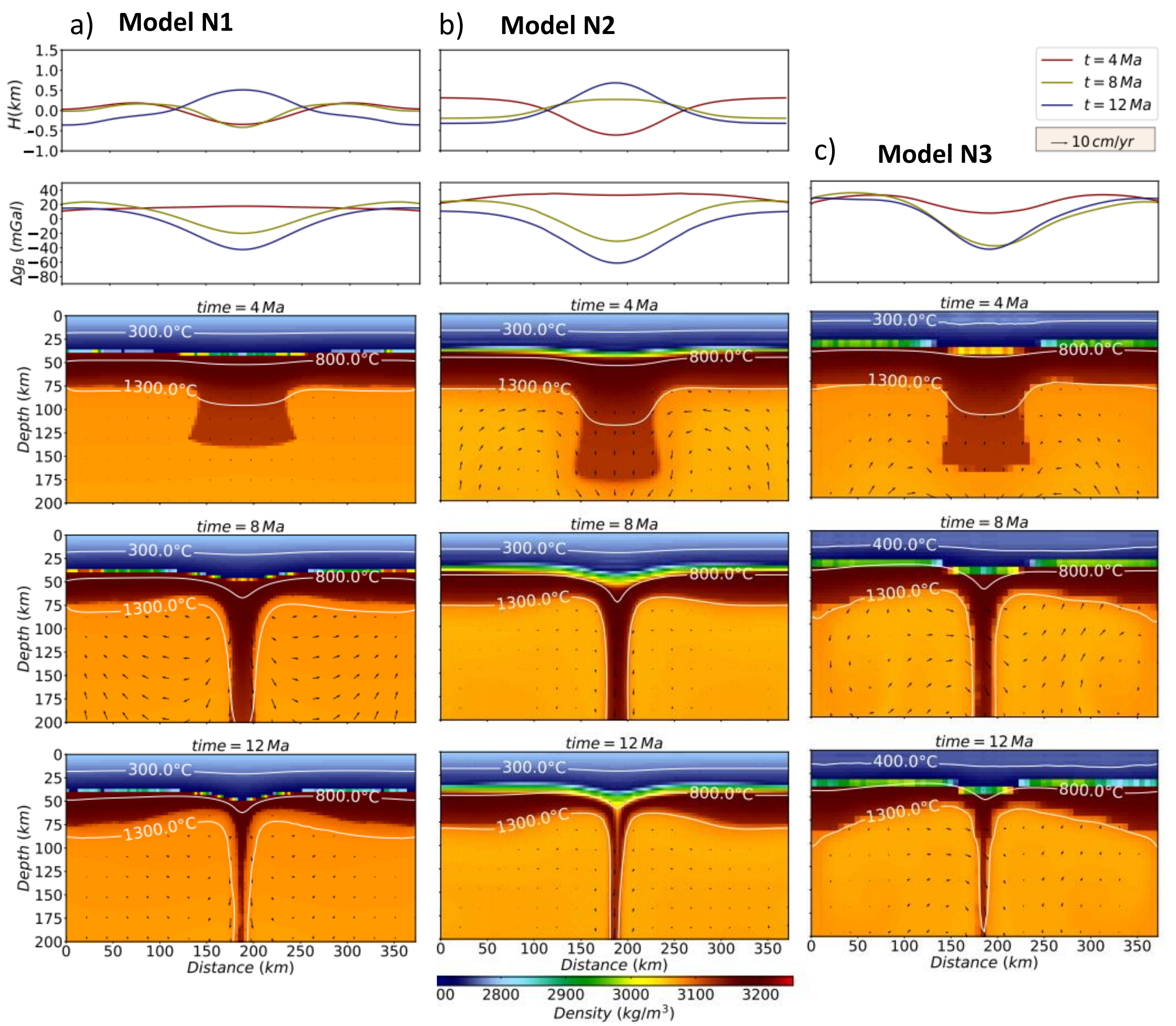

Figure 3.2: Model results for preliminary drips using (a) the marker-in-cell advection strategy in the SOPALE code (model N1), (b) the solution of the advection equation over compositional fields in the ASPECT code (model N2), and (c) the active particles advection method in the ASPECT code (model N3). The plots for each model include profiles of topography H (top plot), Bouguer gravity anomaly Δg_B (second plot), and cross-sections of density structure (lower three plots), at 4, 8 and 12 Ma, showing the evolution of the drip. Results in (c) do not include topography because the use of a free surface with active particles is not supported in ASPECTv2.2.0.

In all the models, the higher density of the mantle lithosphere perturbation triggers its dripping, producing subsidence of the overlying surface owing to the pull of the drip (up to 250 m in model N1 and 700 m in model N2). After the arrival of the dripping material to the bottom boundary there is surface uplift caused by the relaxation of downward stresses and the upwelling of lower-density (and buoyant) sub-lithospheric mantle that replaces the removed portions of mantle lithosphere. The latter produces regions with maximum elevations of 500 m and 700 m in models N1 and N2, respectively. Throughout the phase with positive elevations (e.g., Figure 3.3*a* after 8 Ma), topographic results in SOPALE are consistently 200 m lower than the results produced in ASPECT. However, by 30 Ma the topographies equilibrate at same heights (close to 0 m of elevation).

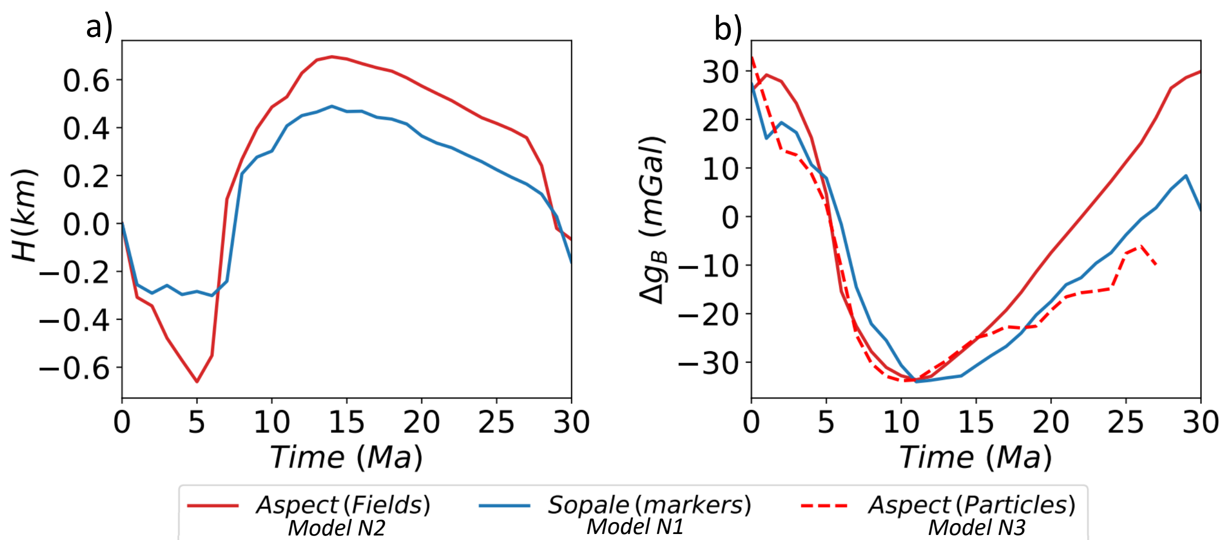

Figure 3.3: Time variation of surface observables in the middle of the profile averaged over a 100 km width above the perturbation for models N1, N2 and N3 including (a) surface topography (H), and (b) Bouguer gravity anomaly (Δg_B). Topography is not reported for model N3 because the use of a free surface with active particles is not supported in ASPECTv2.2.0.

For the Bouguer gravity anomaly, the initial mantle lithosphere instability produces a positive initial anomaly (about +30 mGal) which decreases rapidly due to the crustal contraction and thickening (average of 10 km at 8 Ma for all the models) produced by the drip (nearly reaching -35 mGal in all models). Then, as the sub-lithospheric mantle rises, crustal thinning is induced and produces an increase in the gravity anomaly. Figure 3.3*b* shows that at later times the gravity anomaly magnitude in model N2 has a higher increase compared with models N1 and N3. This behaviour is attributed to numerical diffusion generated through the use of the numerical solution of the advection equation in model N2. This results in a diffusion of the interface between the crust and the mantle lithosphere (Moho) which progressively increases the Bouguer gravity anomaly, leading to a maximum difference of 20 mGal.

These models exhibit significant numerical diffusion because crustal viscosity is very low and it allows for substantial crustal flow in few million years, producing relatively fast deflections of the Moho. This phenomenon is considered to be negligible in models using Earth-like rheologies with temperature-dependent power laws or full viscoplastic rheologies in the timescales of interest because realistic viscosities are significantly higher and limit crustal flow. For instance, supplementary models in appendix A (models N4 and N5) show that when crustal viscosity is increased in 3 orders of magnitude ($\eta_{crust} = 10^{25}$ Pa $\cdot$ s) the crust-mantle interface remains non-diffused by numerical artifacts (interface remains sharp) even at advanced stages of the drip. In the latter case, results of the Bouguer gravity anomaly are consistent (even at late times) using either compositional fields or active particles to displace physical properties in space.

The purposes of this work require the use of the advection strategy of model N2 (advection with compositional fields) because modelling the evolution of surface topography is essential, and the use of a free surface together with the active particles method is not supported in ASPECTv2.2.0 (Figure 3.2*c*). Nevertheless, the models of set N are useful to examine the effect of numerical diffusion during advection and the results allow to evaluate its implications for the models in this thesis. For instance, the results of model N2 indicate that the gravity anomaly calculations could be affected by numerical diffusion and should be analyzed with caution (especially at late modelling times) if the crustal viscosity is low (e.g., a constant viscosity of 10^{22} Pa·s). However, the rest of the models presented in this work use high (Earth-like) rheologies in the crust for which numerical diffusion is not significant (if any), similarly as in model N4 (appendix A), and it does not affect the gravity anomaly calculations. Hence, the following models use the fully supported advection strategy of model N2 and N4 in ASPECT (Bangerth et al., 2020b).

3.4 Summary and Conclusions

This chapter explored the effect of the advection mechanism of the modelling software on the overall results and the observables of gravity anomaly and surface topography in three equivalent drip models. Models N1 and N3 use a marker-based advection method in the SOPALE and ASPECT codes, respectively. In this approach the physical properties are carried by markers or particles which are advected in space according to the velocity field. In model N2 the physical properties are displaced by solving the advection equation over the compositional fields of the simulation using the ASPECT code. The main conclusions obtained from the results are listed below.

- The overall trends and behaviours in the models of set N are qualitatively consistent. All models produce similar patterns and magnitudes in both surface topography and Bouguer gravity anomaly.

- In the ASPECT models the mantle lithosphere instability drips faster. For example, in model N2 (ASPECT) the drip is ∼40 km deeper in the first 4 Ma in compared with model N1 (SOPALE). However, this difference does not produce significant alterations in the evolution of surface expressions.

- Topographic deflections produced in ASPECT are more pronounced than the deflections in SOPALE by a few hundred meters (∼300 m) for both subsidence and uplift.

- If the crustal viscosity is low ($\leq 10^{22}$ Pa·s) and there are high-amplitude deflections in the crust-mantle interface (Moho) in the timescales studied, the gravity anomaly calculations could be affected by numerical diffusion at the boundary (deviations up to 20 mGal in the present models). However, the use of high (Earth-like) viscous rheologies reduces the deflections of the Moho and in this case, the effects of numerical diffusion are not significant. Consequently, the rest of the models in this thesis use high (Earth-like) rheologies.

Chapter 4: Parametrization of the Region of Study in 2D

4.1 Introduction

One of the major challenges in understanding lithosphere removal is that the general dynamics and associated surface observables are strongly dependent on the initial conditions and modelling setup. In addition, material properties (e.g., rheologies and densities) have significant effects on removal dynamics. For instance, some studies have used isoviscous material layers (e.g., Houseman et al., 1981; Kaus and Becker, 2007) while others have used experimental results from rheological studies (e.g., Gleason and Tullis, 1995; Karato and Wu, 1993; Zhang and Green, 2007) to constrain and implement more realistic lithosphere structures (e.g., Beaumont et al., 2010; Currie et al., 2015; Göğüş and Pysklywec, 2008) often producing fundamentally different behaviours and surface effects. Consequently, crustal/lithosphere thickness, its associated thermal structure, and the influence of the latter in temperature-dependent material properties (such as density or viscosity), are important parameters that must be treated rigorously to produce realistic models.

Due to the broad variation of possible expressions of lithosphere removal, this phenomenon has been proposed to explain a wide variation of scenarios. For instance, it has been associated with high mountain regions, such as the Sierra Nevada California (e.g., Saleeby et al., 2012) or the Puna plateau (e.g., Beck and Zandt, 2002; Kay and Mahlburg Kay, 1993), as well as topographic depressions such as the Arizaro basin (e.g., DeCelles et al., 2015) or the cratonic Congo basin (e.g., Downey and Gurnis, 2009). In this thesis, as described in section 1, the purpose is to test if lithosphere removal can explain the observations in the region of the Sierra Nevada de Santa Marta (SNSM), in northern Colombia (including topographic expressions and Bouguer gravity anomaly). Therefore, this chapter includes multiple sets of 2D numerical models intended to constrain the modelling parameters to model realistic lithosphere drips.

The proposed mechanism aims to explain the high Bouguer gravity anomaly through a mantle lithosphere drip followed by eclogitization and removal of the crustal root under the SNSM massif. The initial conditions assume that previous crustal shortening produced a mantle lithosphere instability that triggers its dripping. The models test if drip dynamics can induce the required conditions for eclogitization of the lower crust and can induce its removal. If that is the case, lithosphere removal dynamics must be capable of either producing surface uplift or maintaining the initial topographies after the removal of the crustal root. To verify this, the initial conditions, the starting configuration and the material model is built based on the SNSM. The subsequent models include parameter modifications to explore, understand and constrain their effects. The models include tests of the amplitude of the mantle lithosphere instability and/or total amount of initial lithosphere thickness in the region, velocity boundary conditions, width of the perturbation, and parameters related to plastic deformation.

4.2 Modelling Setup

4.2.1 General Configuration

The models in this chapter use a 2D domain with a width of 1320 km and a length of 660 km representing the continental lithosphere and the upper mantle in the region of the SNSM (figure 4.1). This encompasses the Earth's structure from the surface to the 660 km discontinuity phase transition. This setup does not include the Caribbean plate because the focus of this research is lithospheric drip dynamics and its isolated contribution to surface observables. The mesh has square elements with lengths and widths of 2.58 km in the upper 200 km and 10 km below. The upper region has a finer mesh to properly resolve lithospheric deformation. The lateral boundary conditions are free slip, the bottom boundary condition is no slip, assuming that the high-viscosity lower mantle is coupled to the upper mantle, and the top boundary has a free surface that allows surface deformation (See details in Rose et al., 2017). The thermal boundary conditions use the initial temperature (figure 4.1c) in all boundaries as fixed values in which the maximum temperature is 1837 K (at a depth of 660 km), and the minimum temperature is 273 K (at 0 km).

The crustal thickness is 40 km, consisting of a 20 km upper crust and 20 km lower crust, underlain by an 80 km mantle lithosphere. Because the collision of the Caribbean large igneous province with South America started 75 Ma ago according to Spikings et al. (2015) and subsequent regional tectonics has been characterized by compression, it is assumed that this region underwent crustal shortening. Consequently, there is a thickened crustal region in the middle of the profile of the initial setup (figure 4.1a) representing the SNSM.

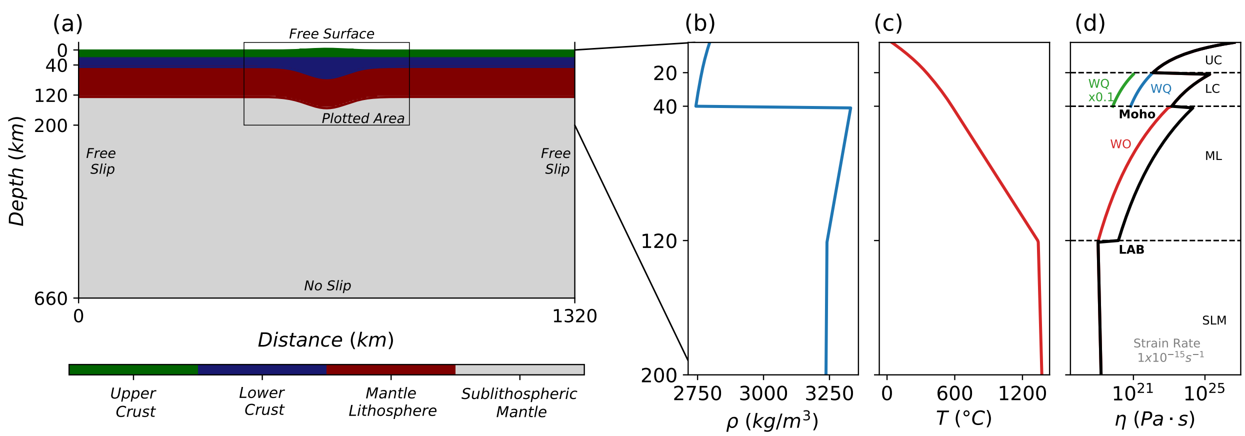

Figure 4.1: (a) Initial model geometry used in parameter tests. Only the enclosed region is shown in the following model figures. (b) Non-perturbed density structure. (c) Initial temperature conditions. The continental geotherm is stretched in the thickened region keeping the Moho temperature constant. (d) Reference temperature-dependent viscosity structure at a constant strain rate of $10^{-15}s^{-1}$ (black). Coloured lines show other viscous rheologies used. WQ: Wet Quartzite (Gleason & Tullis, 1995), WO: Wet Olivine (Karato & Wu, 1993).

The thickened region consists of initially high surface topography and a crustal root. These deflections have Gaussian shapes with a half-width of 125 km. In the middle of the profile, this region is about 35 km thicker than the undisturbed crust, including both the crustal root and the topography. The amplitude of the initial topography with respect to the crustal root is set to be in isostatic balance under the assumption that equilibrium occurred right after or during the previous shortening episode. Also, it is assumed that during previous crustal thickening the underlying mantle lithosphere was simultaneously immersed into the sublithospheric mantle being displaced by the new crustal root. This displacement is considered in the reference initial conditions (figure 4.1a), and produces a deflection in the lithosphere-asthenosphere boundary (LAB) which is gravitationally unstable.

The models presented have temperature-dependent densities and viscosities. The density ρ is computed following equation 3.1, with a reference temperature T_0 of $273K$. Viscous deformation follows the power law for dislocation creep (2.8) introduced in section 2.3.1.

The initial temperature conditions for all the models are set for a continental geotherm with a surface heat flow of 49.37 $\frac{mW}{m^2}$, a thermal conductivity of 2.25 W/mK, and a radiogenic heat production in the upper and lower crust of 1×10^{-6} W/m^3 and 0.4×10^{-6} W/m^3, respectively. At the LAB, the conductive geotherm intersects the mantle adiabat which has a constant geothermal gradient of 0.4×10^{-3} K/m, and a potential temperature of 1565 K, at a depth and temperature of 120 km and 1613 K, respectively. The resultant geotherm is displayed in figure 4.1c. In the central region the continental geotherm is linearly stretched following the Gaussian-shaped thickening, to keep the initial Moho temperature constant throughout the profile.

The material properties and parameters are listed in table 4.1. In the reference model (model T3), the upper crust, lower crust, mantle lithosphere and sublithospheric mantle have viscous rheologies of wet quartzite (WQ) (Gleason & Tullis, 1995), dry Maryland diabase (DMD) (Mackwell et al., 1998), dry olivine (DO) and wet olivine (WO) (Karato & Wu, 1993), respectively. In all the models, viscosity is limited between maximum and minimum numerical cut-off values of 1×10^{28} Pa $\cdot$ s and 1×10^{19} Pa $\cdot$ s to maintain the stability of computations because, as noted by Bangerth et al. (2020b), when the simulations have large viscosity ranges they can result in divergence of the solver and numerical instabilities.

4.2.2 Lower Crustal Eclogitization

Eclogitization is a phase transition experienced by lower crustal rocks when they are subjected to high pressures, and results in rocks with eclogite metamorphic facies. It is considered to affect the lower crust of mountainous regions and is known to produce a large density increase that destabilizes the crustal root, leading to its detachment (e.g., Leech, 2001). For instance,

Table 4.1: Material properties for the models in this chapter.

Parameter	Upper Crust	Lower Crust	Mantle Lithosphere	Sublithospheric Mantle
$\rho_0\,(kg\ m^{-3})$	2800	2800	3400	3400
$\alpha\,(K^{-1})$	3×10^5	3×10^5	3×10^5	3×10^5
Viscous rheology	*Wet Quartzite*	*Dry Diabase*	*Dry Olivine*	*Wet Olivine*
$A_{ps}\,(Pa^{-n}\ s^{-1})$ *	8.57×10^{-28}	5.78×10^{-27}	1.43×10^{-16}	1.76×10^{-14}
n	4.0	4.7	4.0	3.0
$E\,(kJ\ mol^{-1})$	223	485	540	430
$V\,(m^3\ mol^{-1})$	0	0	1.5×10^{-5}	1.0×10^{-5}
Thermal Parameters				
$k\,(W\ m^{-1}\ K^{-1})$	2.25	2.25	2.25	2.25
$C_p\,(J\ kg^{-1}\ K^{-1})$	1250	1250	1250	1250
$H\,(W\ kg^{-1})$	3.57×10^{-10}	1.38×10^{-10}	0	0

$*$ Experimental uni axial strain viscosity pre-factor A_{uni} is scaled to plane strain A_{ps} using a scaling factor of $3^{\frac{n+1}{2}}2^{-1}$.

previous studies (e.g., Ahrens and Schubert, 1975; Austrheim et al., 1997; Leech, 2001) agree that metamorphic eclogitization can occur under eclogite-facies conditions (600 - 800°C and 1.0 -2.0 GPa) if there is water available. Moreover, there is also evidence that eclogite facies rocks can form as the dense residue after magmatic differentiation in the crustal root of continental arcs (e.g., Ducea et al., 2021a; Ducea et al., 2021b). Consequently, eclogitization could have taken place in the region of the SNSM because it was formed as a continental magmatic arc, as reported in previous studies (e.g., Cardona et al., 2010; Ramírez et al., 2020).

This means that the presence of dense eclogites in the context of the SNSM could be explained by magmatic differentiation or by a metamorphic phase change produced by previous shortening. Because both hypothesis are plausible, the presence of a densified lower crust before or during a lithosphere removal episode is feasible. However, this study tests if the pressure and temperature conditions for metamorphic eclogitization can be induced independently by lithosphere drip dynamics. Hence, the models presented in this chapter include eclogitization in the lower crust when its temperature is above 600°C and its pressure is above 1.2 GPa. The reference density for eclogite is 3600 kg/m^3 representing full eclogitization of a basaltic lower crust (e.g., Austrheim et al., 1997). Also, eclogite strength is modelled by using the wet quartzite rheology from Gleason and Tullis (1995) as a starting simplified approach. The purpose is to use a weak rheology considering that Austrheim et al. (1997) report that eclogites should be rheologically weak. The effect of eclogite rheology is fully tested using a more rigorous approach in chapter 5.

4.2.3 Reference Model (Model T3) and Parameter Variations

The reference model for this chapter uses the setup described in section 4.2.1 and the rheologies used result in the viscosity structure in figure 4.1*d* (see black curve). This viscosity is used in the non-perturbed regions (the sides where there is no thickening). However, since multiple studies have identified previous stages of substantial continental arc magmatism in the SMSM (e.g., Cardona et al., 2010; Quandt et al., 2018; Ramírez et al., 2020; Tschanz et al., 1974), some rheological modifications in the region of the massif (the thickened region in the middle) are tested to assess their effects.

In particular, it is important to consider the effect of an increased hydration produced by the water content from the subducting slab in the continental arc in the Paleocene-Eocene (e.g., Cardona et al., 2010), or even from the currently subducting and/or underthrusting Caribbean slab. Consequently, the strength of the lower crust and the mantle lithosphere in the middle of the profile in a width of 125 km is reduced. For the lower crust, the rheology of the dry Maryland diabase (Mackwell et al., 1998) is replaced by the viscous rheology of wet quartzite (Gleason & Tullis, 1995), and the resultant effective viscosity is then reduced by one order of magnitude (see green line in figure 4.1*d*. Also, the rheology of the mantle lithosphere is modified from dry to wet olivine (Karato & Wu, 1993) (see red line in figure 4.1*d*). The rest of the models are developed from the reference and thus, they also include a weaker lithospheric rheology in the thickened region. Parameter variations in each model are summarized in table 4.2. Models in chapter 5 show further tests of lithosphere rheology.

4.3 Initial Lithosphere Thickening

The selected modelling setup was chosen to test if a lithosphere removal episode could explain the current state of the SNSM, in terms of its topography and Bouguer gravity anomaly. This assumes that previous crustal shortening produced the required thickening to trigger

Table 4.2: List of models with parameter variations with respect to the reference model.

Model	Modification with respect to the reference	Figure No.
Set T [a]		
T1	Crustal root amplitude is of 10km	4.2*a*
T2	Crustal root amplitude is of 20km	4.2*b*
T3 (Reference)	Crustal root amplitude is of 30km	4.2*c*
T4	Crustal root amplitude is of 40km	4.3*a*
T5	Crustal root amplitude is of 50km	4.3*b*
Set CV		
CV1	As T3 but with lateral compression at $0.1mm/yr$	4.6*a*
CV2	As T3 but with lateral compression at $0.5mm/yr$	4.6*b*
Set SW [b]		
SW1	As CV1 but includes plastic behaviour with strain weakening using plastic strain	4.9*a*
SW2	As CV1 but includes plastic behaviour with strain weakening using total strain	4.9*b*
Set P		
P1 (Reference Plastic)	As SW1 but with lateral compression at $1mm/yr$	4.11*b*, 4.15*b*
P2	As P1 but cohesion is always 20 MPa (no strain weakening in C)	4.11*a*
P3	As P1 but the friction angle ϕ varies from 15° to 5°	4.13*a*
P4	As P1 but the friction angle ϕ is always 15° (no strain weakening in ϕ)	4.13*b*
P5	As P1 but the friction angle ϕ is always 30° (no strain weakening in ϕ)	4.13*c*
Set V		
V1	As P1 but with lateral compression at $0.5mm/yr$	4.15*a*
V2	As P1 but with lateral compression at $5mm/yr$	4.16*a*
V3	As P1 but with lateral compression at $10mm/yr$	4.16*b*
Set W		
W1	As P1 but with no lateral compression	4.19*a*
W2 [c]	As W1 but the half width of the initial perturbation/topography is reduced by half ($62.5km$)	4.19*b*

[a] In all the models the initial crustal root is balanced isostatically with the initial topography. When the amplitude of the crustal root is modified, the initial topography is also modified to maintain isostatic balance in the crust such that changes in the topography are only triggered by the lithosphere dynamics.
[b] When strain increases from 0.5 to 1.5, ϕ changes from 15° to 2° and C changes from 20 to 2 MPa.
[c] In all the models except by model W2 the half width of the mantle lithosphere perturbation, crustal root and initial topography is of 125 km.

the removal. However, the total lithosphere/crustal thickness prior to the drip is uncertain and therefore variations in the initial structure are tested.

The first modelling set (set T) examines different initial crustal thicknesses. For this purpose, each model in the set has a different crustal root amplitude and the initial topography is modified to produce isostatic balance in the crust. The latter assumes that the timescales for crustal isostasy are much lower than the timescales of lithosphere removal, as suggested by previous geodynamic studies that use short computations to generate isostatic balance (e.g., Currie and van Wijk, 2016). In these models the mantle lithosphere is displaced by the crustal root keeping its same thickness (80 km) so the amplitude of the LAB deflection changes according to the variations in crustal root amplitude. Since the mantle lithosphere is cooler and denser than the sub lithospheric mantle, this deflection is gravitationally unstable and triggers lithosphere dripping as in previous models.

Set T consists of models T1, T2, T3, T4, and T5 (including the reference model T3), which have initial crustal root amplitudes of 10, 20, 30, 40 and 50 km, respectively. Snapshots of the density structures and the corresponding surface expressions at different time-steps are shown in figures 4.2 and 4.3. For the rest of the models in this work surface heat flow is also calculated as an indicator of crustal thinning after removal because it is another surface expression that could be measured in the SNSM. The temporal variations of topography, Bouguer gravity anomaly and surface heat flow in the perturbed are shown in figure 4.4.

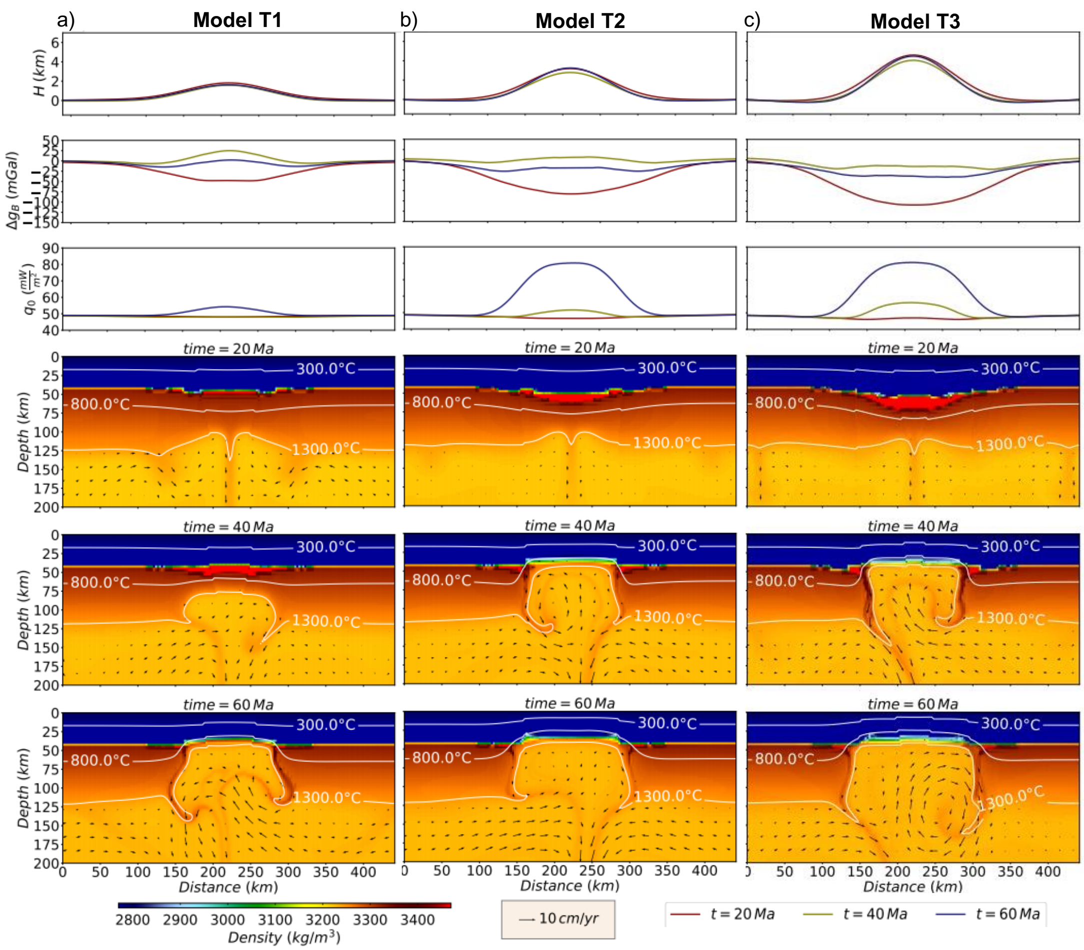

Figure 4.2: Modelling results for (a) model T1 ($R = 10$ km), (b) model T2 ($R = 20$ km) and (c) model T3 ($R = 30$ km) (reference), including snapshots of density structures and profiles of topography (H), Bouguer gravity anomaly (Δg_B) and surface heat flow (q_0), at times before, during and after the main lithosphere removal episode. Models explore the effect of different initial thickenings in the perturbed region (R) (consisting of an imposed crustal root and initial topography).

All the models of set T show a similar qualitative behaviour. First, the perturbation in the LAB grows and the dripping mantle lithosphere material reaches the bottom boundary where it spreads. The local drip of the mantle lithosphere under the perturbed region leaves a gap in the mantle lithosphere which is filled by upwelling sublithospheric mantle. While the mantle lithosphere is progressively removed, heat from the sublithospheric mantle increases the temperature of the crustal root inducing its eclogitization. As the crustal root turns into eclogite it exerts a downward force over the crust because of its negative buoyancy. At this stage, the densified crustal root (due to the eclogitization phase change) cannot sink because the mantle lithosphere underneath acts as a barrier prohibiting its dripping (e.g., density structure showing eclogitized crustal root in red in figure 4.2*b* at 20 Ma). However, the localized mantle lithosphere drip under the perturbed region continues until the sublithospheric mantle rises and reaches the Moho. Then, there is complete removal of the eclogitized crustal root followed by localized upwelling of buoyant sublithospheric mantle which fills the space left by the crustal root. The time of detachment of the crustal root is defined as the time in which the eclogitized crustal root is not longer in direct contact with the base of the non-eclogitized lower crust.

The general dynamics of all the models is similar because it involves mantle lithosphere dripping, followed by crustal root removal. However, there are significant differences in timescales and magnitudes of removal. When there is a thicker crustal root (e.g., Model T5), the mechanism occurs faster because of two reasons. First, the mantle lithosphere instability has a bigger amplitude so it has more available negative buoyancy, resulting in a faster instability growth. Second, the crustal root is also thicker so its bottom is deeper (where pressure is higher), resulting in faster eclogitization because the root heats more quickly. For instance, in model T5 (root thickness of 50 km) complete drip and root detachment occurs within 20 Ma, while in model T1 (root thickness of 10 km) it takes about 60 Ma. However, when the root is smaller (e.g., 10 km in model T1) its removal is less abrupt and there can be a significant time difference between the onset of root removal and its complete detachment. For example, for model T1, the onset of root detachment is at about 50 Ma but its complete removal occurs about 10 Ma later. The explanation for the latter is that when the amplitude of the perturbation is lower, its growth rate is also slower, and complete removal takes longer as reported by Houseman et al. (1981). Even if the crustal root fully reacts to form high density eclogite, if the mantle lithosphere is present below, it acts as a barrier preventing or significantly delaying root removal. Consequently, crustal root removal is promoted if there is also rapid mantle lithosphere dripping.

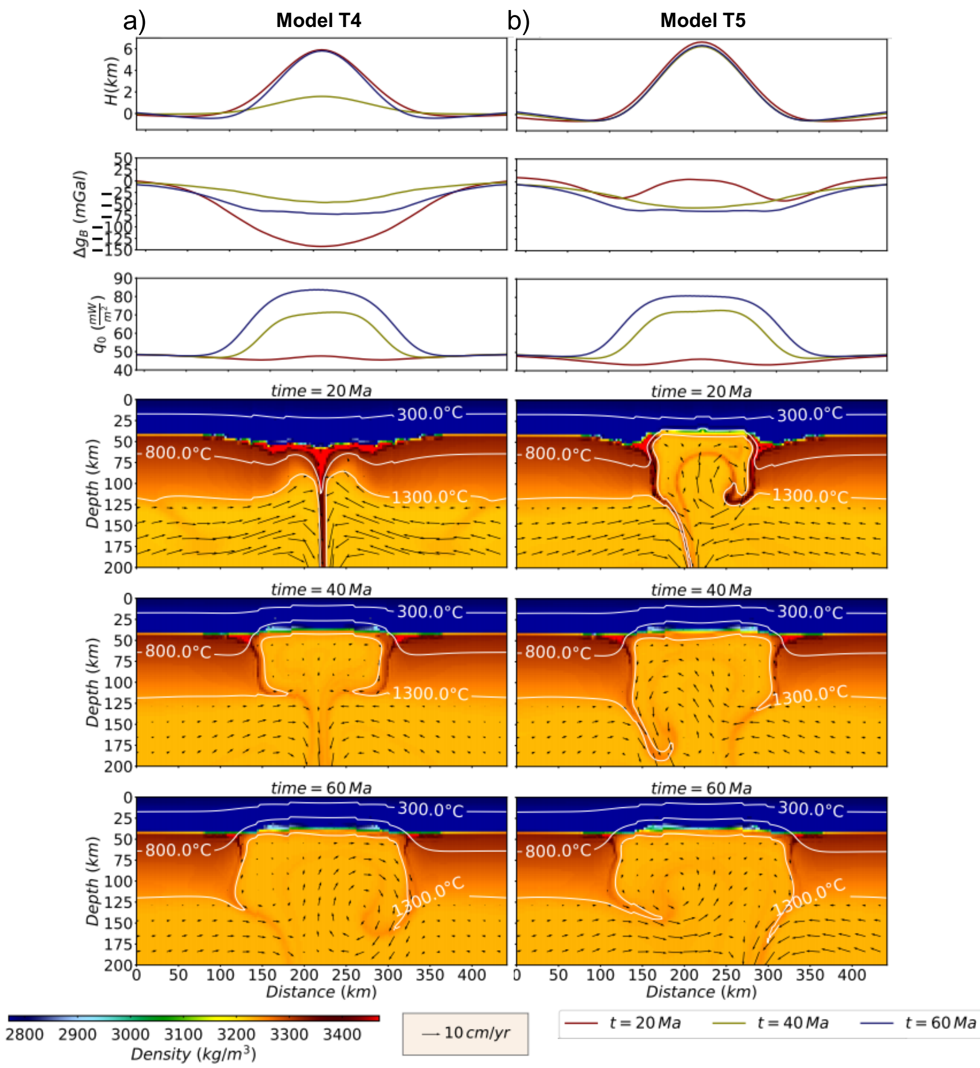

Figure 4.3: Modelling results for (a) model T4 (R = 40 km) and (b) model T5 (R = 50 km), including snapshots of density structures and profiles of topography (H), Bouguer gravity anomaly (Δg_B) and surface heat flow (q_0), at times before, during and after the main lithosphere removal episode. Models explore the effect of different initial thickenings in the perturbed region (consisting of crustal root and initial topography).

In models with higher initial thickness there is more lithosphere material removed because regardless of the initial thickness, the whole crustal root and mantle lithosphere in the central region are removed. Because models with an initially thicker crust also have higher initial topographies that are imposed to enforce initial isostasy, models with initially thicker crusts continue to have thicker crusts even after complete crustal root removal. When the support from the crustal root is removed, the elevated crustal material tends to sink. However, while in models with large initial topographies (e.g., model T5 with a maximum initial topography above 7 km), the elevated crustal material sinks producing a small crustal root in the end, in models with small initial topographies (e.g., model T1 with a maximum initial topography above 1.5 km), the load of the topographic relief is supported by mantle upwelling and the elevated crustal material does not sink.

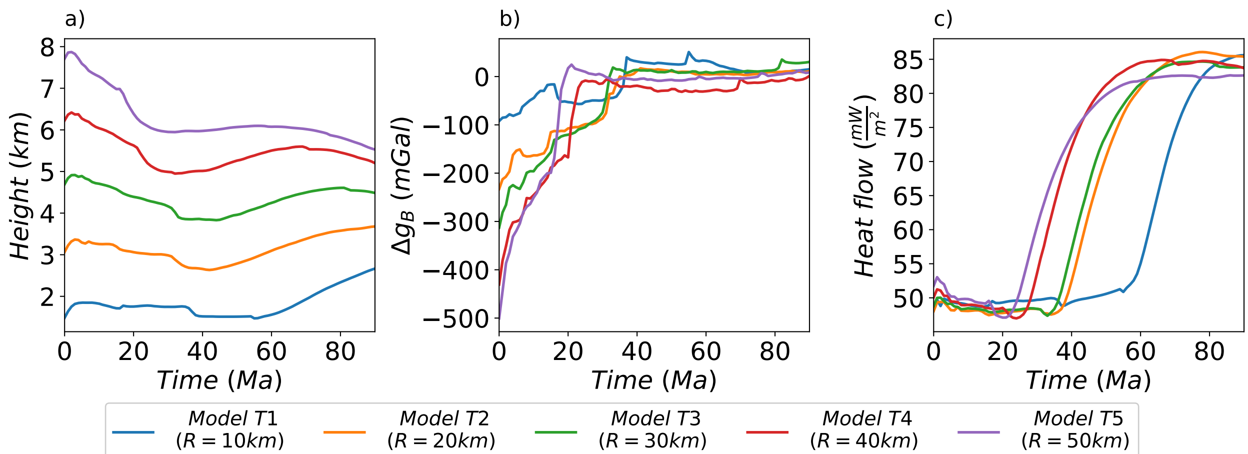

Figure 4.4: Time variation of surface observables, averaged over a 100 km width centred in the perturbed region, for modelling set T. (a) Surface topography. (b) Bouguer gravity anomaly. (c) Surface heat flow. R is the initial amplitude of the crustal root. The initial topography is set to be in isostatic balance with the corresponding root. Time (Ma) corresponds to the modelled time from the beginning to the end of the simulation.

The modelled topography (figure 4.4*a*) shows that at the beginning, there is subsidence related to the mantle lithosphere drip and crustal eclogitization relative to the initial topography. Subsidence continues until the complete detachment of the crustal root. Then, as the sub-lithospheric mantle rises to fill the gap left by the removed material, the surface undergoes uplift. The amount of uplift after crustal root removal is quantified with respect to the elevation right after root removal, which is the resultant elevation after the first phase of subsidence. The presence of a greater amount of high density material in models with thicker roots produces faster drips and results in more subsidence in the removal phase. For example, before crustal root detachment, the drip in model T5 produces subsidence of about

2 km relative to the initial topography whereas model T1 has minimal subsidence and topography has minor variations. Further, because models with a lower initial crustal thickness in the central region (e.g., Model T1) also have a lower initial topography (2 km) and the local crustal load is smaller (due to the imposed initial isostasy in the crust), vertical stresses from sub lithospheric mantle upwelling produce more uplift after root detachment in models with less initial crustal thickening. For example in model T1 there is more than 1 km of uplift relative to the elevation after root detachment while in model T5 uplift reaches only 100 m. In model T5 post-removal uplift is limited because vertical stresses from mantle upwelling act mostly to support the load of the initial crustal load in the central region (initial topography of above 7 km).

The initial magnitude of the Bouguer gravity anomaly in each model (figure 4.4*b*) depends on the amplitude of the crustal root. As expected, the larger the root, the more negative the gravity anomaly (initially Δg_B is about -500 mGal for model T5, whereas it is of -100 mGal for model T1). As eclogite is formed, and the mantle lithosphere instability starts to drip, the Bouguer gravity anomaly progressively increases until the onset of crustal root removal. That instant is characterized by an abrupt increase in the gravity anomaly (often reaching values above 0 mGal) as the crustal root rapidly detaches. The difference in time taken for removal is evident in the abrupt gravity anomaly increase which occurs sooner for models with larger crustal roots (e.g., at 20 Ma for model T5) and later for models with smaller crustal roots. After the removal episode, the gravity anomaly for all models is between 0 to +30 mGals. The small differences in the final magnitudes at later times are within the precision of the gravity anomaly calculations.

The evolution of surface heat flow is characterized by an increase from about 50 $\frac{mW}{m^2}$ (at the beginning) to more than 80 $\frac{mW}{m^2}$ (at the end) which is a consequence of mantle lithosphere and crustal root removal. In all the models, as the hot sublithospheric mantle rises filling the space left by the crustal root, it heats up the crust producing a significant increase in surface heat flow. Consequently, the timing of surface heat flow increase in set T clearly shows the effect of the initial lithosphere thickness in the time taken for complete removal. Figure 4.4*c* shows how surface heat flow starts increasing once complete removal has been achieved. This occurs at 60 Ma for model T1, at about 40 Ma for models T3 and T4, and close to 20 Ma for models T1 and T2. As expected, results indicate that there is higher surface heat flow in models where initial crustal thickness in the central region is lower, because in these cases the crust is also thinner in the end. For instance, model T1 reaches about 85 $\frac{mW}{m^2}$ with a final crustal thickness of about 31 km, while in model T5 the final surface heat flow is close to 80 $\frac{mW}{m^2}$, with a final crustal thickness of about 38 km.

The behaviour of surface heat flow before crustal root removal is characterized by a decrease due to the crustal thickening induced by the downward pull of the mantle lithosphere drip and the densified crustal root. The initial decrease in surface heat flow tends to be larger for models with an initially thicker crustal root and a larger perturbation in the LAB (e.g., model T5) because as the crustal root turns into eclogite there is more dense material exerting a downward pull. For these models, the phase of heat flow decrease is shorter because crustal root removal occurs sooner, allowing less time for drip-induced crustal thickening. However, the differences in the total amount of surface heat flow decrease before crustal root removal caused by the initial thickening in the central region are small (within 5 $\frac{mW}{m^2}$).

Results from model set T show that a lithosphere dripping episode with eclogitization and removal of a crustal root can provide support for the load of high topographies for long timescales (e.g., 50 Ma after removal in model T5), producing crustal thinning, increasing surface heat flow, and leading to a prominent increase in the Bouguer gravity anomaly. The main findings are:

- If the initial crustal thickness in the central region is higher, the growth rate of the perturbation in the LAB is higher allowing for an earlier crustal root removal.

- Initial lithosphere thickness has an important influence on the resultant topography, the post-drip uplift, and the surface heat flow. If the initial thickness is higher, the final elevation is higher, there is less uplift, and final surface heat flow is lower (and *vice-versa*).

- In all the studied cases, mantle upwelling could hold the final topographies producing at least some uplift (from about 100 m to more than 1 km relative to the elevation right after crustal root detachment). The latter is accompanied by crustal thinning due to the removal of the root and subsequent upward stresses from the rising sub lithospheric mantle.

- Post-removal mantle upwelling produces an increase in surface heat flow as the hot sub lithospheric mantle gets in direct contact with the crust.

- The final magnitude of surface heat flow is higher for models with initially thinner crusts (e.g., model T1 with a crustal root of 10 km) because after root removal, models with an initially thinner crust end up with a thinner final crust (and *vice-versa*), and because when the crust is locally thinner, the final surface heat flow is higher (heat transfer from the mantle to the surface is easier). However, the difference in the final surface heat flow produced by the initial thickness of the crust is small (e.g., $<5\ \frac{mW}{m^2}$ of difference between models T1 and T5 which have a difference of 40 km in the initial thickness of the crust).

- While initial lithosphere thickness produces changes in the increase rate of the Bouguer gravity anomaly and its total increased magnitude, it does not seem to affect the final magnitude of the Bouguer gravity anomaly which is between 0 to +30 mGal for all the cases studied. These values are significantly lower than the observed Bouguer gravity anomaly in the study region which is above 100 mGal.

Models T2, T3 and T4 follow the same trends and behaviours as models T1 and T5 but with intermediate magnitudes. Model T3 is used as a reference for the rest of the models in the chapter because it exhibits an intermediate behaviour in which the initial and final average elevation is between 4 and 5 km. Thus, the initial lithosphere thickness in the elevated region is not unrealistically high, and it is enough to produce a final topography which is within the range of the SNSM observations. Ramírez et al. (2020) report that in the Jurassic, there was continental arc magmatism and that the crustal thickness in the region was about 64 km. The latter is comparable to the 70 km initial thickness used in model T3.

4.4 Lateral Compression

Previous plate kinematics studies in the Caribbean show that there has been significant convergence between the Caribbean and South American plates after the late Cretaceous, including recent oblique convergence in northern South America (e.g., Müller et al., 1999; Pindell and Dewey, 1982; Pindell et al., 2005; Pindell et al., 2006). However, plate reconstructions by Müller et al. (1999) suggest that substantial variations in convergence rates between the North American and South American plates in the last 83 Ma have produced significant variations in the convergence rates between the Caribbean and the South American plates with values as low as 1.2 ± 0.9 mm/year (in the period between 38.4 Ma to 25.8 Ma ago) or as high as 9.6 ± 3.1 mm/year (in the period between 25.8 Ma to 9.5 Ma ago).

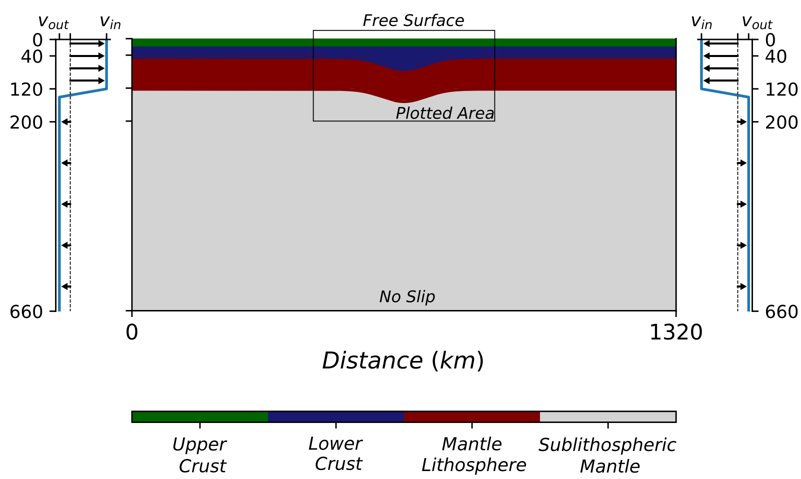

Figure 4.5: Modelling setup used for models with horizontal compression. The setup is the same as in figure 4.1 but the lateral boundaries are modified to produce inflow in the lithosphere with a compression velocity of V_{in}. Outflow is imposed in the lower part of the lateral boundaries at a velocity of V_{out} to balance the inflow on top. In the models the magnitude of V_{in} is varied and V_{out} is modified accordingly to preserve mass within the model domain.

Therefore, it is challenging to quantify with certainty the exact convergence rates and their duration in the SNSM region. Moreover, considering that deformation produced during tectonic plate convergence is accommodated through faults in plate boundaries and their surroundings, the exact amount of lateral compression in the region of the SNSM is difficult to determine. Consequently, the approach in this study is to test different rates of lateral compression and their effect on lithosphere removal and its associated surface expressions.

This is achieved by modifying the lateral velocity boundary conditions to impose inflow in the upper 120 km to simulate compression. The inflow is balanced by outflow below 120 km in order to keep the mass constant within the model domain (4.5).

This section presents model set CV ("compression velocity") which consists of two models (CV1 and CV2). These models have the same setup as model T3 but there is lateral compression at rates of 0.1 mm/yr and 0.5 mm/yr for CV1 and CV2, respectively. Snapshots of the density structure and profiles of topography, Bouguer gravity anomaly, and surface heat flow are shown in figure 4.6. The time evolution of the surface expressions is shown in figure 4.7. Model CV1 has no significant difference from model T3, suggesting that a compression velocity of 0.1 mm/yr is negligible. Similarly, when the compression velocity is increased to 0.5 mm/yr (model CV2), there are no significant fluctuations in the evolution of the Bouguer gravity anomaly over the central region (figure 4.7*b*). However, there are clear differences in the evolutions of topography and surface heat flow (figures 4.7*a*, and 4.7*c*), as well as in all the profiles of all surface expressions (profiles in figure 4.6*b*), including the Bouguer gravity anomaly. In model CV2 there is lithosphere dripping followed by eclogitization and removal of the crustal root such as in model T3 (section 4.3) but at later times, lateral compression produces crustal thickening at the sides resulting in the onset of a new removal (caused by eclogitization) close to the right boundary (figure 4.6*b*). The latter results in non-symmetrical profiles of topography, gravity anomaly and surface heat flow, with local alterations at the site of the secondary removal.

In model CV2, lateral compression produces crustal contraction, thickening and uplift. In the first 40 Ma, uplift is moderate because it is restricted by the simultaneous downward pull caused by the mantle lithosphere and eclogite drip. However, when the crustal root detaches and the downward stresses are released, there is a prominent uplift episode of about 3 km at a constant rate of about 0.18 mm/yr, and the central region reaches a maximum elevation of 9.6 km at 53 Ma. This is followed by subsidence (at about 0.12 mm/yr) until the end of the modelling time producing a final average topography of about 5.5 km.

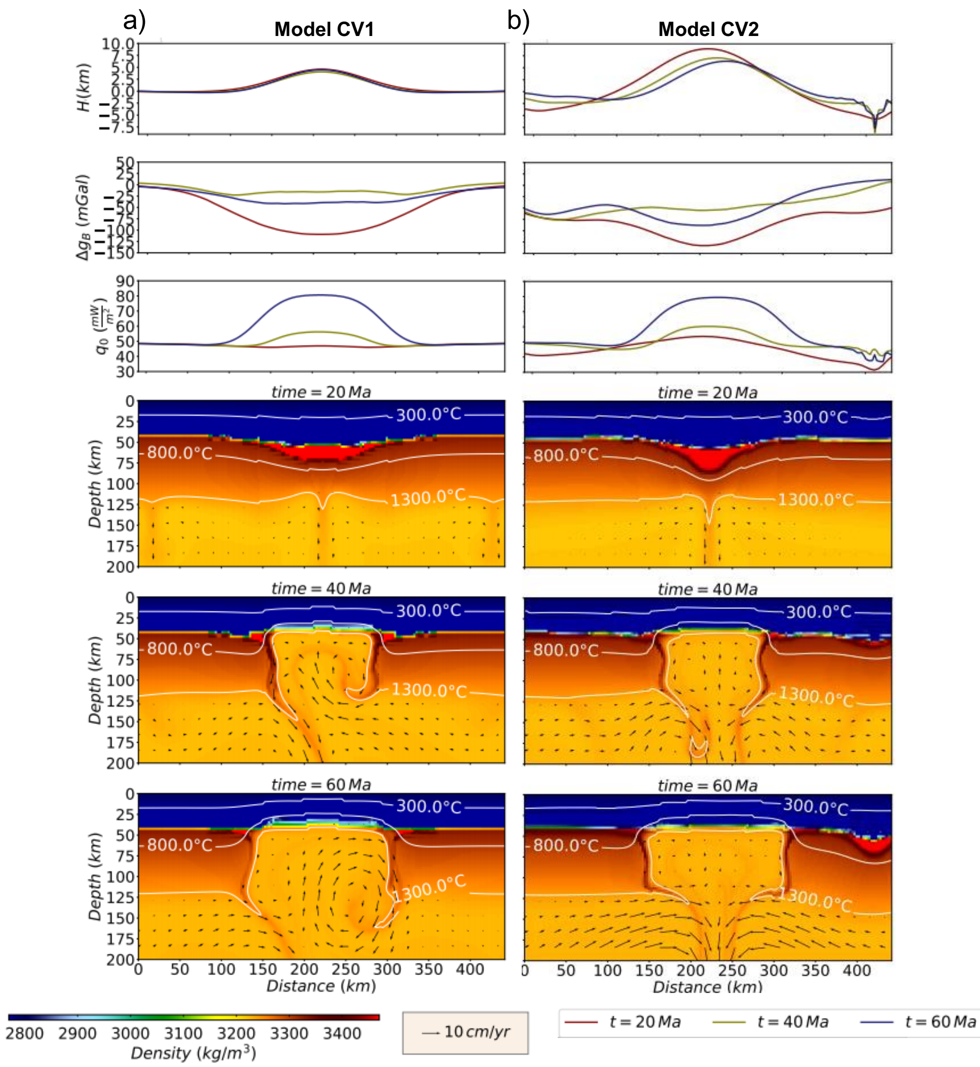

Figure 4.6: Modelling results for (a) model CV1 ($v_c = 0.1$ mm/yr) and (b) model CV2 ($v_c = 0.5$ mm/yr), including snapshots of density structures and profiles of topography (H), Bouguer gravity anomaly (Δg_B) and surface heat flow (q_0), at times before, during and after the main lithosphere removal episode. Models explore the effect of different compression velocity magnitudes (v_c) in fully viscous models.

The behaviour of surface heat flow in the first 40 Ma is similar as in the reference model but it is about 4 $\frac{mW}{m^2}$ higher. Then, after crustal root removal, surface heat flow increases more rapidly reaching a maximum of 85 $\frac{mW}{m^2}$ approximately 20 Ma before than in the reference model. This suggests that lateral compression can promote crustal root detachment. This is followed by a small decrease of surface heat flow as crust compressed and thickened by 12 km at the site of the secondary drip, leading to a final value of less than 80 $\frac{mW}{m^2}$ in the central region (figure 4.7). This occurs because the average value in the centre is slightly affected by the close heat flow alteration at the secondary drip.

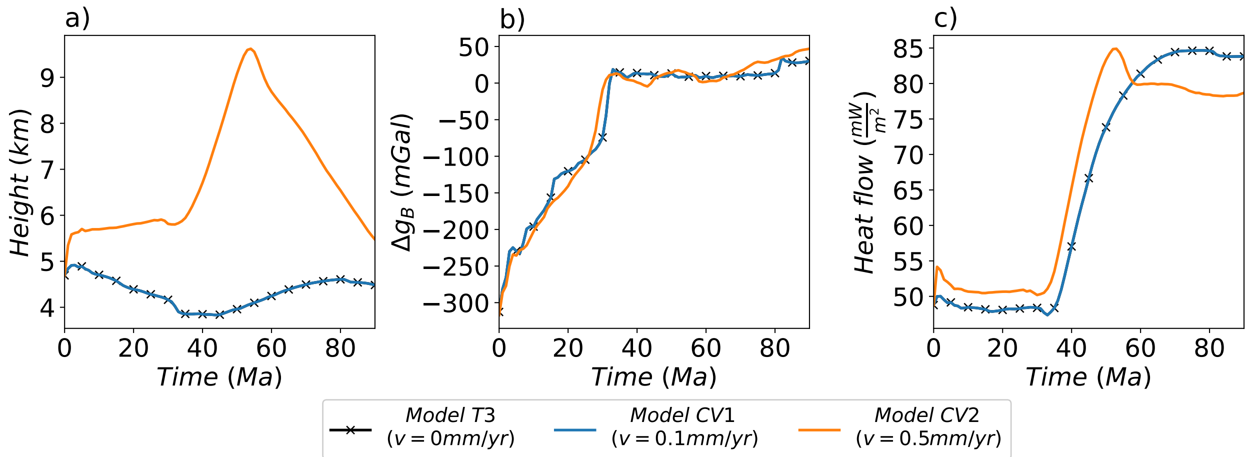

Figure 4.7: Time variation of surface observables, averaged over a 100 km width centred in the perturbed region, for models CV1 and CV2. (a) Topography. (b) Bouguer gravity anomaly. (c) Surface heat flow. Results of model T3 (which uses zero compression velocity) are shown as a reference (black). Time (Ma) corresponds to the modelled time from the beginning to the end of the simulation.

Results from model CV2 suggest that lateral compression at a low rate (0.5 mm/yr) together with the secondary drip produce some crustal thickening, slightly reducing surface heat flow in the centre (by about 5 $\frac{mW}{m^2}$). However, the heat flow increase produced by the lithosphere dripping and root removal should still be prominent (increase of at least 25 $\frac{mW}{m^2}$). Also, the results suggest that lateral compression at 0.5 mm/yr does not produce significant differences in the Bouguer gravity anomaly evolution generated by the drip. On the other hand, model CV2 shows a large (>3 km) increase of the surface elevation. This is caused by the absence of plastic deformation in the models which should restrict the formation of high topographies by compression. This is because when the crust experiences compression there is faulting and shortening in the shallow structure and deformation is accommodated horizontally. This suggests that a more realistic model using lateral compression may require limiting the viscosities using a frictional-plastic criterion to account for plastic deformation. This is tested in the following sections. The concluding remarks of model set CV are:

- A compression velocity of 0.1 mm/yr produces negligible effects in surface observables compared to a model with no compression.

- Lateral compression above 0.5 mm/yr has a clear effect on topography and surface heat flow but it has a small influence in the Bouguer gravity anomaly.

- Further work including plastic deformation is required to quantify the importance of lateral compression on surface heat flow and topography and to explore the effect of higher compression velocities.

4.5 Frictional-Plastic Rheology

A common approach in numerical modelling of lithosphere dynamics and crustal deformation is to use a frictional-plastic yield criterion to limit the unrealistically high viscosities that result from fully viscous power-law formulations (e.g., Beaumont et al., 2010; Currie et al., 2015; Heron et al., 2019; Naliboff et al., 2017). This also allows for realistic deformation of the shallow lithosphere, including the formation of weak zones and faults. The models in this section follow te setup of Model T3, but the viscosity is limited using the Drucker Prager yield criterion in 2D (2.9), which is introduced in section 2.3.2.

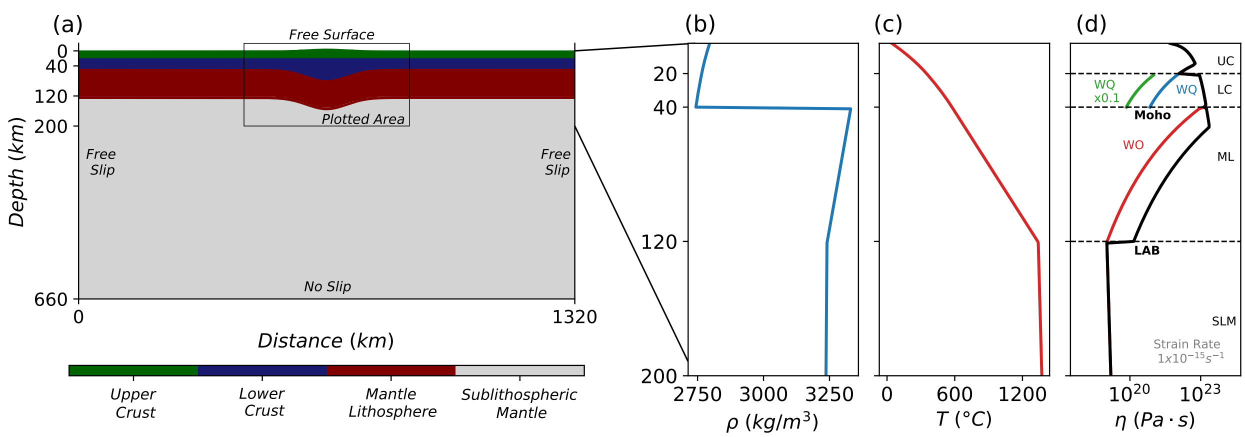

Figure 4.8: (a) Modelling set up used in viscoplastic tests. Only the enclosed region is shown in the following model figures. (b) Reference density structure (at the sides of the domain). (c) Initial temperature conditions. The continental geotherm is stretched in the thickened region keeping the Moho temperature constant. (d) Reference viscoplastic effective viscosity (black line). The viscous rheologies used for the reference are explained in the text. Coloured lines show other viscous rheologies used. WQ: Wet Quartzite (Gleason & Tullis, 1995) (for the lower crust), WO: Wet Olivine (Karato & Wu, 1993) (for the mantle lithosphere).

The models in this section test the strain weakening strategy, and its effect on cohesion and the friction angle. The reference configuration for the models in this section is shown in figure 4.8, which is the same as in figure 4.1, but in this case, the viscous strengths are limited using equation (2.9) accounting for brittle behaviour, with linear strain weakening applied when the cumulative strain varies between 0.5 and 1.5. This results in weakening in the friction angle and cohesion from 15° to 2° and from 20 to 2 MPa, respectively, following previous approaches (e.g., Currie et al., 2015; Huismans and Beaumont, 2007; Krystopowicz and Currie, 2013; Warren et al., 2008).

4.5.1 Strain Weakening: Plastic Strain vs. Total Strain

In the models in this section, strain weakening is applied either when the total or plastic strain changes from 0.5 to 1.5. Both strategies are tested to verify their importance in the results. Set SW (”strain weakening”) consists of models SW1 and SW2, which use plastic and total strain as a reference for strain weakening, respectively.

The model results and the evolution of surface observables for these models are shown in figures 4.9 and 4.10. These models include a compression velocity of 0.1 mm/yr. Firstly, the effect of plastic behaviour is evident in the topographic profiles in figure 4.9. With plasticity, crustal strain was localized in fault zones, resulting in subsidence and vertical motions along the weak regions. This causes the formation of graben-type structures on top of the lithosphere drip. Consequently, before the total removal of the crustal root (at about 30 Ma) in models with plasticity (models SW1 and SW2), the negative buoyancy of the mantle lithosphere and the eclogite produced a collapse of the topography to almost 0 km elevation. After the removal, mantle upwelling together with lateral compression contribute to produce uplift reaching 1 km of average elevation.

Also, as observed in previous models, the time of the sudden increase in surface observables (topography, Bouguer gravity anomaly and surface heat flow) occurs at the time of detachment of the crustal root. This occurs earlier for models of set SW than for the reference model (Model T3). This shows that a lateral compression of 0.1 mm/yr can contribute to accelerate the drip dynamics by about 10 Ma. This is fundamentally different from results of model CV1 in section 4.4 (without plasticity) which suggests that the effect of lateral compression at 0.1 mm/yr is neglectable, but agrees with model CV1 (with compression at 0.5

mm/yr) which also shows that lateral compression accelerates drip dynamics. This suggests that frictional-plastic rheologies are more sensitive to lateral compression.

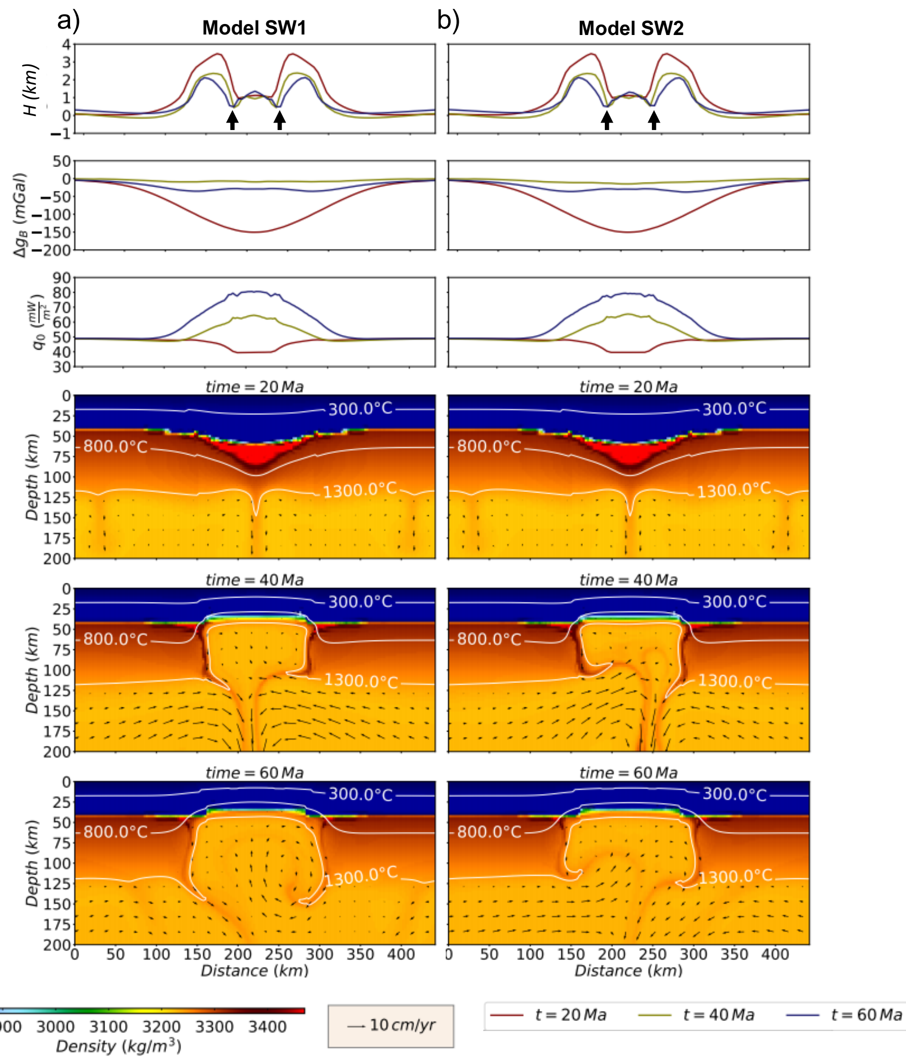

Figure 4.9: Modelling results for (a) model SW1 and (b) model SW2, including snapshots of density structures and profiles of topography (H), Bouguer gravity anomaly (Δg_B) and surface heat flow (q_0), at times before, during and after the main lithosphere removal episode. Models explore the effect of using either plastic strain (SW1) or total strain (model SW2) to produce strain weakening. Location of weak zones allowing brittle fracturing are shown by black arrows in the topographic profiles.

Aside from the difference in timing, models in set SW exhibit only small variations in the Bouguer gravity anomaly suggesting that for this observable, the effect of plastic deformation and compression at 0.1 mm/yr is not significant. At the end of the modelling time the gravity anomaly converges to +30 mGals for all models, including model T3. However, in the two models of set SW the rapid collapse of the initial topography with the simultaneous plastic deformation in the crust (contraction and thickening) produced by compression results in a decrease in surface heat flow in the first 30 Ma by more than 10 $\frac{mW}{m^2}$. Even though surface heat flow increases after root removal, as in previous models, crustal thickening of about 2 km (relative to the final crustal thickness of model T3) caused by compression lead to slightly lower final heat flow magnitudes (less than 5 $\frac{mW}{m^2}$ lower).

A comparison of models SW1 and SW2 show that the difference between the use of plastic strain or total strain as a reference to apply strain weakening in the models is negligible. For instance, the evolution of surface expressions is almost equal and only shows minor differences at late modelling times (figure 4.10). This suggests that most of the strain taking place in the models occurs in the plastic regime. Hence, models in the following sections continue to use plastic strain as a reference (such as in model SW1).

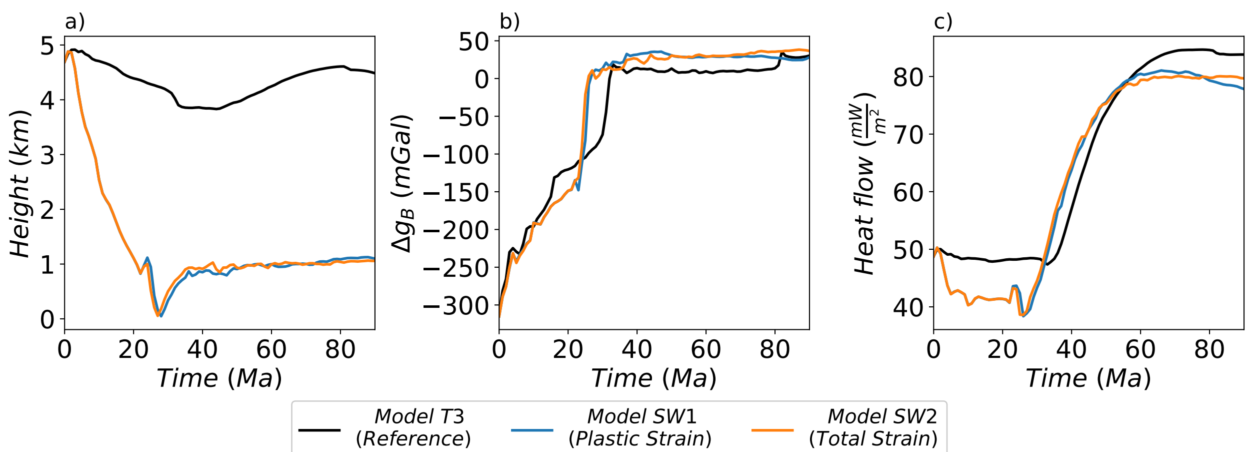

Figure 4.10: Time variation of surface observables, averaged over a 100 km width in the centre of the model, for models SW1 and SW2. Model T3 is shown as a reference (black). (a) Topography. (b) Bouguer gravity anomaly. (c) Surface heat flow. Time (Ma) corresponds to the modelled time from the beginning to the end of the simulation.

The effect of plasticity significantly affects the evolution of topography and surface deformation during a lithosphere removal episode. For example, the weakening of the upper crust limits the formation of high topography because it allows for the accommodation of deformation through weak zones. Moreover, models suggest that a lithosphere removal episode in the SNSM could produce faults in the crust that could possibly be observed in the surface as physical evidence. The formation of these faults enhances surface subsidence prior to root removal and the subsequent mantle upwelling cannot recover the elevation lost. The maximum surface elevation after root removal is of about 1 km in models SW1 and SW2 (considering plasticity), which is not compatible with the observations in the SNSM, which has a maximum height of more than 5 km.

4.5.2 Cohesion

In this section, two models are presented to test the effect of cohesion in the formulation for plasticity under a greater rate of compression. Cohesion is a parameter describing the shear strength of rocks in the absence of normal stresses (C in equation 2.9). Model P1 has the same configuration and setup of model SW1 but lateral compression is increased to 1 mm/yr to explore the behaviour of plasticity under more significant lateral stresses. Additionally, another model with the same setup as model P1 is computed but without strain weakening in cohesion (Model P2), meaning that it has a constant value of 20 MPa throughout the model evolution.

The topographic profiles in figure 4.11 show that the increased lateral compression produces more surface deformation, generating more faults in the upper crust. These topographic irregularities are also reflected in the surface heat flow patterns (figure 4.11). The final thickness of the crust in models P1 and P2 is 6 km higher than in model SW1 because the increase in lateral compression leads to more crustal contraction and thickening. The change in final crustal thickness is reflected in all the surface expressions in figure 4.12. In comparison to model SW1, models P1 and P2 exhibit surface elevations which are 1 km higher (reaching 2 km), Bouguer gravity anomalies which are 60 mGals lower (reaching -40 mGals), and surface heat flows which are 10 $\frac{mW}{m^2}$ lower (reaching 70 $\frac{mW}{m^2}$). This indicates that the magnitude of regional compression is significant and it is directly reflected in the magnitudes of surface observables.

There are no significant differences between the results of models P1 and P2, showing that strain weakening in cohesion is not important for the evolution of surface expressions. As expected, the main effect of strain weakening in cohesion is in plastic deformation. This can be observed in figure 4.11, where there are more topographic irregularities produced by shallow faulting in model P1 (figure 4.11b), than in model P2 (figure 4.11a).

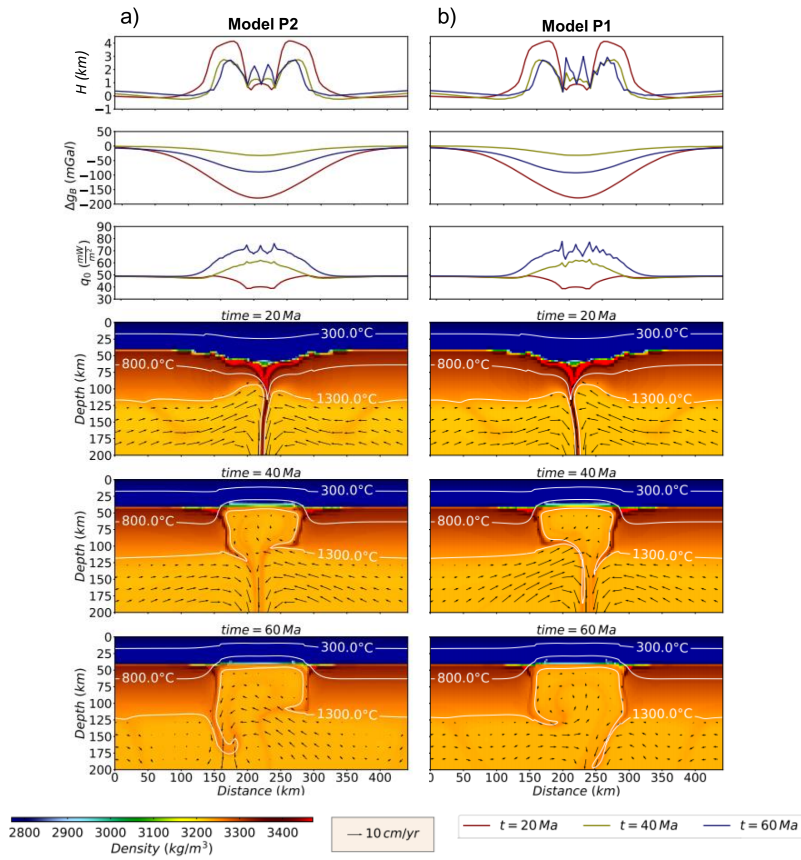

Figure 4.11: Modelling results for (a) model P2 ($C = 20 - 20$ MPa) and (b) model P1 ($C = 20 - 2$ MPa), including snapshots of density structures and profiles of topography (H), Bouguer gravity anomaly (Δg_B) and surface heat flow (q_0), at times before, during and after the main lithosphere removal episode. Models explore the effect of cohesion C in plastic deformation.

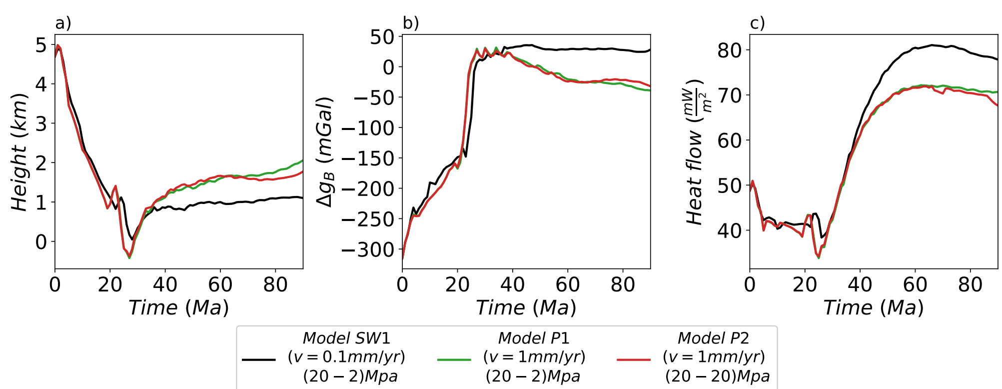

Figure 4.12: Time variation of surface observables, averaged over a 100 km width centred in the perturbed region, for models P1 and P2. Model SW1 is shown as a reference (black) (a) Topography. (b) Bouguer gravity anomaly. (c) Surface heat flow. Time (Ma) corresponds to the modelled time from the beginning to the end of the simulation.

However, the effect of an increased lateral compression is not compatible with the observations in the SNSM because even though the induced crustal thickening (by about 6 km) contributes to form higher topographies, it simultaneously decreases the gravity anomaly and surface heat flow. Hence, if the observations of simultaneous high gravity anomaly and high topography in the SNSM were caused by lithosphere removal, these results suggest two possibilities. Either lateral compression was low, producing little or no crustal thickening after the removal episode, or there has been not enough time for significant crustal thickening alter the event.

4.5.3 Friction Angle

This section presents the rest of the models of set P (models P3, P4 and P5), which have the same setup as model P1, but include modifications to test the effect of the friction angle in the formulation for plastic behaviour (ϕ in equation 2.9). This parameter describes the dependence of rock shear strength with normal stresses. In model P3, there is weakening in the friction angle from 15° to 5° when plastic strain changes from 0.5 to 1.5. Additionally, models P4, and P5, have constant friction angles of 15° and 30° respectively, without strain weakening. Figures 4.13, and 4.14 show the results of these models.

As seen previously, the most prominent effect of the friction angle is on shallow plastic deformation. When there is no weakening in the friction angle (e.g., model P4 or P5), the crust is more rigid, producing sharper fracture-like structures that reach the surface (figure 4.13*c*). Conversely, when there is strain weakening and the friction angle is reduced (e.g., models P1 and P3), fractures are smaller and less sharp, allowing for a more ductile deformation.

Figure 4.14 shows that the friction angle has only a small effect on the evolution of surface observables. There is a trend of lower average elevations when the friction angle is higher (about 300 m lower than model P1; figure 4.14*a*). This is produced by the presence of larger sharp faults at the surface. Also, variability in surface deformation tends to produce minor alterations in surface heat flow at later times. For example, after 50 Ma, there are fluctuations of less than 2.5 $\frac{mW}{m^2}$ in figure 4.14*c*. However, neither these effects nor the small variations in the Bouguer gravity anomaly, are significant for the purposes of this study.

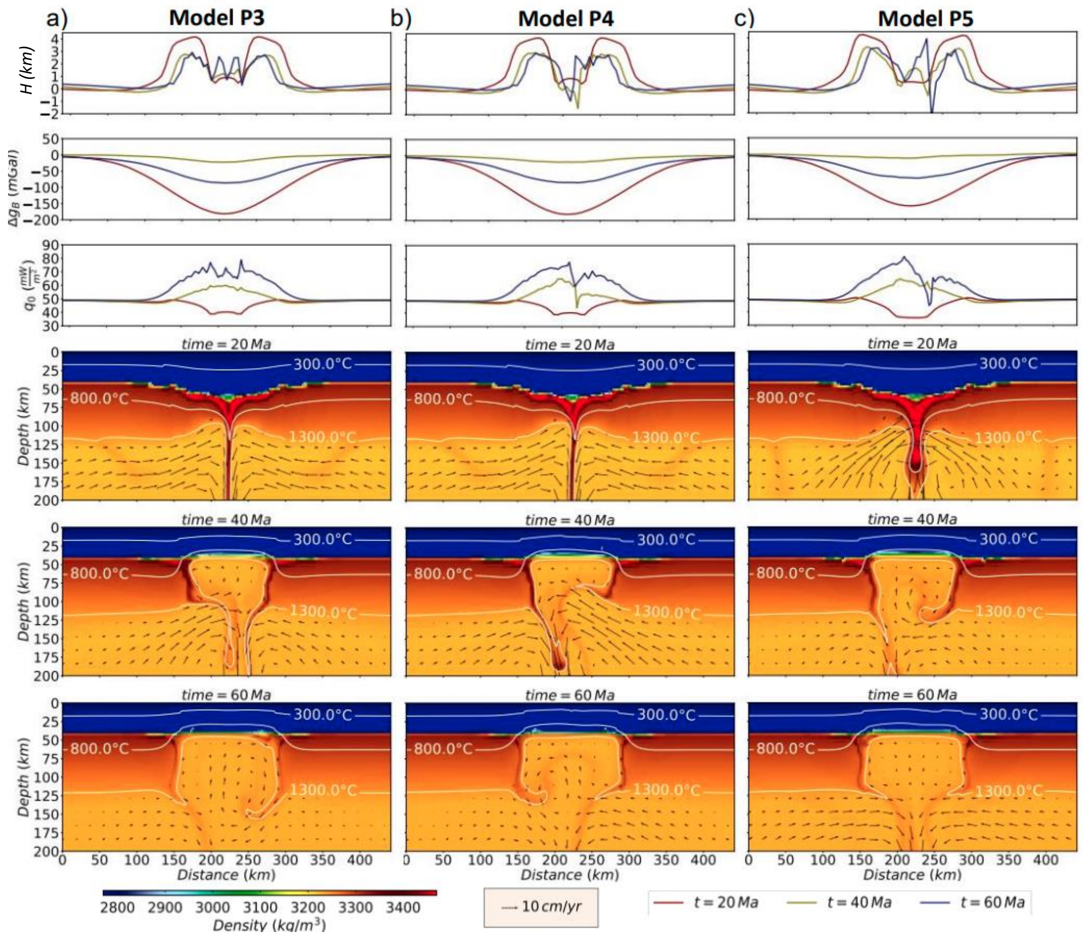

Figure 4.13: Modelling results for (a) model P3 ($\phi = 15° - 5°$), (b) model P4 ($\phi = 15° - 15°$), and (c) model P5 ($\phi = 30° - 30°$) , including snapshots of density structures and profiles of topography (H), Bouguer gravity anomaly (Δg_B) and surface heat flow (q_0), at times before, during and after the main lithosphere removal episode. Models explore the friction angle ϕ in plastic deformation.

Because the friction angle does not have a big impact on the model results, the rest of the models in this work use the standard configuration with strain weakening in the friction angle producing a decrease between 15° and 2° (such as in the reference model P1) which has been used successfully in multiple previous studies (e.g., Currie et al., 2015; Huismans and Beaumont, 2007; Krystopowicz and Currie, 2013).

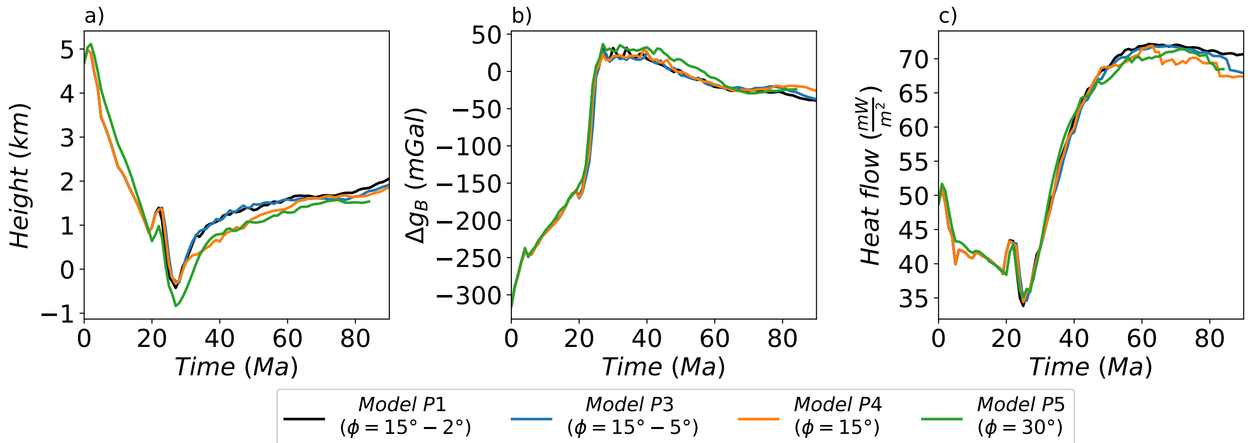

Figure 4.14: Time variation of surface observables, averaged over a 100 km width in the central region, for models P3, P4, P5 and P6, showing the effect of the friction angle ϕ of the plastic yield criterion. Results of model P1 are included as a reference. (a) Topography. (b) Bouguer gravity anomaly. (c) Surface heat flow. Time (Ma) corresponds to the modelled time from the beginning to the end of the simulation.

4.5.4 Summary

- Most of the strain weakening produced in the models is associated with plastic strain because there is no significant difference when using either the total strain or the plastic strain to generate strain weakening.
- Plasticity has a significant effect on the evolution of topography and surface deformation because it facilitates drip-induced subsidence through the formation of faults and/or weak zones, such that elevation cannot be recovered by the post-drip mantle dynamics.
- The cohesion, friction angle and reference strain for strain weakening only affect the amount of shallow faulting and local small topographic variations. These do not have a significant effect on the regional surface expressions or the dynamics studied.

4.6 Compression Rates in Viscoplastic Models

Previous models suggest that during lithosphere removal, high rates of lateral compression are not compatible with the observations of high topography together with a high positive Bouguer gravity anomaly (see section 4.5.2). This is because compression produces crustal thickening, which generates a decrease in the Bouguer gravity anomaly. However, it is not clear which magnitudes of lateral compression would still allow for a significant increase of the Bouguer gravity anomaly after crustal root removal and which magnitudes would hinder any increase. Hence, this section explores the effect of lateral compression magnitudes (imposed through the velocity boundary conditions) by introducing modelling set V. This set consists of models V1, V2 and V3, which use compression velocities of 0.5, 5, and 10 mm/yr respectively. The rest of the model parameters are the same as in model P1.

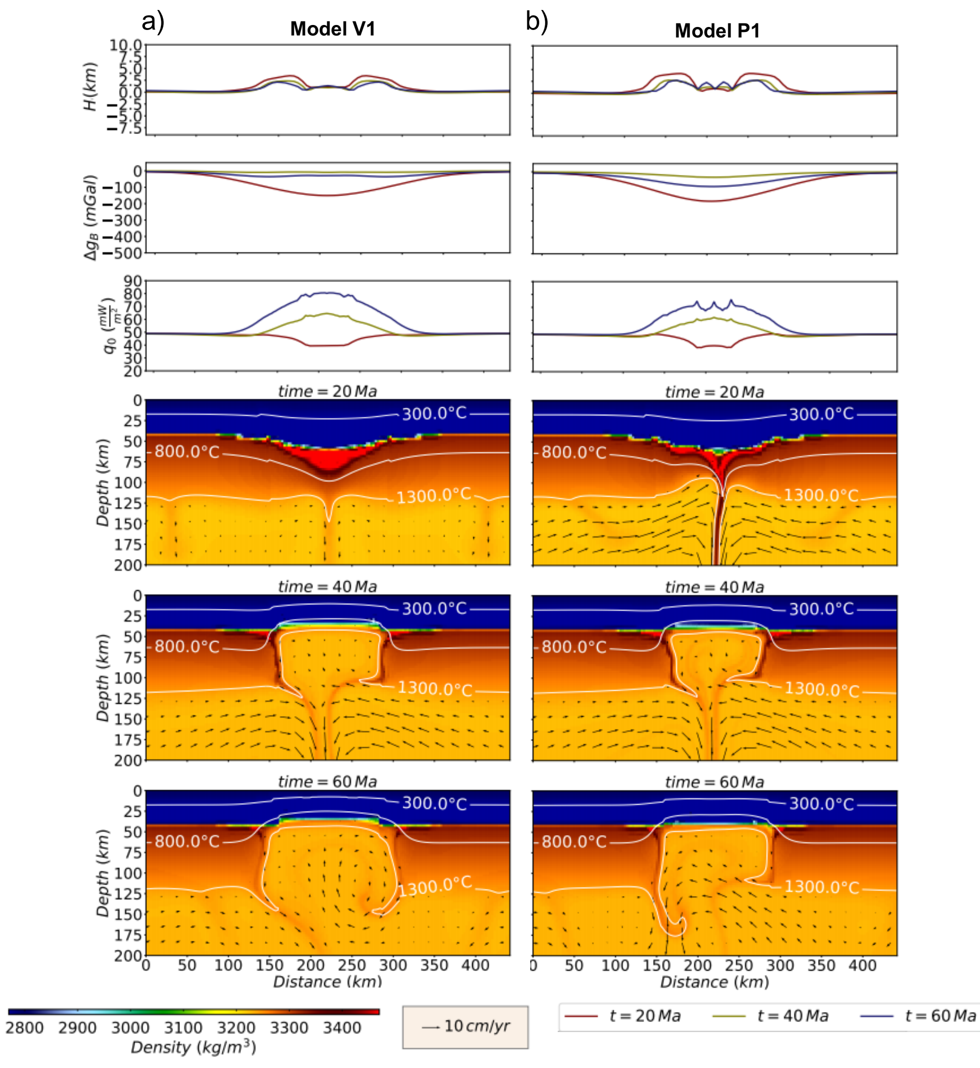

Figure 4.15: Modelling results for (a) model V1 ($v_{comp} = 0.5$ mm/yr) and (b) model P1 ($v_{comp} = 1.0$ mm/yr) as a reference, including snapshots of density structures and profiles of topography (H), Bouguer gravity anomaly (Δg_B) and surface heat flow (q_0), at times before, during and after the main lithosphere removal episode. Models explore the effect of different compression velocity magnitudes in viscoplastic models.

Results for set V are shown in figures 4.15 and 4.16. The evolution of surface observables is shown in 4.17 together with the results of models SW1 (0.1 mm/yr) and P1 (1.0 mm/yr) to have a complete set with different compression rates. The overall behaviour of model V1 is similar to the previous models with plasticity. Figure 4.17 shows that the surface expressions for model V1, with compression at 0.5 mm/yr, are intermediate between those of models SW1 (compression at 0.1 mm/yr) and P1 (compression at 1.0 mm/yr).

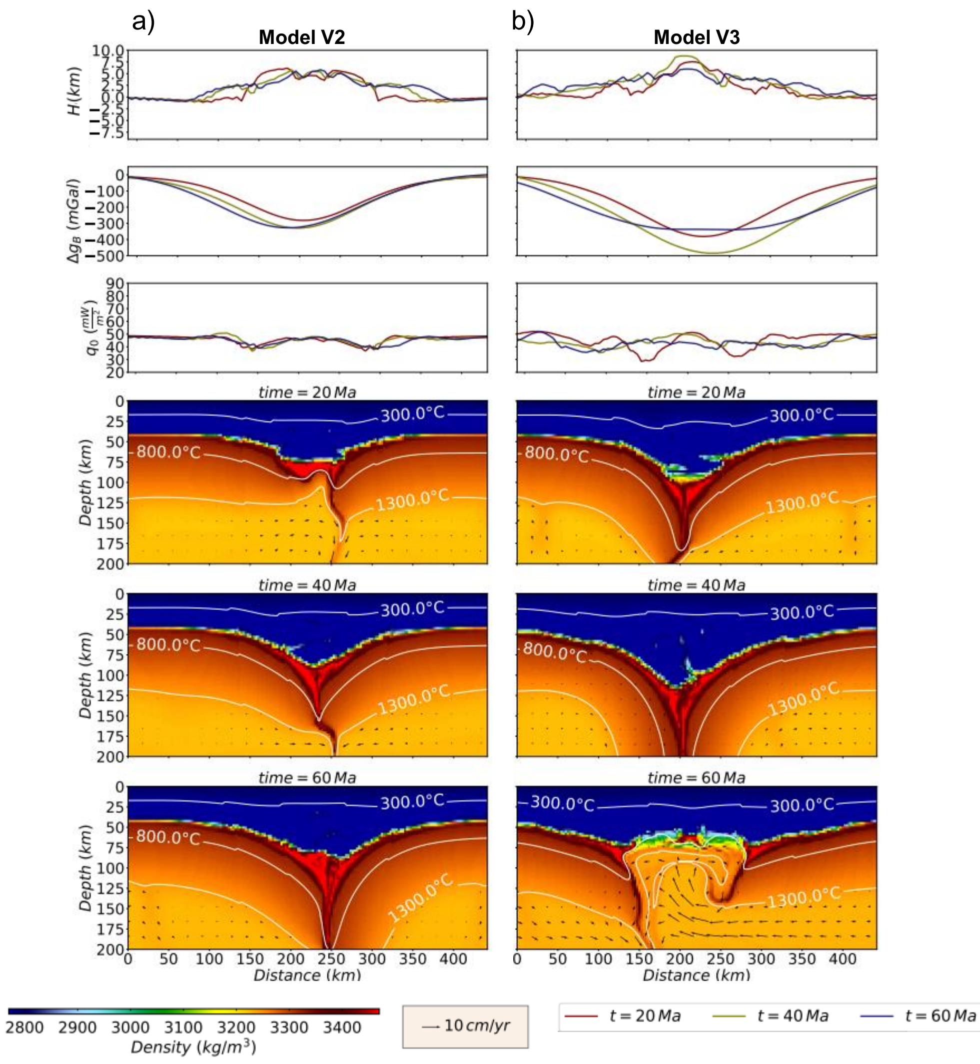

Figure 4.16: Modelling results for (a) model V2 ($v_{comp} = 5.0$ mm/yr) and (b) model V3 ($v_{comp} = 10.0$ mm/yr), including snapshots of density structures and profiles of topography (H), Bouguer gravity anomaly (Δg_B) and surface heat flow (q_0), at times before, during and after the main lithosphere removal episode. Models explore the effect of different compression velocity magnitudes in viscoplastic models.

In models V2 and V3 the compression rate is higher and produces a maximum crustal thickness of 88 km at 50 Ma and 113 km at 40 Ma, respectively. This leads to substantial surface uplift, producing high, wide, and rough elevations (figure 4.16). This is accompanied by rapid growth of the crustal root before its eclogitization. Only a small portion of the crustal root reaches the temperatures required for the phase change because the resultant root is formed by cooler crustal material from the sides that is pushed to the centre and forced to higher depths. Because the compression rate is rapid, there is not enough heating time to produce eclogitization in the lower crustal material entrained from the sides. The portion of eclogitized crustal material still detaches, leaving a gap in the lithosphere. However, in models V2 and V3, the remaining crust is considerably thick (final thickness of 59 km in model V2 and 63 km in model V3) and produces a highly negative Bouguer gravity anomaly (about -200 mGal for both models V2 and V3) as expected for an elevated region supported by Airy-type isostasy (i.e., when topography is balanced by changes in crustal thickness instead of density variations).

In model V2, progressive thickening leads to a minimum gravity anomaly of -315 mGal at 52 Ma. However, subsequent lower crustal eclogitization induces an increase in the anomaly to about -200 mGal. Then, at about 80 Ma there is complete removal of the eclogitized portion of the root. This produces a rapid decrease in the gravity anomaly to -240 mGal which can be observed as a small negative peak in figure 4.17*b*. On the other hand, because in model V3 lateral stresses produce considerably more crustal thickening before root removal, there is a faster decrease of the Bouguer gravity anomaly, which reaches -500 mGal at 43 Ma, followed by the detachment of the eclogitized material at 45 Ma. This produces a fast and significant increase in the gravity anomaly which quickly reaches -300 mGal. The subsequent sublithospheric mantle upwelling and crustal thinning (due to root detachment) produce a further increase in the gravity anomaly to -190 mGal. However, continued lateral compression generates further crustal thickening and a decrease in the gravity anomaly until the end (from -190 mGal to -230 mGal).

In the evolution of topography for model V2, progressive crustal thickening (88 km thick) produces a maximum elevation of 5 km at about 52 Ma. Then, the pull of the dense eclogite in the lower crust and the mantle lithosphere produce progressive subsidence until the complete removal of the eclogitized portion of the root at about 80 Ma. The latter produces a rapid uplift episode with maximum average elevation of 5.6 km. In model V3, the trend in the evolution of topography is the same but the increase in lateral compression accelerates the process considerably. For instance, full detachment of the eclogitized portion of the root occurs at about 45 Ma, producing a maximum peak elevation of about 9 km, followed by subsidence and equilibration at an average elevation of 4.5 km.

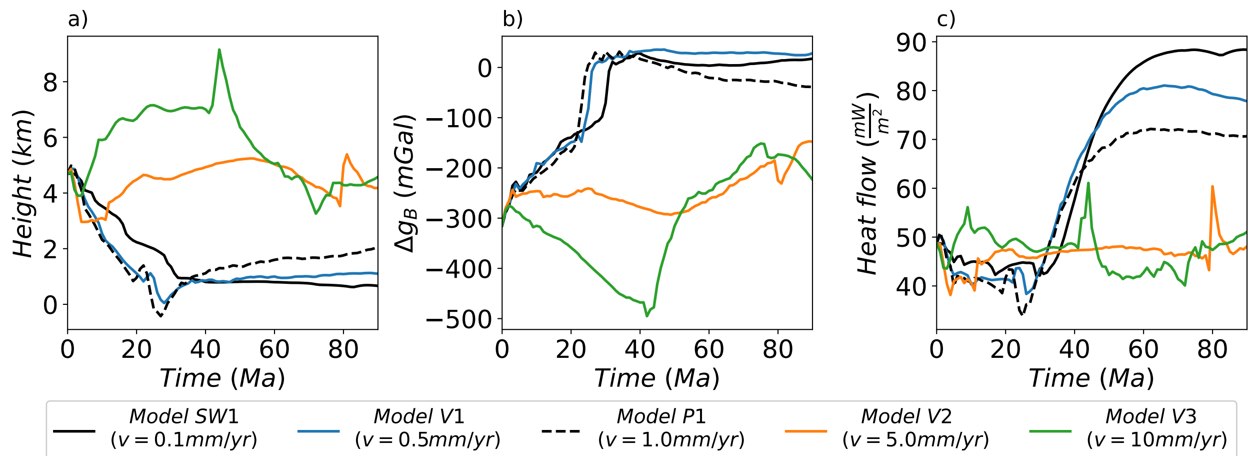

Figure 4.17: Time variation of surface observables, averaged over a 100 km width centred in the perturbed region, for modelling set V. (a) Topography. (b) Bouguer gravity anomaly. (c) Surface heat flow. Results of models P1 (Compression velocity of 1 mm/yr, in black dashed lines) and SW1 (Compression velocity of 0.1 mm/yr, in black) are shown as a reference. Time (Ma) corresponds to the modelled time from the beginning to the end of the simulation.

The crustal root removal events are marked by a strong peak in surface heat flow which occurs at 45 Ma and 80 Ma for models V3 and V2, respectively. These peaks consist of a rapid increase of more than 10 $\frac{mW}{m^2}$, reaching about 60 $\frac{mW}{m^2}$ for both models. This is provoked by rapid shallow deformation from the lateral compression. However, progressive crustal thickening induced by compression nullifies this effect and surface heat flow rapidly declines. Because the crust is considerably thickened before lithosphere removal and the crust remains thick even after eclogite removal, the final magnitude of surface heat flow is very similar to its initial value. Aside from the peaks generated during root detachment, throughout the evolution of the models there are only low alterations in surface heat flow (below 6 $\frac{mW}{m^2}$), mostly caused by local perturbations at the Moho or at the surface.

Conclusions for model set V are:

- High lateral compression rates (5 mm/yr or higher) produce substantial uplift simultaneously thickening the crust and decreasing the Bouguer gravity anomaly to less than -200 mGal.

- Under high lateral compression rates (5 mm/yr or higher) there are minor alterations to surface heat flow as crust is continually thickened before, during and after lithosphere removal.

- A prominent increase in the Bouguer gravity anomaly and surface heat flow induced by lithosphere removal is only observed at low lateral compression rates (1 mm/yr or lower).

Results from set V suggest that if the current observations at the SNSM were produced by lithosphere removal, the total lateral compression effectively transferred to the massif must have been low, with a compression rate below 5 mm/yr. The models indicate that there is a prominent increase in the gravity anomaly for compression rates up to 1 mm/yr. However, in these models the Bouguer gravity anomaly increase occurs after the collapse of the elevated region. Therefore, there is no simultaneous occurrence of high topography and high Bouguer gravity anomaly. Since compression rates must be low, any contribution to topography from lateral stresses must be small. Therefore, the simultaneous high topography and gravity anomaly can only be explained by lithosphere removal if the crustal root is fully removed and the subsequent mantle dynamics can provide the required support to sustain the load of the massif or to delay its descent.

4.7 Width of Initial Perturbation

The previous models in this chapter use a Gaussian shaped mantle lithosphere perturbation, crustal root, and initial topography, with a half width of 125 km, centred in the modelling domain. This was chosen as an approximation to the width of the SNSM. However, it is important to consider a more representative shape, based on the actual dimensions of the SNSM and its hypothetical mantle lithosphere perturbation. Also, it is important to determine if the width of the perturbation can produce significant changes in the dynamics or the surface expressions of lithosphere removal. Consequently, this section includes modelling set W, which consists of 2 models (model W1 and W2), to test the effect of the perturbation width in the absence of lateral compression. Model W1 has the same setup as model P1, including the perturbation half width of 125 km, but has no lateral compression. Model W2 has the same setup as model W1, but the half width is reduced to 65.2 km.

Firstly, the actual shape of the SNSM topography is examined using data from the ASTER Global Digital Elevation Model V003 (Spacesystems & ASTER Science Team, 2019). The observed topography is compared to the half widths used in the models of set W in figure 4.18. This shows that a perturbation half width of 65.2 km is more representative of the study region. Aside, the initial elevation in the models is also similar to the current elevation of the SNSM.

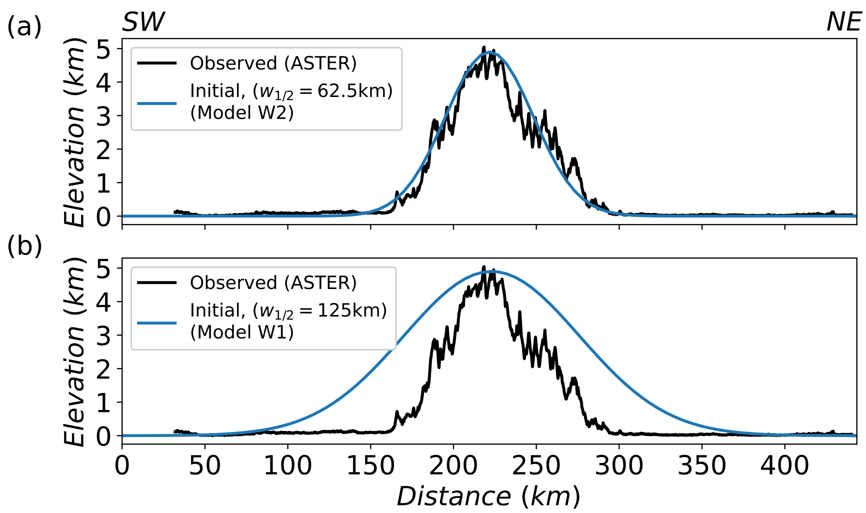

Figure 4.18: Comparison of the modelled initial Gaussian topographies in a) model W2 (half width of 62.5 km), and b) model W1 (half width of 125 km), with the observed topography of the SNSM obtained from the ASTER Global Digital Elevation Model V003, oriented from SW to NE (profile on figure 1.1*a*).

The results of models of set W are shown in figures 4.19, and 4.20. Comparison with results of model P1 (with lateral compression rate of 1 mm/yr) confirms that compression accelerates the removal episode. This is evident in figure 4.20*b*, which shows that model W1 (no lateral compression) presents a later increase in the Bouguer gravity anomaly (7 Ma after than in P1). Also, when the initial perturbation/topography is narrower (model W2), the lithosphere drip occurs 8 Ma after the drip of model W1. This is because the perturbation and crustal root have a lower negative buoyancy because of the decrease in size.

Consequently, the perturbation growth is slower.

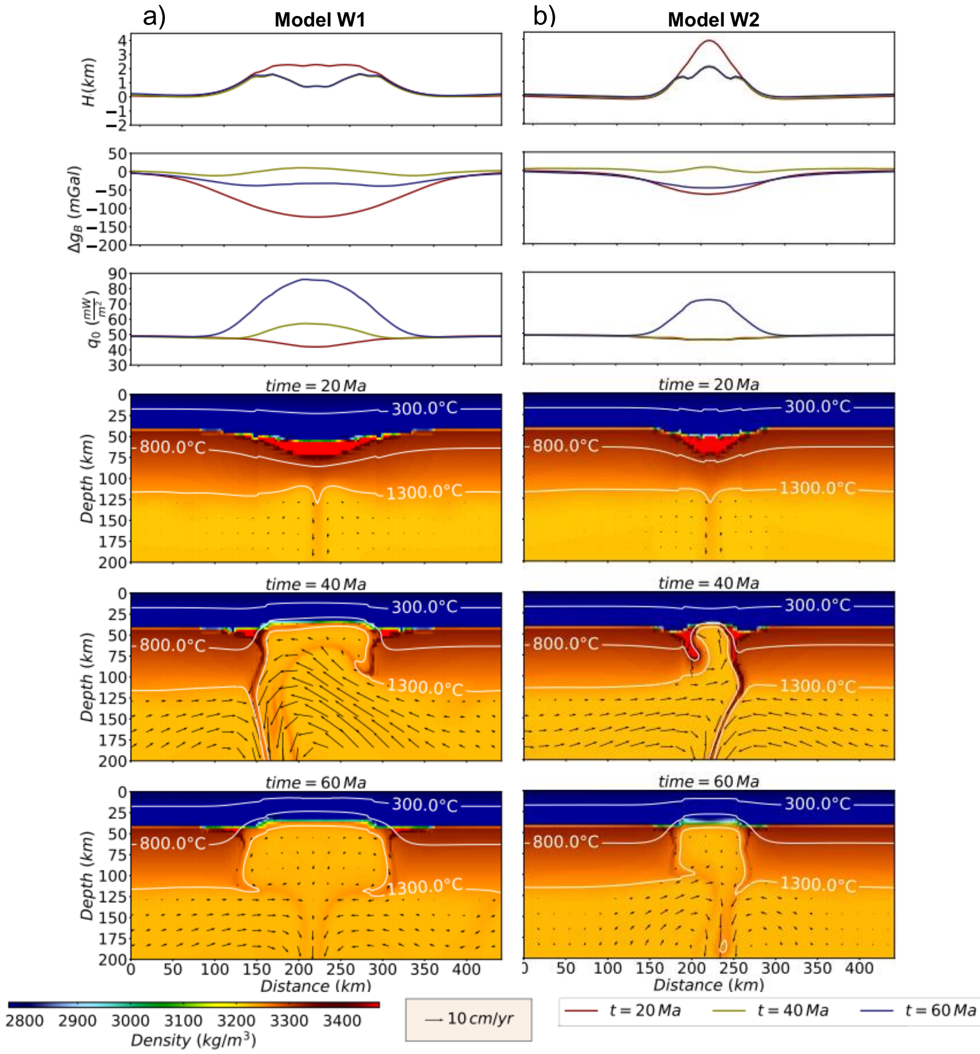

Figure 4.19: Modelling results for (a) model W1 (perturbation half widths of 125 km) and (b) model W2 (perturbation half widths of 62.5 km), including snapshots of density structures and profiles of topography (H), Bouguer gravity anomaly (Δg_B) and surface heat flow (q_0), at times before, during and after the main lithosphere removal episode. Models explore the dynamic effect of the initial lithosphere thickening half width, and its influence on surface-plastic deformation.

Figure 4.20*a* shows that in model W1 there is less subsidence than in model P1 before the removal episode. For instance, there is 1.2 km of less subsidence in the first 30 Ma for model W1, than in the first 27 Ma for model P1. This is because when there is compression, the initial mantle lithosphere perturbation is thickened, resulting in more available negative buoyancy. Then, the thicker instability produces a larger and faster drip. Similarly, when the width of the perturbation is larger (e.g., model W1 compared to model W2), there is also more available negative buoyancy, the drip is larger, and there is more subsidence. As a consequence, there is 0.7 km of less subsidence in model W2 within the first 38 Ma, compared to the subsidence in model W1 in the first 30 Ma. Also, after the drip there is no significant uplift for models of set W, due to the lack of compression. Instead, subsidence is diminished and the topography tends to an equilibrium elevation of 0.6 km for model W1 and 1.3 km for model W2.

For the Bouguer gravity anomaly, model W2 has a higher initial value (-190 mGal compared to -310 mGal for model W1) due to the reduction of the size of the perturbation. In the rest of the evolution, the overall behaviour is the same as in model W1 but the magnitude of the gravity anomaly is reduced because sub-lithospheric mantle upwelling and crustal thinning takes place over a narrower width. For instance, the maximum Bouguer gravity anomaly (right after removal) in model W1 is of 20 mGal whereas in model W2 it is 0 mGal. Since the resultant gap in the lithosphere is wider for model W1, the density perturbation is larger, the corresponding high values in the gravity anomaly profiles cover a wider length (profiles in figure 4.19), and the average anomaly over the perturbed region tends to be higher than for model W2 (e.g., 60 mGal higher at 90 Ma).

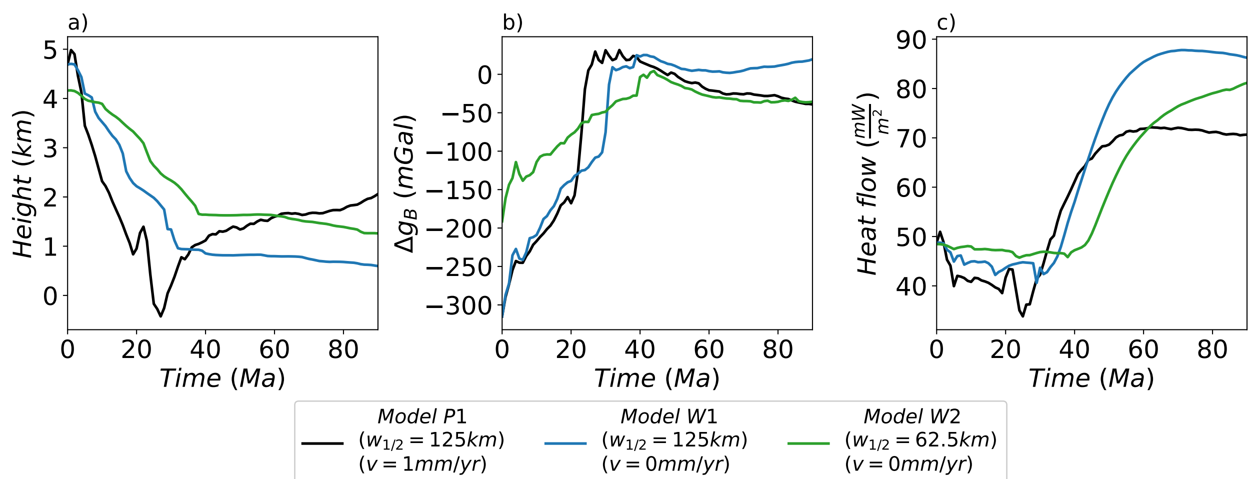

Figure 4.20: Time variation of surface observables for models W1 and W2. Reported values are averaged quantities over a 100 km and 50 km widths for models W1 and W2, respectively, centred in the perturbed region. (a) Topography. (b) Bouguer gravity anomaly. (c) Surface heat flow. Results of model P1 are shown as a reference (black). Time (Ma) corresponds to the modelled time from the beginning to the end of the simulation.

Finally, in models of set W there is no compression, and therefore the crust is not thickened after lithosphere removal. This results in higher surface heat flows after crustal root removal and the ascent of hot sub-lithospheric mantle. In model W1 there is a maximum heat flow of 86 $\frac{mW}{m^2}$ compared to 71 $\frac{mW}{m^2}$ for model P1. For model W2, the lithosphere gap after removal is narrower, and there is less sub-lithospheric mantle reaching the Moho along the profile. This results in a lower magnitude and narrower perturbation in surface heat flow with a maximum value of 80 $\frac{mW}{m^2}$ at 90 Ma.

Results from set W show that the width of the initial perturbation (and topography) has a significant influence on the magnitudes of topography, Bouguer gravity anomaly and surface heat flow. Since a Gaussian topography with half width of 62.5 km is closer to the current topography of the SNSM, the results for model W2 are more representative for the region of study. Hence, the rest of the models in this work use the initial half with of 62.5 km.

The general effects of the width of the initial perturbation/topography are:

- When the initial perturbation/topography is narrower the lithosphere drip is slower because the perturbation (and crustal root) is smaller and has less negative buoyancy.
- When the perturbation is wider, there is more available negative buoyancy, the drip is larger, faster, and there is more subsidence during the drip.

4.8 Discussion and Conclusions

This chapter presents parameter tests to explore the dynamics of lithosphere removal in 2D and its surface expressions. The models include tests of the amount of initial lithosphere thickening, lateral compression rate, plastic deformation, and width of the initial perturbation. This allows an examination of the importance of these parameters, which are difficult to constrain based on observations. The main conclusions obtained from the models in this chapter are:

- If the initial lithosphere thickness in the perturbed region is higher, the final elevation increases, the amount of uplift decreases, and the final surface heat flow is lower. Initial thickness does not have a significant influence in the final magnitude of the Bouguer gravity anomaly, but it affects the speed of the removal with higher rates for a higher initial thickness

- The inclusion of frictional-plastic deformation is critical to create realistic lithosphere deformation. Plasticity has a significant effect on the evolution of topography and surface deformation during a lithosphere removal episode, as it prevents the formation of unrealistically high topographies because it allows the accommodation of deformation through weak zones.

- Parameters related to plasticity (cohesion, friction angle, reference strain for strain weakening) only affect the amount of shallow faulting and small topographic alterations. These do not have a significant effect on the average elevation, Bouguer gravity anomaly, and surface heat flow produced during lithosphere removal.

- If the width of the initial perturbation (and initial topography) is reduced, the size of the instability decreases and there is less available negative buoyancy. This results in a smaller and slower drip which produces less subsidence.

In general, all models show that mantle lithosphere dripping and crustal root eclogitization induce the removal of the crustal root, leading to mantle upwelling, surface uplift, and an increase in both the Bouguer gravity anomaly and surface heat flow. In models that include plastic deformation the magnitudes of the gravity anomaly and elevation right after removal are lower than those observed in the SNSM. However, results demonstrate that lithosphere dripping and crustal root removal (after eclogitization) can lead to the absence (or reduction) of a crustal root, and that the subsequent mantle dynamics can provide support to maintain a surface elevation of more than 1 km, simultaneously producing an increase in surface heat flow.

High magnitudes of lateral compression produce substantial crustal thickening, decreasing the gravity anomaly and surface heat flow. Hence, if lithosphere removal produced the observations in the SNSM, either lateral compression was low (rates close to 1 mm/yr or lower) or there has been not enough time for significant crustal thickening after the event. The simultaneous occurrence of a high topography and a positive Bouguer gravity anomaly induced by lithosphere removal requires that the post-drip mantle dynamics provides sufficient support to hold the load of the massif (or to delay its collapse) until the increase of the gravity anomaly, because the lateral support is probably not significant. For instance, Model W2 results in a maximum gravity anomaly of 0 mGal, with an elevation of about 1.5 km immediately after the removal event. These values show that lithosphere removal can result in an elevated region that is underlain by a thin crust and therefore, an unexpectedly high gravity anomaly. However, these values are still below the magnitudes in the SNSM (maximum height over 5 km and Bouguer gravity anomaly above +130 mGal), suggesting that lithosphere removal is not sufficient to explain the observations in the SNSM, or that there are still important features that have not been considered in the models. For instance, it is known that surface expressions of lithosphere removal (convective instability drips or delamination) have significant variability depending on lithosphere rheology (e.g., Wang and Currie, 2017; Wang et al., 2014). Consequently, it is necessary to conduct more simulations to determine if observations in the SNSM can be explained under other rheological configurations in the modelling setup.

Chapter 5: Lithosphere Removal in the Sierra Nevada de Santa Marta in 2D

5.1 Introduction

Previous studies of lithosphere drips by Wang et al. (2014) and Burov and Watts (2006) show that during and after lithosphere removal, the associated surface expressions can exhibit a broad variation depending on crustal thickness and lithosphere rheology. For instance, Wang et al. (2014) and Wang and Currie (2017) show two end member cases. On one hand, when the crust is thin and strong, the surface response is completely coupled to drip dynamics and a drip event produces surface subsidence. On the other hand, if the crust is thick and the lower or mid-crust is rheologically weak, the surface (upper crust) is mechanically decoupled from mantle dynamics and the induced crustal flows (lower crust) produce crustal contraction, thickening, and uplift. Göğüş and Pysklywec (2008) report that for all drips, the surface topography exhibits a symmetrical trend, and that the removal of lower lithosphere usually leaves a gap that is filled by hot sublithospheric mantle which heats the crust. The latter generally produces a localized and symmetrical increase in surface heat flow. Additionally, studies by Currie et al. (2015), Krystopowicz and Currie (2013) and Leech (2001), show that if lithosphere dripping in a mountain region is driven by, or accompanied by, eclogitization of the lower crust, the drip will remove the eclogitized root, resulting in a thinner crust.

This work investigates if a previous lithosphere removal event may explain the observations in the SNSM. The SNSM is a localized and symmetrical mountain region (with elevations above 5 km) where there is evidence of recent uplift with an unknown driving force (e.g., Villagómez et al., 2011). There is also high surface heat flow (60-80 $\frac{mW}{m^2}$, Quintero et al., 2019) and a high Bouguer gravity anomaly (above +130 mGal, Case and Macdonald, 1973), indicating that there is a thin crust below. Models in Chapter 4 showed that during lithosphere removal with eclogitization, the crustal root can be completely removed. This produces an increase in the Bouguer gravity anomaly while the surface elevation of the perturbed region remains above 1 km. However, it is not clear if these dynamics could produce the values observed in the SNSM or explain a recent uplift episode. The fully viscous models show that mantle upwelling produces significant uplift after the relaxation of downward stresses associated with the drip. On the other hand, models that include plastic deformation show that post-drip uplift is considerably reduced (or even prevented) because upper crustal strength is diminished by plastic yielding, limiting the transfer of vertical stresses originated in the upper mantle.

The purpose in this chapter is to investigate if lithosphere removal can explain the reported magnitudes of topography, gravity anomaly and surface heat flow using 2D numerical models. Lithosphere rheology plays a crucial role in the dynamics of removal and therefore the models here explore variations in rheology. Additional models examine the effects of the local crustal density variations, lateral compression rate and initial thickness of the perturbed region. Additionally, the non-isostatic topography produced by lithosphere removal is reported to quantify to what extent non-isostatic forces can provide support for the load of the massif. Finally, results from the models are used to estimate melting patterns and seismic wave velocities produced in the upper mantle, as other type of evidence that could be used to identify lithosphere removal. The latter could help elucidating whether if this mechanism has played an important role in the history of the extraordinary SNSM.

5.2 Modelling Setup

The reference setup for the 2D models in this chapter is shown in Figure 5.1. The modelling domain, mesh resolution and boundary conditions, are the same as that used in Chapter 4. The upper and lower crust have thicknesses of 20 km each (total crustal thickness of 40 km), and the mantle lithosphere has a thickness of 60 km. This gives a total lithosphere thickness of 100 km, which is consistent with the fact that the SNSM is located close to the boundary of the South American plate rather than in a cratonic area. An initial perturbation is imposed in the centre of the model domain to represent a pre-existing thickened crust and lithosphere. This has a half-width of 62.5 km, comparable to the real half width of the SNSM. The crustal root and mantle lithosphere perturbation is 30 km, and the initial topography is adjusted to produce isostatic compensation with the crustal root.

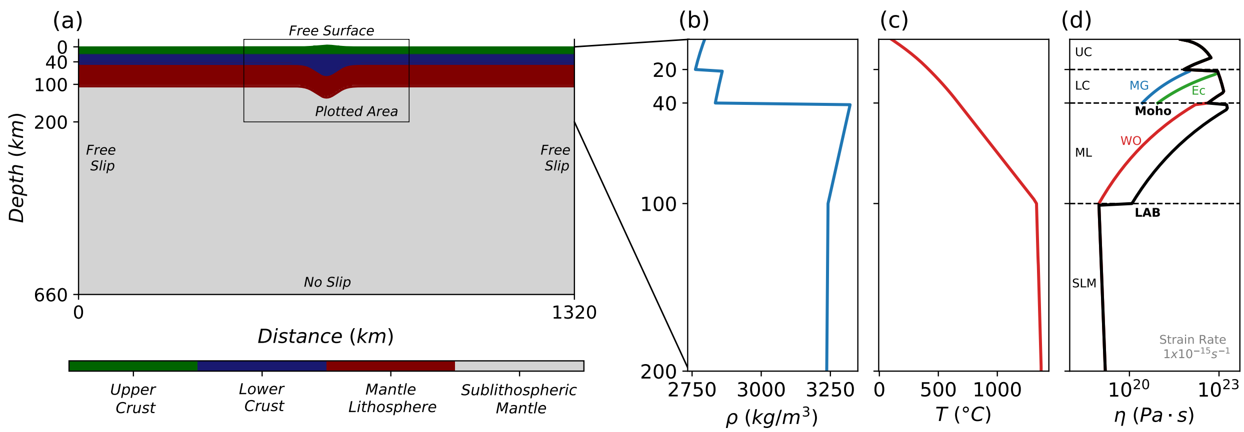

Figure 5.1: (a) Initial model geometry. Only the enclosed region is shown in the following figures. (b) Non-perturbed density structure. (c) Initial temperature conditions. The continental geotherm is stretched in the thickened region keeping the Moho temperature constant. (d) Reference viscosity structure at a constant strain rate of 1×10^{15} s^{-1} (black). Other viscous rheologies tested are also shown. Ec: Eclogite (Zhang & Green, 2007)×0.1, MG: Mafic Granulite (Wang et al., 2012) and WO: Wet Olivine (Karato & Wu, 1993).

The material parameters are also the same as in Chapter 4 except that all materials have viscous-plastic rheologies, and the lower crust and eclogite have the parameter modifications given in table 5.1. In this chapter, the lower crust has a reference density of 2900 kg/m^3 and viscous rheologies of either dry diabase (Mackwell et al., 1998) or mafic granulite (Wang et al., 2012), depending on the model. Also, eclogite has a reference density of 3550 kg/m^3 (e.g., Austrheim, 1987; Austrheim et al., 1997), and a viscous rheology that is 10 times weaker than the rheology of dry eclogite (Zhang & Green, 2007) to represent wet eclogite (abbreviated as Ec×0.1). In the reference model (model A), the upper crust, lower crust, mantle lithosphere and sublithospheric mantle have viscous rheologies of wet quartzite (Gleason & Tullis, 1995) (WQ), dry Maryland diabase (Mackwell et al., 1998) (DMD), dry olivine (DO) and wet olivine (Karato & Wu, 1993) (WO), respectively (table 4.1), using the power law for dislocation creep (equation 2.8). Additionally, all materials have a frictional-plastic rheology using the Drucker

Prager yield criterion (equation 2.9), where strain weakening using plastic strain results in a reduction of the friction angle and cohesion from 15° to 2° and 20 MPa to 2 MPa, respectively. The formulation used for viscoplastic rheologies is introduced and explained in section 2.3.2.

Table 5.1: Additional material parameters for models in this chapter. The upper crust, mantle lithosphere and sub lithosphere mantle use parameters given in Table 4.1.

Parameter	**Lower Crust**		**Eclogite**
$\rho_0\,(kg/m^3)$	2900		3550
$\alpha\,(1/K)$	3×10^5		3×10^5
Plastic rheology[a]			
ϕ	$15° - 2°$		$15° - 2°$
$C\,(MPa)$	$20 - 2$		$20 - 2$
Viscous rheology	*Dry Diabase*	*Mafic Granulite*	*Dry Eclogite*$\times 0.1$
$A_{ps}\,(Pa^{-n}s^{-1})$ [b]	5.78×10^{-27}	3.17×10^{-21}	3.74×10^{-14}
n	4.7	3.2	3.5
$E\,(kJ/mol)$	485	244	403
$V\,(m^3/mol)$	0	0	2.72×10^{-5}
Thermal Parameters			
$k\,(Wm^{-1}K^{-1})$	2.25		2.25
$C_p\,(Jkg^{-1}K^{-1})$	1250		1250
$H\,(W/kg)$	1.38×10^{-10}		1.13×10^{-10}

[a] All the materials have viscous-plastic rheologies, in which strain weakening is applied when plastic strain changes from 0.5 to 1.5, by changing the friction angle and cohesion from 15-2° and 20-2 MPa, respectively.
[b] The experimental uni axial strain viscosity pre-factor A_{uni} is scaled to plane strain A_{ps} using a scaling factor of $3^{\frac{n+1}{2}}2^{-1}$.

Table 5.2: List of models with parameter modifications with respect to the reference model. The mantle lithosphere rheology is varied locally (in the central region), but remains as dry olivine at the sides for all models. Ec=eclogite, DMD=dry Maryland diabase, WO=wet olivine, DO=dry olivine, MG=mafic granulite, and LMG=local mafic granulite (MG in the perturbed region only and DMD in the rest).

Model	Eclogitization	Eclogite Rheology	Lower Crust Rheology	Local Mantle Lithosphere Rheology	ρ_0^* [a] (kg/m^3)	Figure No.
Reference						
A	✗	Ec×0.1	DMD	DO	2800	5.2
Set B						
B1	✓	Ec×0.1	DMD	DO	2800	5.4*a*
B2	✓	Ec×0.1	LMG	DO	2800	5.4*b*
B3	✓	Ec×0.1	MG	DO	2800	5.4*c*
Set C						
C1	✓	Ec×0.1	DMD	WO	2800	5.5*a*
C2	✓	Ec×0.1	LMG	WO	2800	5.5*b*
C3	✓	Ec×0.1	MG	WO	2800	5.5*c*
Set D						
D1	✓	MG	LMG	WO	2800	5.9*a*
D2	✓	Ec	LMG	WO	2800	5.9*c*
Set E						
E1	✓	Ec×0.1	DMD	WO	2900	5.11*a*
E2	✓	Ec×0.1	LMG	WO	2900	5.11*b*
E3	✓	Ec×0.1	MG	WO	2900	5.11*c*

[a] ρ_0^* stands for the reference density in the upper crust locally, over the width of the perturbed region only.

The reference model for this chapter does not include lower crustal eclogitization. However, in subsequent models there is eclogitization of the lower crust at a temperature of $680°C$, and a pressure of 1.2 GPa. Tables 5.2 and 5.3 summarize the models presented in this chapter, showing the parameter modifications with respect to the reference.

5.3 Results

5.3.1 Reference Model (Model A)

Model A is the reference model for this chapter. It uses the setup in Figure 5.1*a*, including the reference viscosity structure in Figure 5.1*d* (black line), and the results are shown in Figure 5.2. The initial crustal thickening results in a perturbation of the lithosphere-asthenosphere boundary (LAB). The mantle lithosphere is gravitationally unstable because it is cooler

Table 5.3: List of models of set F with parameter modifications with respect to model E2 which is taken as the reference for this set.

Model	Lateral Compression Rate (mm/yr)	Initial Amplitude of crustal root* (km)	Figure No.
Reference			
E2	0.0	30	5.11*b*
Set F			
F1	0.0	20	Appx. B1*a*
F2	0.0	40	Appx. B1*c*
F3	0.5	20	Appx. B2*a*
F4	0.5	30	Appx. B2*b*
F5	0.5	40	Appx. B2*c*
F6	1.0	20	Appx. B3*a*
F7	1.0	30	Appx. B3*b*
F8	1.0	40	Appx. B3*c*
F9	1.5	20	Appx. B4*a*
F10	1.5	30	Appx. B4*b*
F11	1.5	40	Appx. B4*c*

and therefore denser than the sublithospheric mantle. The imposed perturbation triggers lithospheric dripping in a similar fashion to the models of Houseman et al. (1981). The crustal root is initially pulled down during the growth of the perturbation, producing a thickening of the crust and a progressive decrease in the gravity anomaly to -185 mGal. After the perturbation founders and detaches, there is a rapid gravity anomaly increase of ~30 mGal producing a spike at $t = 40$ Ma (Figure 5.3*b*). However, the immediate replacement of dense mantle lithosphere by hot and buoyant sublithospheric mantle causes a further decrease in the gravity anomaly and by 100 Ma, the Bouguer gravity is -193 mGal. Throughout the model evolution, there are minor topographic alterations (<0.12 km) related to the drip, and a gentle increase in surface heat flow of 8 $\frac{mW}{m^2}$ as the hot sublithospheric mantle comes into contact with the crustal root.

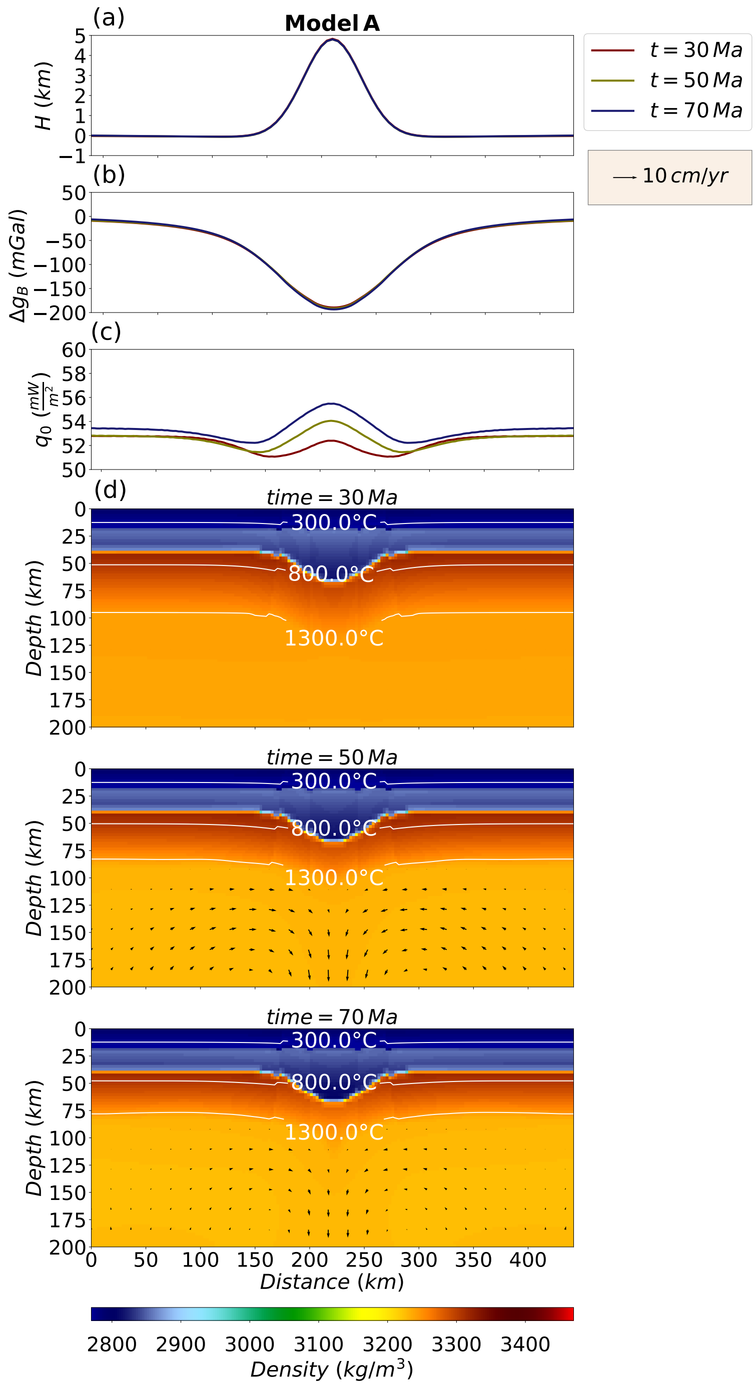

Figure 5.2: Evolution of the reference model (Model A) at different times, showing the effect of the mantle lithosphere drip. (a) Topographic profiles, where the elevation (H) is reported relative to the unperturbed surface of the modelling domain. (b) Bouguer gravity anomaly profiles (Δg_B). (c) Surface heat flow profiles (q_0). (d) Snapshots of the density and thermal structure.

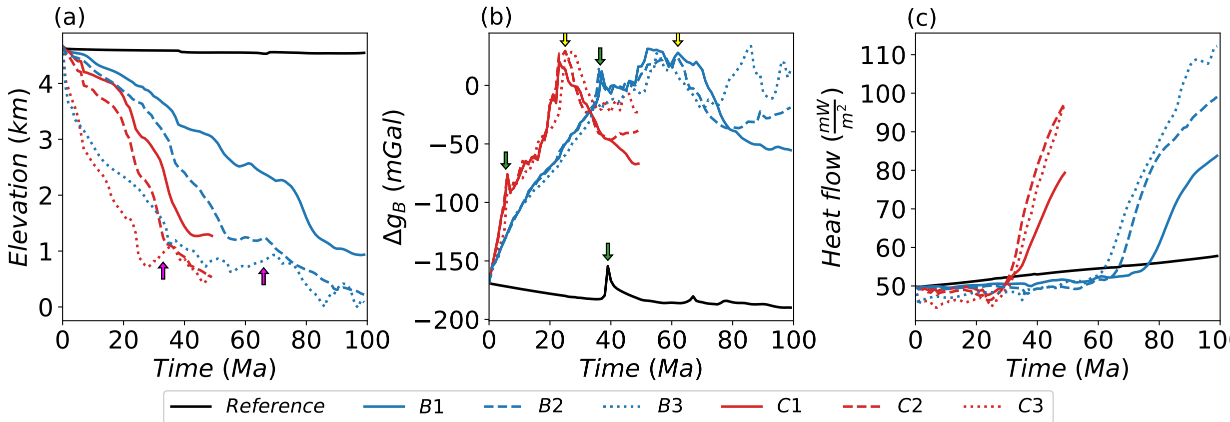

Figure 5.3: Time variation of surface observables averaged over a 50 km width centred over the initial perturbation, for the reference model (black) and sets B (blue) and C (red). (a) Surface. Lithosphere removal induces instantaneous subsidence. Pink arrows indicate stages of significant uplift after removal in models B3 and C3. (b) Bouguer gravity anomaly (Δg_B). Lithosphere removal produces an immediate increase in Δg_B. Green arrows indicate the gravity response to the mantle lithosphere drip and yellow arrows indicate the response produced by crustal root removal. (c) Surface heat flow. Surface heat flow increases rapidly after the removal episode as the heat must transfer through the crust by conduction. Time (Ma) corresponds to the modelled time from the beginning to the end of the simulation.

5.3.2 Effect of Lower Crustal Eclogitization (Model B1)

Model B1 follows the parameters of Model A, but it includes eclogitization of the lower crust, following the procedure used in Chapter 4. If the lower crustal material reaches the conditions for eclogitization (i.e., temperature of 680°C, and pressure of 1.2 GPa), its density increases to 3550 kg/m^3, representing full eclogitization of a basaltic lower crust (e.g., Austrheim et al., 1997). The lower crust is not initially in the eclogite stability field and rather, the phase change conditions are induced by the pull of the foundering mantle lithosphere and the temperature increase during lithosphere removal. The negative buoyancy of the mantle lithosphere and eclogite produce significant surface subsidence, as well as an increase in the Bouguer gravity anomaly. The mantle lithosphere under the perturbed region starts dripping while the lower crust undergoes eclogitization. The continued phase change of the crustal root leads to the onset of crustal root removal at about 55 Ma (i.e., when the root starts to drip), and to its complete detachment at 71 Ma. In the period between 55-70 Ma, the crustal root drips together with the remaining mantle lithosphere underneath. This leaves a thin crust (38 km) in the centre of the model, underlain by upwelling sublithospheric mantle.

The mantle lithosphere drip produces progressive surface subsidence and a rapid peak in the Bouguer gravity anomaly at about 40 Ma (Figure 5.3*b*), (similarly as in model A). Crustal root eclogitization prior to its removal produces an increase in the Bouguer gravity anomaly reaching a maximum peak of +28 mGal at about 51 Ma. Then, crustal root removal produces an increase in the Bouguer gravity anomaly (reaching a peak of +22 mGal), and an increase in subsidence rate (up to 0.2 mm/yr) at t=61 Ma (Figure 5.3).

After root detachment, the Bouguer gravity anomaly is the net result of a thin crust (∼38 km), which produces a positive contribution, and the presence of shallow low-density sublithospheric mantle (replacing the mantle lithosphere), which produces a negative contribution. The latter results in a positive anomaly right after full eclogite detachment (e.g., 71 Ma).

In the next period (70-100 Ma), upwelling of sublithospheric mantle to shallow levels induces a progressive increase in surface heat flow (up to $84.3\frac{mW}{m^2}$). The localized heating of the lower crust decreases its density preferentially, producing a local decrease in the gravity anomaly. Further, as the initial topography sinks, the interface between the upper crust and the lower crust bends downward to accommodate the descending lighter material (maximum bending of ∼8 km at 100 Ma), also decreasing the Bouguer gravity anomaly. The latter results in a local Bouguer gravity anomaly and surface elevation of -50 mGal and 1 km, respectively, at 100 Ma.

This model shows that the drip event results in a period of high (and positive) gravity anomaly coexisting with a topographic high during (and right after) crustal root removal (Figure 5.3*a* between 46 and 72 Ma). This trend is observed in the rest of the models in this chapter but the timescales and magnitudes vary with different rheologies and/or density parameters.

5.3.3 Lower Crustal Rheology (Set B)

Lithospheric rheology is known to produce significant differences in drip dynamics (e.g., Göğüş and Pysklywec, 2008; Wang and Currie, 2017; Wang et al., 2014). Therefore, model tests are carried out to examine different rheological parameters. In model set B (Figure 5.4) the lower crustal rheology is varied. Figure 5.1*d* shows viscosity profiles for all the rheologies used in the models. The lower crust in Model B1 has a rheology of DMD, as in the reference (model A). Model B2 uses the lower crustal rheology of a mafic granulite (MG, Wang et al., 2012) in the thickened region; the crust on either side has a DMD rheology. Hereafter, this structure is referred to as local mafic granulite (LMG), and it represents a locally weaker composition, hypothesized to be the result of hydration of the thickened region by water injection in the previous magmatic arc. In model B3, all the lower crust has an MG rheology, producing a weak lower crust for the entire model that mechanically decouples the upper crust and the mantle lithosphere. The results of set B are shown in figures 5.3 and 5.4.

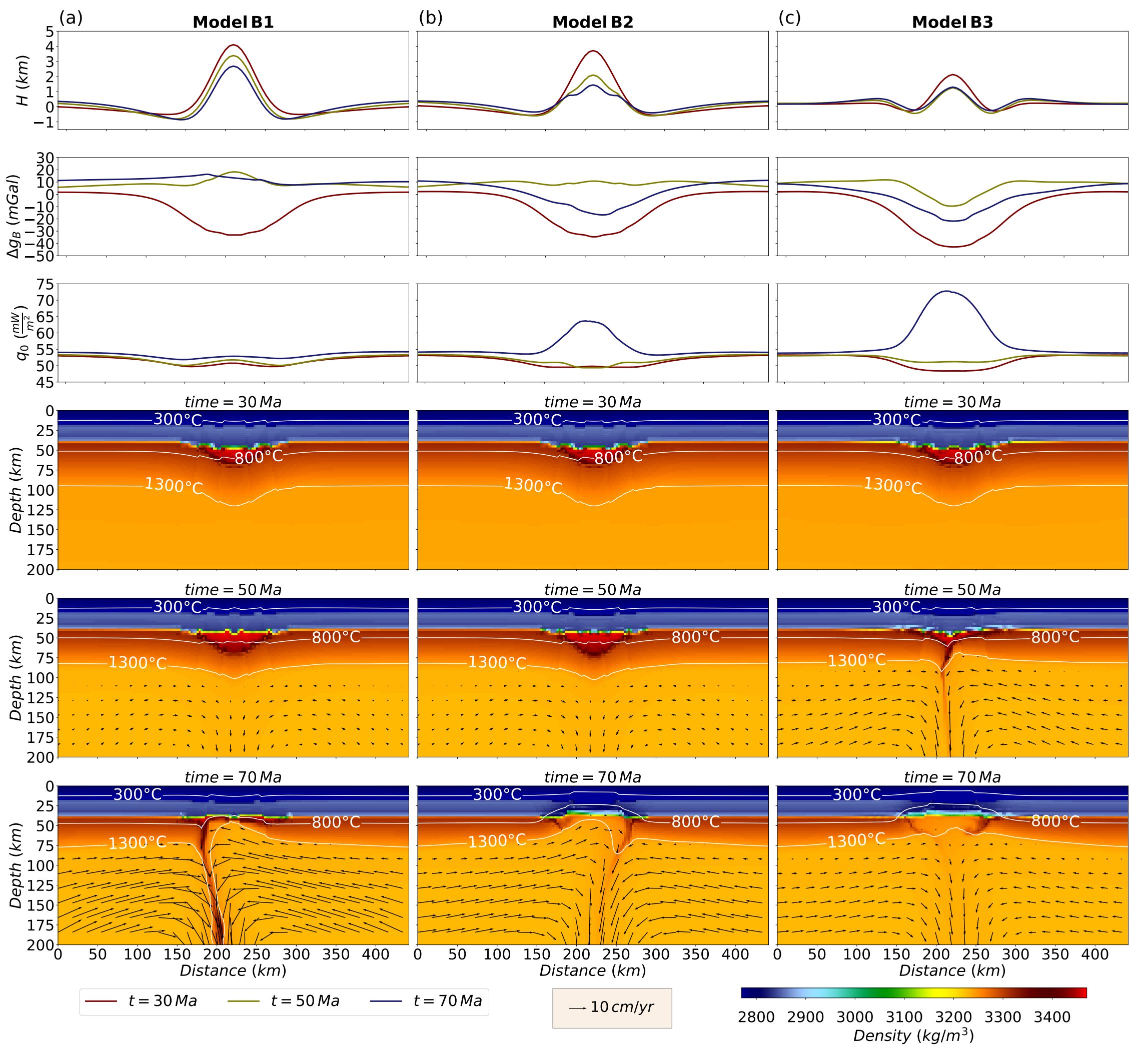

Figure 5.4: Evolution of (a) model B1, (b) model B2 and (c) model B3, including snapshots of density structures and profiles of topography (H), Bouguer gravity anomaly (Δg_B) and surface heat flow (q_0), at times before, during and after the main lithosphere removal episode. Modelling set B includes eclogitization and explores the effect of different lower crustal rheologies.

A rheologically weaker lower crust (i.e., LMG or MG) allows for a slight increase in the removal rate. For models B2 and B3, detachment occurs at 64 Ma and 60 Ma, respectively, which is 6 Ma and 10 Ma earlier than in model B1 (71 Ma). In models B2 and B3, elevations are consistently lower than in model B1, suggesting less support for the initial topography owing to the weaker crust. On the other hand, model B3 exhibits ∼0.3 km of uplift after lithosphere removal. In this case, the faster crustal root removal results in a more rapid ascent of the sublithospheric mantle compared to model B1. This upwelling appears to drive the post-removal uplift.

After crustal root detachment (at 71, 64, and 60 Ma for models B1, B2, and B3, respectively), topographic collapse and lower crustal heating result in a decrease in the Bouguer gravity anomaly similarly as in model B1, due to a downward deflection of the upper-lower crustal interface (∼8 km), and the thermal effect on density. However, at later times (e.g., 80 Ma for model B2), there is crustal thinning of up to 6 km induced by the upwelling of sublithospheric mantle in models with weak lower crustal rheologies (i.e., B2 and B3). This crustal thinning is progressive and results in a higher Bouguer gravity anomaly and surface heat flow. For example, in Figure 5.3*b* the Bouguer gravity anomaly in model B2 increases significantly with respect to model B1 after 80 Ma, resulting in a final value of -25 mGal (about 25 mGal higher than in model B1). Also, Figure 5.3*c*, shows that the final surface heat flow in model B2 is 15 $\frac{mW}{m^2}$ higher than in model B1. This is attributed to the combined effect of crustal thinning (due to sublithospheric mantle upwelling), and the larger heating time in model B2 (crustal root removal occurs sooner). Effects of crustal thinning in model B3 are not compared because the late dynamics of this model is influenced by lithospheric delamination (see details in section 5.3.6).

5.3.4 Mantle Lithosphere Rheology (Set C)

In model set C variations in mantle lithosphere rheology are tested. Model A and models in set B (models B1, B2 and B3) use a mantle lithosphere rheology of dry olivine. In set C, the mantle lithosphere in the perturbed region has the rheology of wet olivine, considering that the SNSM was an active continental arc and therefore may have been more hydrated than adjacent regions. Models C1, C2 and C3 have the same modifications in the lower crust as models B1, B2 and B3, respectively. These models also include lower crustal eclogitization and consequently, lithosphere removal is produced by both the perturbation in the mantle lithosphere and the formation of dense eclogite. The results for model set C are shown in figures 5.3 and 5.5.

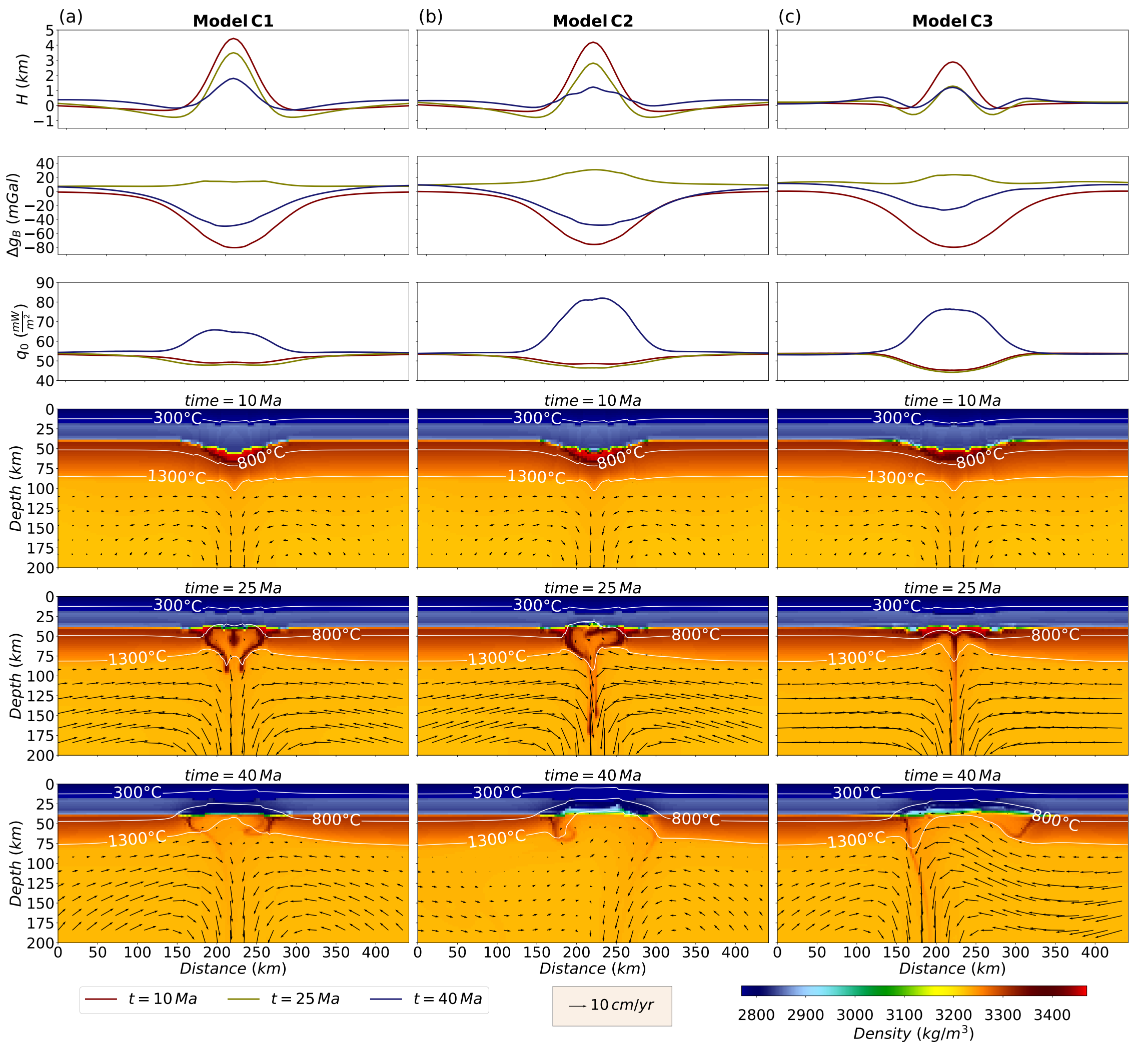

Figure 5.5: Evolution of (a) model C1, (b) model C2 and (c) model C3, including snapshots of density structures and profiles of topography (H), Bouguer gravity anomaly (Δg_B) and surface heat flow (q_0), at times before, during and after the main lithosphere removal episode. Modelling set C has a wet (weaker) mantle lithosphere rheology below the elevated region. Models in the set include eclogitization, and explore the effect of different lower crustal rheologies.

The effects of mantle lithosphere rheology are evident in the differences between observables in sets B and C (Figure 5.3). The general behaviour in set C resembles that of set B, but the presence of weaker mantle lithosphere in the central region (in set C) speeds up the removal process. Root detachment occurs at 25, 26 and 28 Ma for C1, C2, and C3 respectively, which is ~35-42 Ma earlier than in the comparable set B models. This results in an earlier increase in surface heat flow and Bouguer gravity anomaly, as well as an earlier increase in subsidence rate (Figure 5.3) (alterations in observables occur 30-40 Ma earlier). In set B, the mantle lithosphere has a dry and strong rheology, which results in a slower drip, and thus the crustal root can completely turn into eclogite before its detachment because the mantle lithosphere inhibits its descent. Therefore, the positive gravity anomaly remains for longer (e.g., it lasts about 26 Ma in model B1) since it is first produced by the full eclogite root, and then it is maintained by crustal thinning after detachment. In these cases, root removal produces a small drop in the gravity anomaly (e.g., at t=59 Ma in model B1 (Figure 5.3*b*)) which is immediately recovered. On the other hand, in set C, the mantle lithosphere has a weaker rheology, and the high-density eclogite starts dripping right after its formation, producing a rapid main peak in the gravity anomaly (see models of set C at about t=25 Ma, in Figure 5.3*b*).

Models with a weak lower crust (C2 and C3) in set C also exhibit crustal thinning (~6 km) induced by sublithospheric mantle upwelling. This produces an increase in the Bouger gravity anomaly and surface heat flow at late times (>40 Ma) in a similar way as in models of set B (e.g., increase of 25 mGal and 15 $\frac{mW}{m^2}$ in model C2 relative to model C1). Such as in model B3, the effects of crustal thinning in model C3 are not compared because the late dynamics of this model is influenced by lithospheric delamination (see details in section 5.3.6).

5.3.5 Comparison of Surface Observables

The effect of lithosphere rheology on surface observables is summarized in Figure 5.6. This figure compares the surface elevation, Bouguer gravity anomaly, and surface heat flow in the central part of the model at the time of the maximum gravity anomaly ($t = t_{\Delta g_{max}}$), and at 10 Ma after this ($t = t_{\Delta g_{max}} + 10$ Ma). The time of the maximum gravity anomaly is chosen because the purpose of this study is to find to what extent an episode of lithosphere removal (including crustal root removal) can produce an increase in the Bouguer gravity anomaly, and the implications of the latter in the other observables (surface elevation and heat flow).

The time of the maximum gravity anomaly is taken as an indicator of the time of crustal root removal because it occurs when most of the crustal root has dripped and immediately before the detachment of the last remains of eclogitized lower crust (∼1-3 Ma before depending on the model).

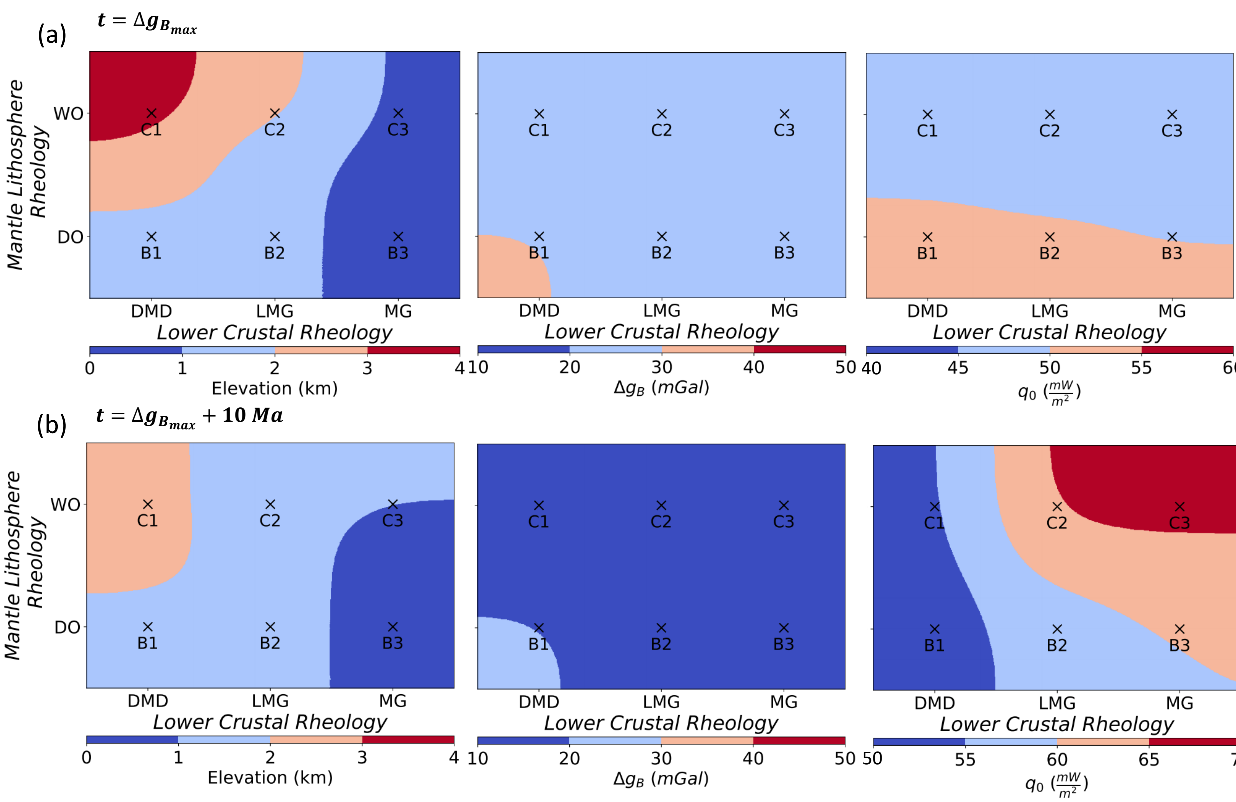

Figure 5.6: Magnitude of surface elevation, Bouguer gravity anomaly (Δg_B), and surface heat flow (q_0) (from left to right), averaged over a 50 km width centred on the perturbed region, (a) at the time of the maximum gravity anomaly after crustal root removal, and (b) 10 Ma after the peak gravity anomaly. The plots shown models of sets B and C as a function of mantle lithosphere rheology (y-axis) and lower crustal rheology (x-axis). This summarizes the general effect of lithosphere rheology on the surface expressions of lithosphere removal.

The maximum gravity anomaly for all the models is within 20-30 mGal, suggesting that there is not a significant difference between the models. However, a weaker mantle lithosphere rheology results in elevations within the range of 3 to 4 km, which are high compared to the elevations for strong mantle lithosphere rheologies (within 0 to 2 km), because the removal is faster than the subsidence rate. Conversely, weaker lower-crustal rheologies allow a faster subsidence rate resulting in lower elevations (within 1-2 km) compared to elevations for strong lower-crustal rheologies (within 3-4 km). 10 Ma after the removal episode the relative variations between the models are the same, but the magnitudes of gravity anomaly and height are lower for all models (decrease of about 1 km and 10 mGal in Figure 5.6*b*).

On the other hand, surface heat flow exhibits different trends during and after root removal. For instance, at $t = t_{\Delta g_{max}}$, variations in lower crustal rheology do not affect the surface heat flow, but surface heat flow is lower (between 45-50 $\frac{mW}{m^2}$) for a weaker mantle lithosphere because in this case the drip is faster (occurs at about 25 Ma) and there is less internal crustal heating time before crustal root removal. Conversely, when the mantle lithosphere rheology is strong, eclogite removal occurs later (e.g., 70 Ma for model B1), resulting in slightly higher values of surface heat flow (between 50-55 $\frac{mW}{m^2}$). At 10 Ma after $t_{\Delta g_{max}}$, the crust has started to be heated by the presence of the hot sublithospheric mantle. Surface heat flow is higher (up to 60-70 $\frac{mW}{m^2}$) with weaker lithosphere rheologies (both in the lower crust and mantle lithosphere) because they enhance mantle lithosphere removal (more amount is removed in less time), and allow for some crustal thinning by upwelling of sub lithospheric mantle after the complete removal.

5.3.6 Late Evolution

The main purpose of the models is to explore the surface expressions during the lithosphere removal episode (i.e., within 10 Ma before and 10 Ma after the drip). However, the models also make predictions over longer timescales. Figure 5.7 shows the surface observables between 50 Ma to 75 Ma for the models in set C, and between 75 Ma to 100 Ma for the models in set B. The behaviour observed in both sets is consistent and only differs in timing. In general, the evolution of set B is delayed because of the higher mantle lithosphere viscosities.

In models B1 and C1, topography continues to decrease after the removal event, reaching elevations of 1 km and 0.8 km, respectively. The Bouguer gravity anomaly for model B1 keeps decreasing, converging to a nearly constant value around -65 mGal at about 90 Ma. In model C1 there is little change in the gravity anomaly, which has a value of about -60 mGal. For both B1 and C1, surface heat flow increases over time, as the lower crust remains exposed to the hot sublithosphere mantle, and the high temperatures heat the crust by conduction. Models B1 and C1 reach values of 80 $\frac{mW}{m^2}$ and 93 $\frac{mW}{m^2}$, at 100 Ma and 75 Ma, respectively.

Surface heat flow in model C1 is higher because there has been more heating time after crustal root detachment (~50 Ma) than for model B1 (~30 Ma).

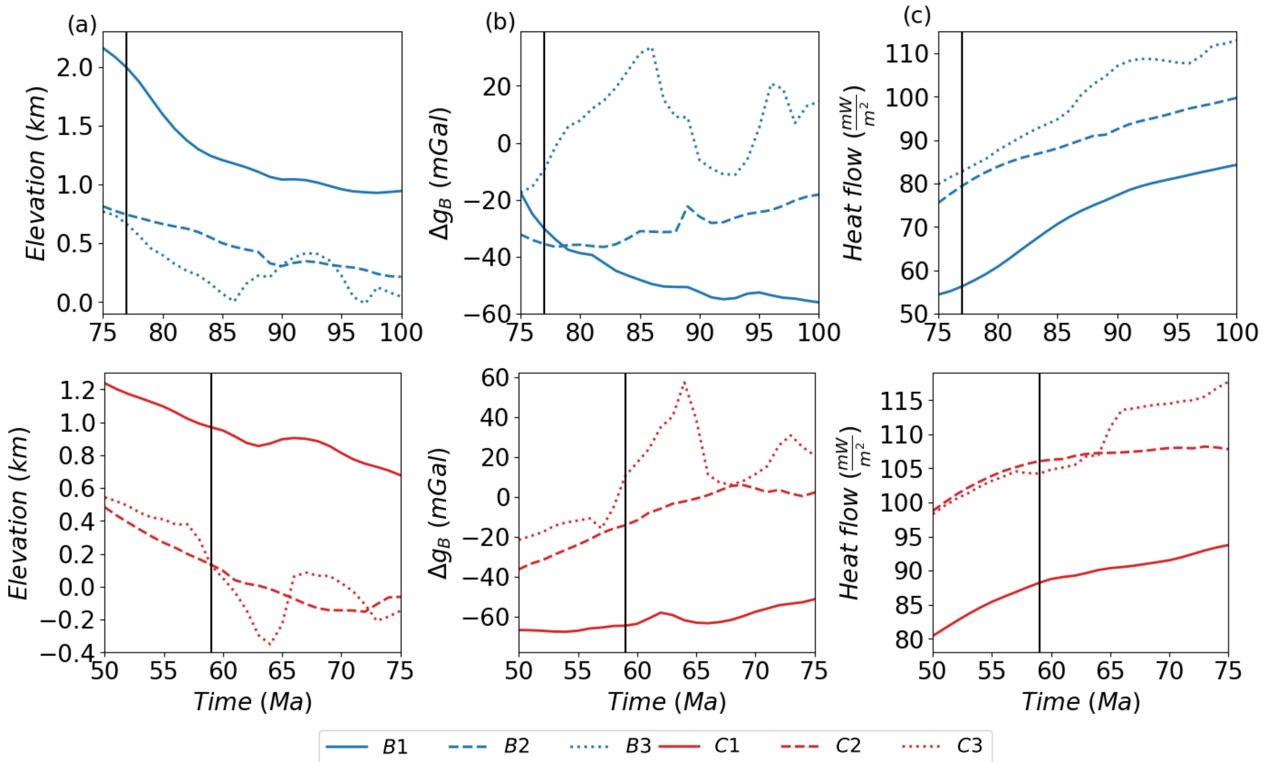

Figure 5.7: Late evolution of surface observables averaged over a 50 km width centred in the perturbed region, for models of sets B and C. (a) Surface elevation. (b) Bouguer gravity anomaly (Δg_B). (c) Surface heat flow. The time on the x-axis has been chosen to show the surface expressions produced by delamination in models B3 and C3. The black vertical line in each plot shows the time at which delamination starts for models B3 and C3.

Models B2 and C2 have a weaker lower crustal rheology in the central region, and therefore elevations are consistently lower because there is less support and subsidence occurs faster (elevations in model B2 and C2 are 0.75 km and 0.9 km lower than in models B1 and C1, respectively). Also, the presence of a weaker lower crust allows for significant crustal thinning (~6 km) induced by progressive sublithospheric mantle upwelling after the removal. This results in a higher Bouguer gravity anomaly for models B2 and C2; B2 has an anomaly that is 38 mGal higher than that of B1, and C2 is about 50 mGal higher than C1. The thinner crust in B2 and C2 also results in an increase in surface heat flow of 15 $\frac{mW}{m^2}$ relative to models B1 and C1.

Interestingly, the behaviour is completely different for models B3 and C3, which have a weaker lower crust all along the profile. In this case, there is less coupling between the lower crust and the mantle lithosphere and the detachment of the crustal root and mantle lithosphere is promoted. The sublithospheric mantle upwells in the central region, and the mantle lithosphere at one side begins to peel away as a coherent block, sinking into the sublithospheric mantle (Figure 5.8). This process is driven by the cool and thus dense mantle lithosphere, which is dense enough to detach from the weak lower crust . As described by Göğüş and Pysklywec (2008), this type of behaviour is known as lithospheric delamination, and it is characterized by asymmetrical surface expressions in topography and surface heat flow. This occurs in both B3 and C3, starting at 77 Ma and 59 Ma, respectively, and it leads to a wide region of thin lithosphere, in contrast with other models where thinning was restricted to the central region. Delamination induces a brief uplift pulse with rates of 0.06 mm/yr and 0.37 mm/yr (at 86 Ma and 64 Ma), for B3 and C3, respectively (Figure 5.7a). This is accompanied by further crustal thinning (9 km), leading to an increase in the Bouguer gravity anomaly with maximum peaks of +35 mGal and +59 mGal, for B3 and C3, respectively (also at 86 Ma and 64 Ma). Delamination is also followed by a rapid increase in surface heat flow of $10\frac{mW}{m^2}$ and $6\frac{mW}{m^2}$, for B3 and C3, respectively (starting at 86 Ma and 64 Ma).

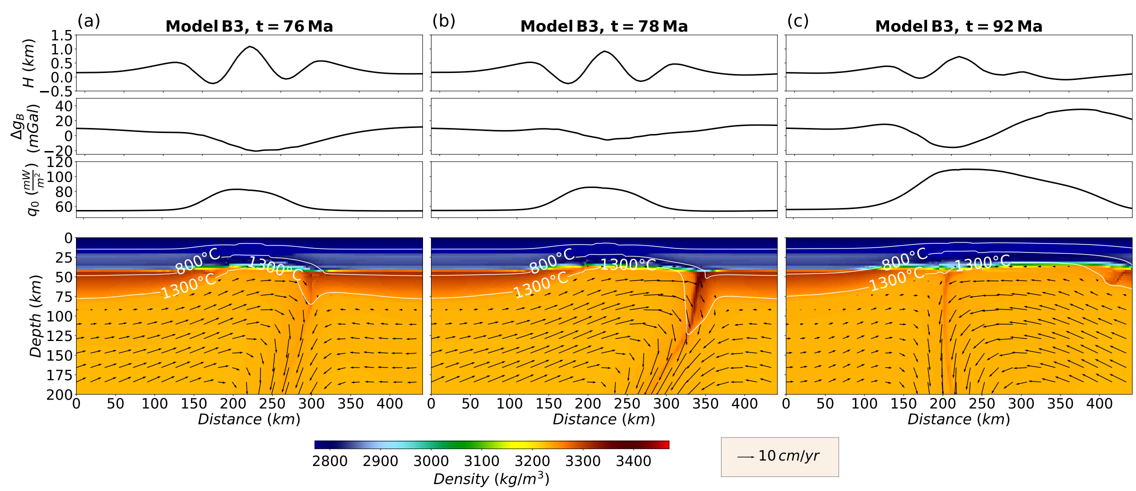

Figure 5.8: Snapshots of the density structure and profiles of surface observables for the late evolution of model B3 showing mantle lithosphere delamination: a) at 76 Ma, before the onset of delamination. b) at 78 Ma showing active delamination. c) at 92 Ma, after delamination showing the resultant non-symmetrical surface expressions of topography (H), Bouguer gravity anomaly (Δg_B), and surface heat flow (q_0).

5.3.7 Eclogite Rheology (Set D)

The previous models use the eclogite rheology from Zhang and Green (2007), with the viscosity reduced by one order of magnitude to represent rheological weakening produced during the phase change (i.e., Ec×0.1 in table 5.2). However, there is little constraint on the actual strength of eclogitized lower crust. Some studies report that eclogitization is accompanied by rheological weakening, suggesting that eclogites could be weaker than their protoliths and that the overall strength of eclogites is conditioned by the extent and rate of the reaction, which is strongly dependent on the amount of water available to trigger the phase change or the mechanisms by which water enters the rock (e.g., Austrheim et al., 1997; Leech, 2001) However, other studies suggest that eclogite may have a strong rheology (e.g., Jin et al., 2001).

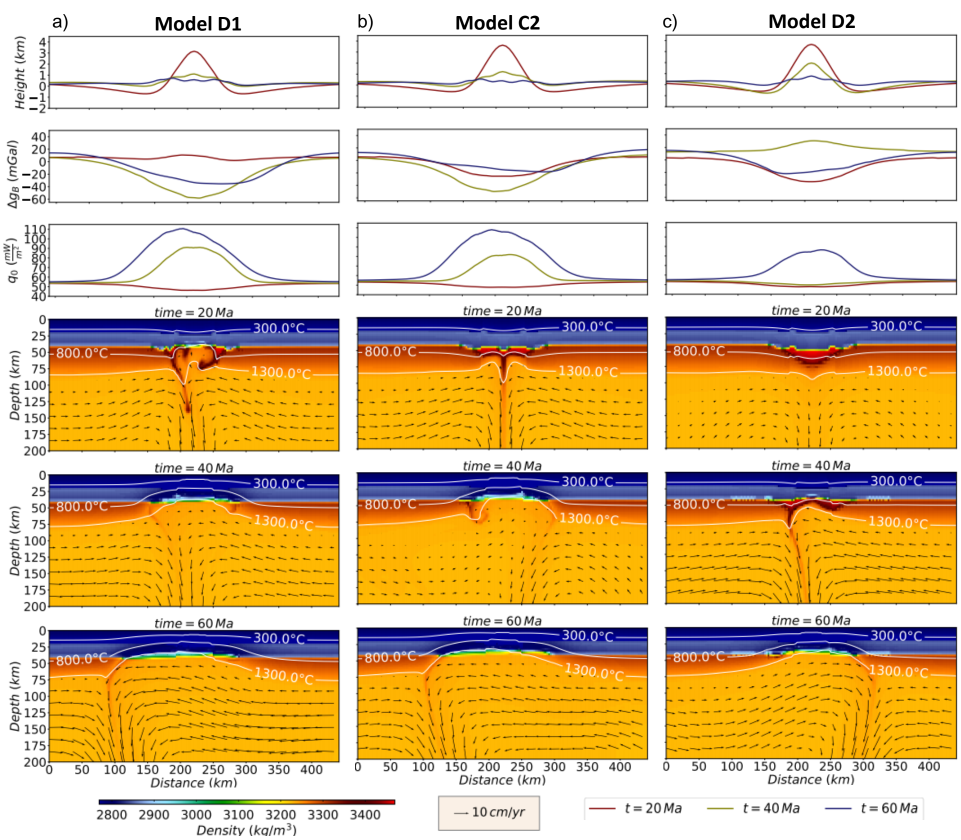

Figure 5.9: Evolution of set D, which explores the effect of different eclogite rheologies. (a) model D1 (Wang et al., 2012), (b) model C2 as a reference (Zhang & Green, 2007)×0.1 (c) model D2 (Zhang & Green, 2007). Plots include snapshots of density structures and profiles of elevation (H), Bouguer gravity anomaly (Δg_B) and surface heat flow (q_0), at times before, during and after the main lithosphere removal episode.

Model set D (consisting of models D1 and D2) examines how changes in eclogite rheology affect the dynamics of a lithosphere drip. Models D1 and D2 have the same setup as model C2, with the only difference being the eclogite rheology. In model, E1 eclogite is modelled using the rheology of mafic granulite from Wang et al. (2012) (MG), and in model D2, it has the rheology of dry eclogite from Zhang and Green (2007) (Ec). The results of these models are shown in Figures 5.9, and 5.10, including the results of model C2 for comparison because it uses the standard rheology of Ec×0.1.

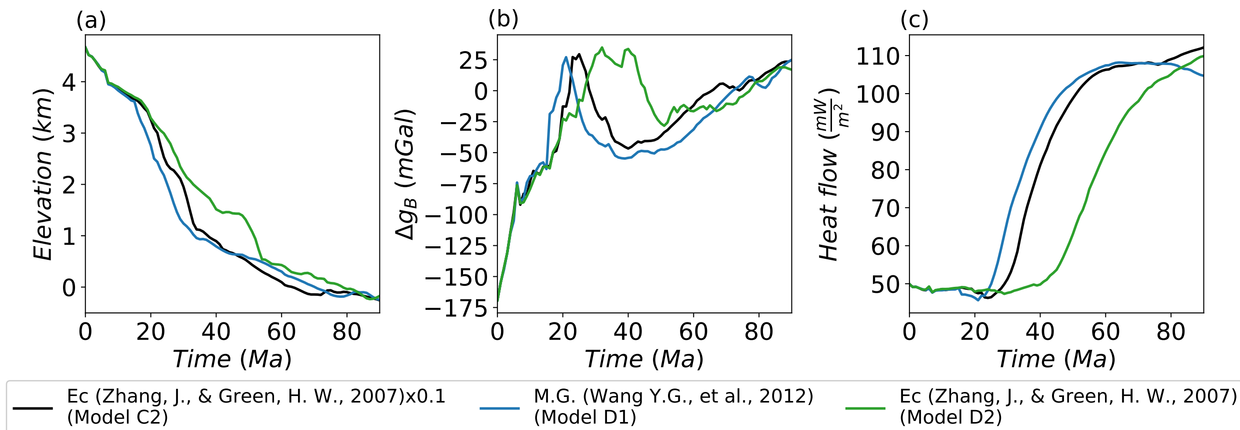

Figure 5.10: Time variation of surface observables averaged over a 50 km width centred in the perturbed region, testing the effect of different eclogite rheologies. Results of model C2 are shown as a reference (black). (a) Surface elevation. (b) Bouguer gravity anomaly (Δg_B). (c) Surface heat flow. Time (Ma) corresponds to the modelled time from the beginning to the end of the simulation.

The model evolution and the associated surface expressions (Figure 5.10) show that eclogite rheology does not have a significant effect on the overall dynamics or the trends and magnitudes of surface topography, Bouguer gravity anomaly, and surface heat flow. The most important effect is the timing of crustal root removal. Model D1, which has the weaker eclogite rheology has a slightly faster drip (detachment occurs 4 Ma before than model C2), whereas model D2, which has the strongest rheology, has a considerably slower drip (detachment 14 Ma after model C2). These are visible in the time shifts of subsidence in Figure 5.10*a*, the peak of the Bouguer gravity anomaly in Figure 5.10*b*, and the onset of the increase in surface heat flow in Figure 5.10*c*.

5.3.8 Density of the SNSM Massif (Set E)

Gravity studies of northern Colombia (e.g., Ceron-Abril, 2008; Sanchez and Mann, 2015; Sanchez-Rojas and Palma, 2014) argue that the crystalline rocks of the Grenvillian basement that underlies most of the SNSM massif appears to have a higher density, compared to the surroundings (e.g., at least between 100 - 400 kg/m^3 higher, according to gravity models in Sanchez and Mann (2015)), and that this is a significant contribution to the observed positive Bouguer gravity anomaly. The effects of a locally higher density are studied in model set E, where the upper crust in the 125 km wide elevated region has a density that is 100 kg/m^3 higher.

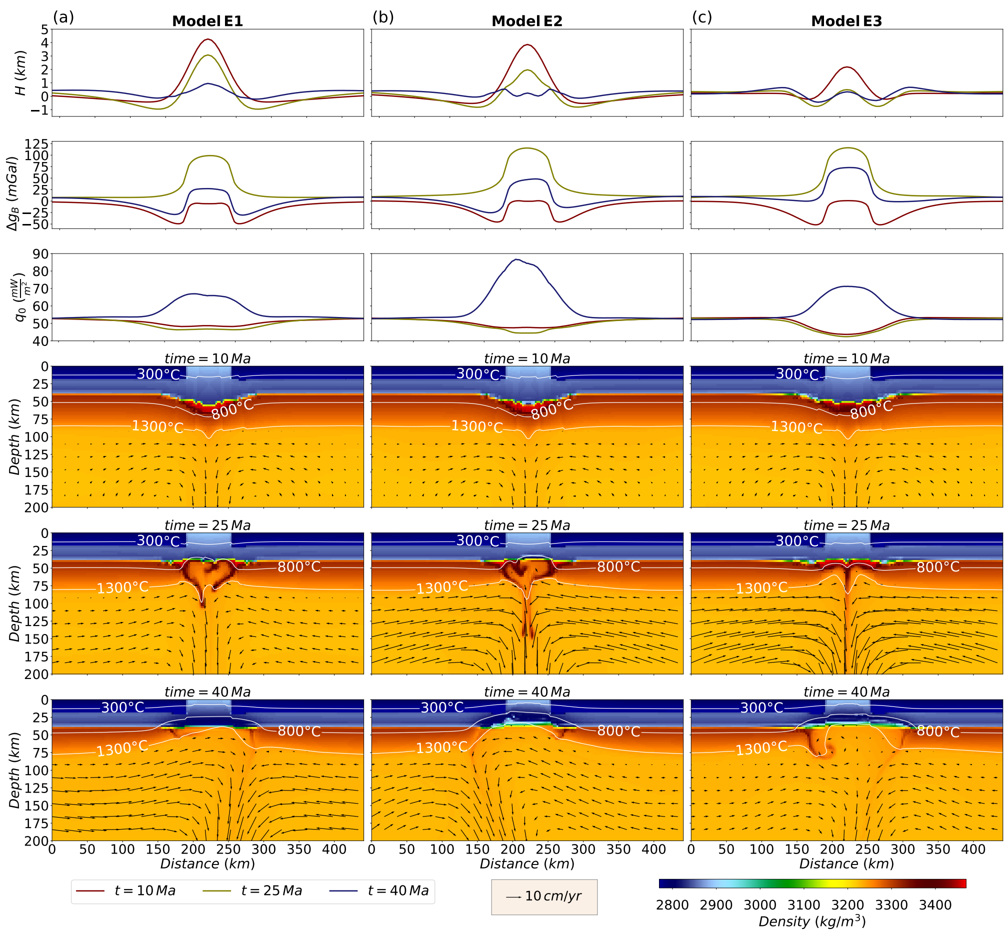

Figure 5.11: Evolution of (a) model E1, (b) model E2 and (c) model E3, including snapshots of density structures and profiles of topography (H), Bouguer gravity anomaly (Δg_B) and surface heat flow (q_0), at times before, during and after the main lithosphere removal episode. Set E is as set C, but it includes high-density upper crustal rocks in the perturbed region (100 kg/m^3 increase).

The setups and rheological configurations of models E1, E2, and E3 are the same as models C1, C2, and C3, respectively, differing only in the upper crust density in the central region (see table 5.2).

The results of set E are shown in Figure 5.11 and the temporal variations in surface observables are shown in Figure 5.12, together with the results of model C1 as a reference. The overall behaviour and effects of rheological variations remain the same as in set C, and there is little effect on the surface heat flow. However, the elevation is consistently lower (at most 0.8 km lower), showing that the additional load of the dense rocks significantly opposes to the upward stresses from the rising sublithospheric mantle. On the other hand, the trend of the gravity anomaly remains unchanged, but the presence of the high-density rocks results in higher gravity anomalies (>+50 mGal) with peaks during root detachment (at about t=25 Ma).

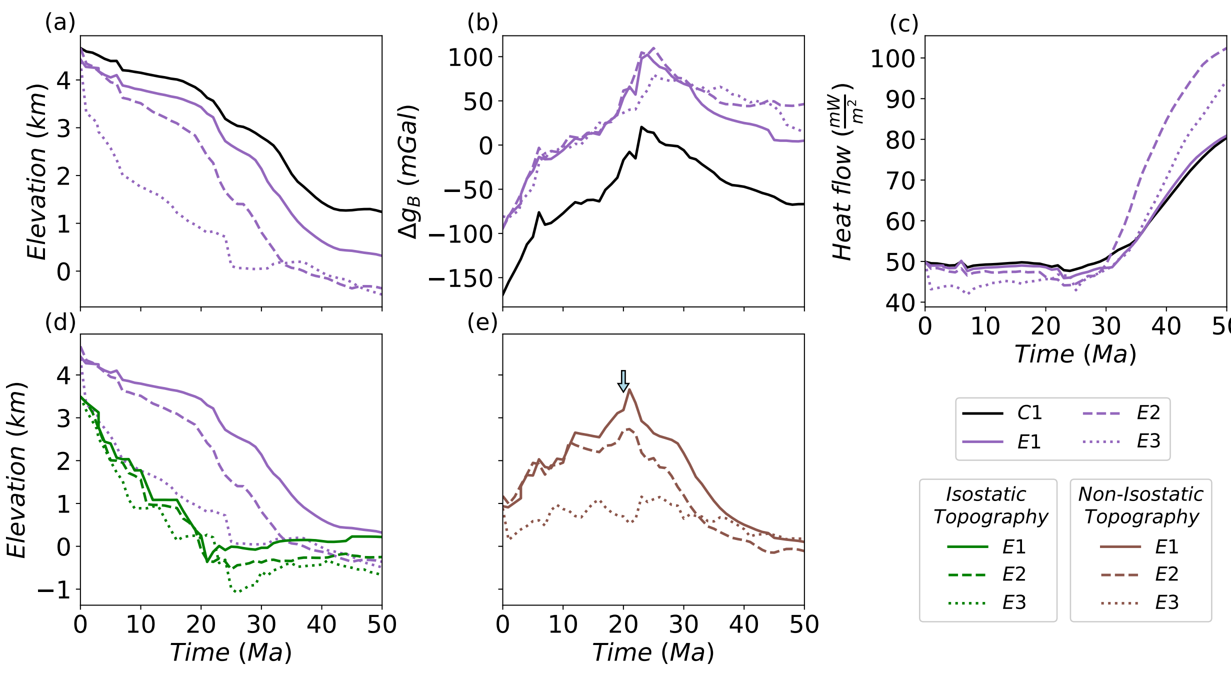

Figure 5.12: Time variation of surface observables, averaged over a 50 km width centred in the perturbed, for modelling set E, and model C1 as a reference. (a) Surface elevation. (b) Bouguer gravity anomaly (Δg_B). (c) Surface heat flow. (d) Isostatic topography (green) with total topography as a reference (purple). (e) Non-isostatic topography. Blue arrow indicates time of maximum uplift rate (0.37 mm/yr) right before total crustal root removal.

5.3.9 Effect of Regional Compression and Crustal Root Amplitude (Set F)

The SNSM is located close to the margin between the Caribbean and South American plates, and therefore plate boundary forces may have affected the evolution of this region. Plate reconstructions show that convergence rates in the Caribbean after the late Cretaceous have likely subjected the massif to variable magnitudes of horizontal stresses (e.g., Müller et al., 1999). Lateral compression could alter the dynamics of lithosphere removal, it should be considered in the models. However, because convergence rates have changed in time and part of the compression may have been accommodated on faults outside the SNSM, it is unclear how much compression may have been transferred to the SNSM. There are also no constraints on the total lithosphere shortening and thickening within the SNSM. Consequently, the previous models (Model A and sets B, C, D and E) use an imposed initial thickening. In Model Set F, the effects of compression and initial thickening are examined. These models use the same parameters of model E2 but the lateral boundary conditions are modified to produce an inflow velocity in the lithosphere which is balanced with outflow in the sublithosphere mantle; this approach was used in Chapter 4 (Figure 4.5). Models in this set (F1 to F11) test different combinations of compression rates (0, 0.5, 1.0 and 1.5 mm/yr) and initial crustal root amplitudes (20, 30 and 40 km); Model E2 has a compression of 0 mm/yr and a 30 km initial root.

The individual results of models of set F and the corresponding surface expressions are shown in Appendix B. The overall behaviour of models F1 to F11 resembles that of model E2 (Figure 5.12*a*-*c*), with only minor differences. In general, crustal compression produces uplift at later times. However, during root removal, compression restricts uplift because it enhances plastic strain, producing weak zones close to the surface (as seen in chapter 4). When the initial lithospheric thickening is higher, the drip occurs more quickly owing to the higher initial perturbation, and the additional load induces higher subsidence rates after crustal root removal.

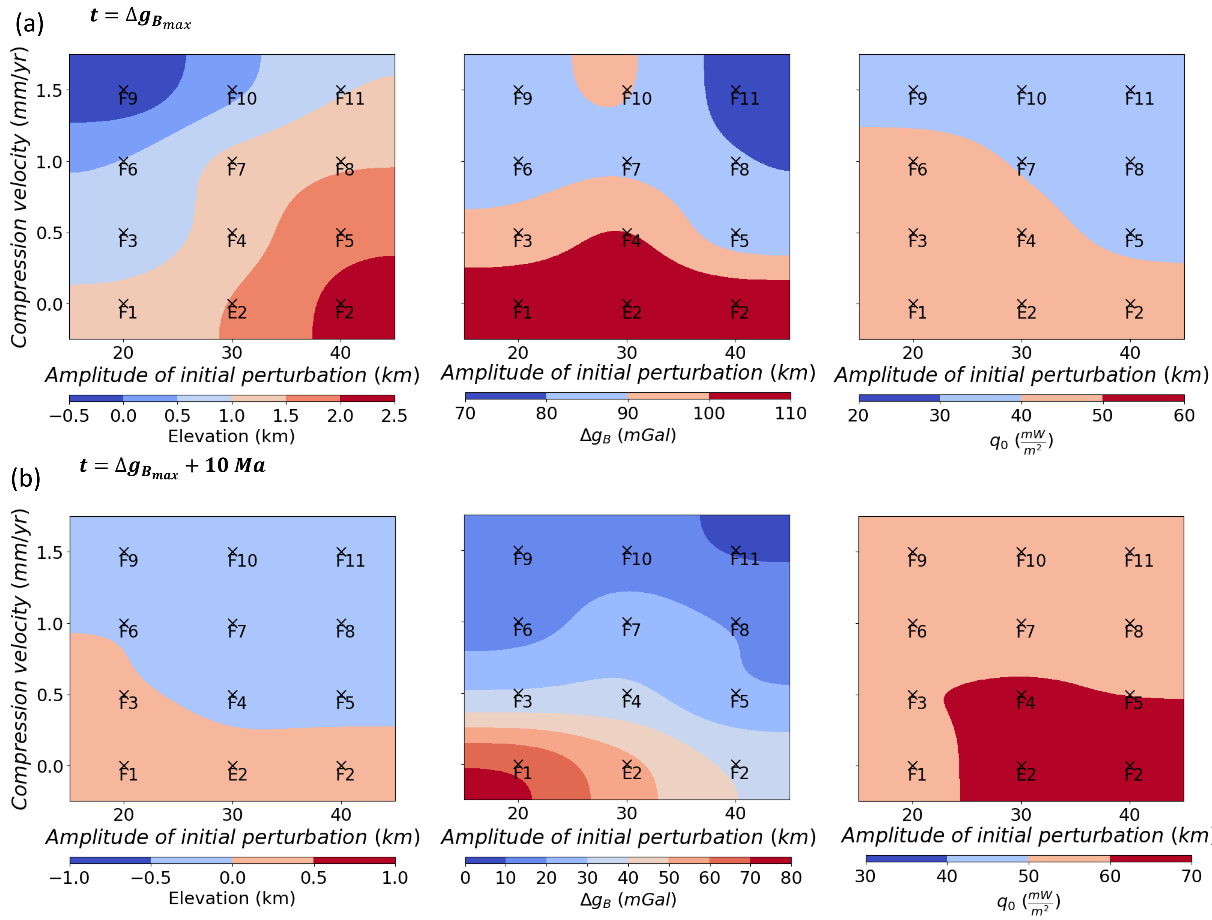

Figure 5.13: Magnitude of surface elevation, Bouguer gravity anomaly (Δg_B), and surface heat flow (q_0) (from left to right), averaged over a 50 km width centred on the perturbed region, (a) at the time of the maximum gravity anomaly after crustal root removal, and (b) 10 Ma after the peak gravity anomaly after root removal. The latter is shown for models of set F (but with model E2 as a reference), as a function of lateral compression rate (y-axis) and initial crustal root amplitude (x-axis).

The effects of compression rate and initial lithospheric thickening are shown in Figure 5.13 showing the surface elevation, Bouguer gravity anomaly, and surface heat flow at the time of the maximum peak of gravity anomaly after removal (t=tΔg_{max}) and 10 Ma after. As expected, an increase in crustal thickness in the perturbed region produces a decrease in surface heat flow and an increase in surface elevation. However, the gravity anomaly shows a trade off because when the crust is thicker, the gravity anomaly is lower, but at the same time there is more eclogitization and a larger portion of the lower crust is removed, producing a greater increase in the gravity anomaly after removal. This results in higher gravity anomalies for intermediate initial thicknesses (i.e., an initial perturbation of 30 km). On the other hand, Figure 5.13 shows that an increase in lateral compression velocity results in a decrease in the gravity anomaly and surface heat flow because it induces crustal thickening. There is a trade off between the uplift produced by compression and the increase in subsidence caused by the enhanced plastic strain in the crust and the formation of weak zones. The behaviour is dominated by plastic strain induced by compression, resulting in lower topographies at higher compression velocities. The observed trends in gravity anomaly and surface heat flow are maintained after 10 Ma, but by this time, the topography has collapsed in all models.

5.4 Geological and Geophysical Implications

5.4.1 Comparison With Observations

The models in this chapter test the hypothesis that the observed high topography and positive Bouguer gravity anomaly in the SNSM can be explained by lithosphere removal via a drip. Of the models examined in this chapter, the model that best fits the observations is Model E1 (model of set E, with no lateral compression and DMD lower crust rheology) as it produces the highest simultaneous gravity anomaly and elevation after removal. This is a consequence of the following points: a weak local mantle lithosphere rheology produces a fast removal (within 25 Ma) and allows less time for post-drip subsidence, a strong lower-crustal rheology (DMD) provides more support for the load of the initial topography, and the high-density upper crustal rocks in the perturbed region produce a significant contribution to the Bouguer gravity anomaly.

Therefore, the results of Model E1 are used for comparison to the observations in the SNSM in Figure 5.14. The model results are shown at a model time of 23 Ma, corresponding to the maximum peak in the gravity anomaly, when the crustal root has been removed ($\sim$2 Ma before full detachment). At this time the local Bouguer gravity anomaly is the result of the trade off between the absence of cool and dense mantle lithosphere underneath (lack of mass), the high-density shallow rocks in the SNSM (100 km/m^3 denser), and a locally thin crust ($\sim$38 km) directly underlain by a shallow sublithospheric mantle (excess of mass near the Moho). While there are still uncertainties in the exact crustal thickness in the SNSM, this value is close to the estimates in Sanchez-Rojas and Palma (2014) and Poveda et al. (2018), of about 35 km.

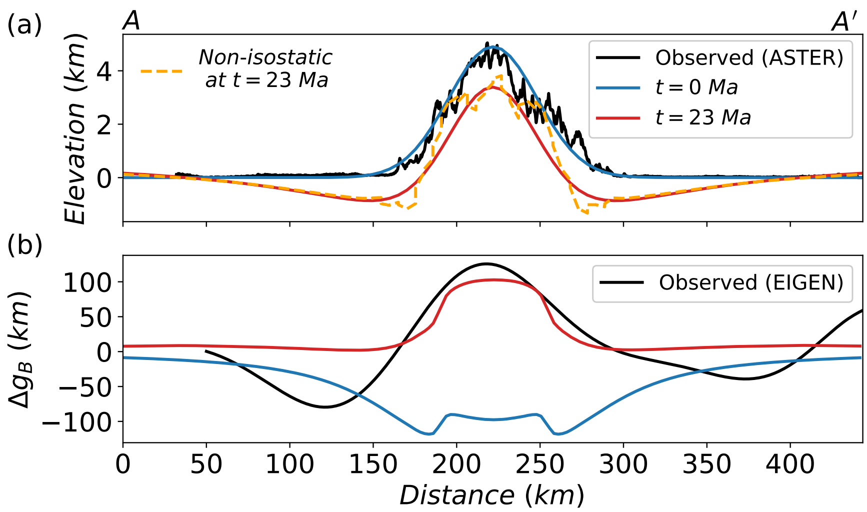

Figure 5.14: Comparison between topographic and Bouguer gravity anomaly profiles of the preferred model (model E1) right after crustal root removal ($t = 23$ Ma), with observed data. Initial topographic and gravity anomaly profiles ($t = 0$ Ma) are shown as a reference. (a) Modelled topography compared to observed data from the ASTER global digital elevation model V003 (Spacesystems & ASTER Science Team, 2019). The non-isostatic topographic profile at $t = 23$ Ma shows that non-isostatic effects are localized in the elevated region and that at this time, most of the topography is non-isostatic. (b) Modelled Bouguer gravity anomaly compared to observed data from the EIGEN-GL04C global gravity field model (Förste et al., 2008). Observed profiles are extracted along the line indicated in Figure 1.1a.

The observations are taken along a SW-NE profile across the SNSM (location in 1.1a), with the Bouguer gravity anomaly from the EIGEN-GL04C Global gravity field model (Förste et al., 2008) and the surface topography from the ASTER Global Digital Elevation Model V003 (Spacesystems & ASTER Science Team, 2019). The maximum modelled values for the Bouguer gravity anomaly and surface elevation are of +103 mGal and 3.3 km, respectively, compared to the maximum observed values of +126 mGal and 5.1 km. The observed gravity shows that the positive peak is surrounded by two negative peaks that are associated with the low-density sediments of the lower Magdalena basin southwest of the SNSM and the Baja Guajira basin to the northeast. These gravity minima do not appear in the modelled gravity anomaly since the surrounding basins are not considered in the numerical model.

5.4.2 Isostatic vs. Non-Isostatic Topography

The modelled topography is the result of both the density structure of the model (i.e., isostatic gravity), as well as the dynamics of the model. This means that aside from isostatic effects, topographic alterations include the effect of the downwelling of the lithosphere during the drip, upwelling of the sublithospheric mantle following the drip, and lateral lithosphere strength. In order to assess the relative contributions of these, isostatic topography calculations for models of set E are shown on Figure 5.12*d*. This is defined as the topography that would be observed if the model was in isostatic equilibrium, based on the modelled density structure (Figure 5.12*d*). Figure 5.12*e* shows the non-isostatic part of the topography, calculated by taking the difference between the total topography and its isostatic part. These figures show that the isostatic topography is significantly lower than the total topography throughout the removal episode for models E1 and E2, while model E3 is closer to isostatic balance. This suggests that the topographic support provided by a rheologically stronger lower crust in model E1 is significant, while the mechanical decoupling produced by a weaker lower (e.g., model E3) crust limits the transfer of vertical stresses from the upwelling mantle to the surface. In model E1, the non-isostatic topography reaches a maximum peak of 3.5 km at 23 Ma, suggesting that the coexistence of a positive Bouguer gravity anomaly and high topography at this time is only possible due to the delay in subsidence produced by non-isostatic effects. Figure 5.14*a* shows the profile of non-isostatic topography right after root detachment, showing that at 23 Ma the topography is predominantly non-isostatic.

5.4.3 Melting

The lithosphere drip results in a thinning of the lithosphere and causes upwelling of the sublithospheric mantle to fill the gap created by the drip. Upwelling and decompression of sublithospheric mantle with simultaneous lower crustal heating have led to the suggestion that lithospheric removal can induce melting of both the mantle and crust, and therefore magmatism may accompany lithosphere removal (e.g., Kay and Mahlburg Kay, 1993; Mahlburg Kay et al., 1994). In this section, the pressure-temperature conditions in model E1 are used to assess whether melting is predicted. The calculations presented use the dry granite and dry peridotite solidus from Elkins-Tanton (2005), to consider lower crustal and mantle melting, respectively.

Figures 5.15*a* and 5.15*b* show the model E1 at 10 Ma after removal (t = 33 Ma) to allow enough time for significant melt production. The highlighted regions show where the crust and mantle are above their solidus temperature, confirming that upwelling of sublithospheric mantle could produce decompression melting in the shallow mantle and deep crust in the region of lithosphere removal. There is also a thin zone at ∼90 km depth outside of the main drip region where lower mantle lithosphere has been partially removed and conditions favour melting.

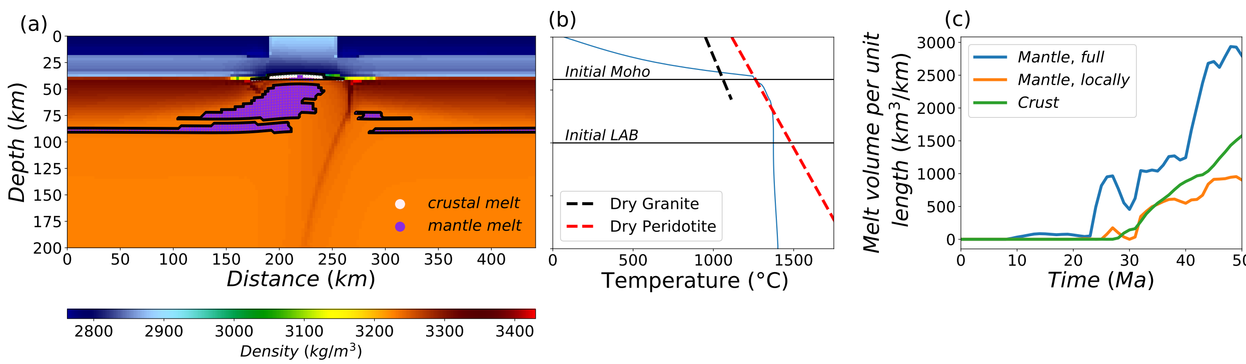

Figure 5.15: (a) Density structure of the preferred model (Model E1) at t = 33 Ma (10 Ma after removal). Contours enclose regions where the P-T conditions are above the dry peridotite and dry granite solidi, for the mantle (purple infill) and lower crust (white infill), respectively. (b) Temperature profile at x=230 km and t = 33 Ma, with the dry peridotite and dry granite solidi from Elkins-Tanton (2005). (c) Calculations of melt volume per unit length along strike for the lower crust (assuming 0.75% of melt per degree above the solidus) and mantle (assuming 0.3% of melt per degree above the solidus). Local mantle melt volume is the melt volume in a 60 km width centred in the elevated region.

Figure 5.15*c* shows the temporal evolution of mantle melt volume (per unit along strike) for both the full model domain and for a local 60 km wide region centred in the elevated zone. This is calculated by monitoring the regions of the model that are above the solidus, assuming a melt fraction per Kelvin above the solidus of 0.3% for the mantle (Katz et al., 2003) and 0.75% for the crust (Annen & Sparks, 2002). The initiation of melting coincides with the onset of mantle upwelling after lithosphere removal (at about 23 Ma), and suggests that mantle and crustal melt volumes in the region of interest could be significant, with approximately equal amounts of each. These calculations show the possible volume of melt and the spatial and temporal distribution. The models do not include the transport of melt to the surface, nor the effects of melt on rheology and density. Further work is needed to assess these factors.

5.4.4 Seismic Velocity Structure

The models provide predictions of the temperature, pressure and composition structure at each point in the model domain over time. In this section, the structure of model E1 at a time of 23 Ma (time of the maximum Bouguer gravity anomaly) is used to calculate the expected seismic velocity structure, as an additional observation that could be used to test the idea of a lithospheric drip. The conversion of the model results to seismic velocity structure uses three steps, following the method described in Goes et al. (2000), Sobolev et al. (1996), and van Wijk et al. (2008).

First, the PerpleX code (Connolly, 2005) is used to estimate values of the bulk and shear moduli at the pressures and temperatures of the model. In this step it is assumed that the compositions of the mantle lithosphere and sublithospheric mantle are both represented by the composition of a pyrolite, following van Wijk et al. (2008) (Composition shown in table 5.4). Because the purpose of this estimations is to quantify the effect of lithosphere removal in the seismic structure of the upper mantle (for the preferred model), and because the crust has diverse and complex compositions, the crust is excluded from this analysis.

In the second step, the anharmonic seismic wave velocities at each point in the model domain are calculated by applying the density structure from the model, and the estimated values of the bulk and shear moduli into equations (5.1):

$$V_p = \sqrt{\frac{k + \frac{4}{3}\mu}{\rho}} \quad , \quad V_s = \sqrt{\frac{\mu}{\rho}} \tag{5.1}$$

where k is the bulk modulus, μ is the shear modulus, V_p is the anharmonic seismic velocity of the p-waves, and V_s is the anharmonic seismic velocity of the s-waves. In the final step, the anharmonic velocities are then corrected for attenuation using equation (5.2):

$$V_{p,s_{ane}} = V_{p,s_{anh}} \left[1 - \frac{Q_{p,s}^{-1}}{2tan\frac{\pi a}{2}}\right] \tag{5.2}$$

where $V_{p,s_{ane}}$ is the anelastic velocity (for either p or s waves), $V_{p,s_{anh}}$ is the anharmonic velocity (for either p or s waves), a is a constant describing the frequency dependency of attenuation and $Q_{p,s}$ is the quality factor for either the P and S waves. Q_p and Q_s are calculated following (5.4) and (5.3), respectively:

$$Q_s = Q_0 \omega^a e^{\frac{agT_m}{T}} \tag{5.3}$$

$$Q_P = \left[\frac{(1 - \frac{4}{3}\left(\frac{V_s}{V_p}\right)^2)}{Q_k} + \frac{4}{3Q_s}\left(\frac{V_s}{V_p}\right)^2 \right]^{-1} \tag{5.4}$$

where Q_0 is the pre-factor constant, g is the thermal scaling factor, ω is the mean frequency content, Q_k is the bulk attenuation, and T_m is the melting temperature (assumed as the dry peridotite solidus in Figure 5.15*b*, from Elkins-Tanton (2005)). The parameters used for the attenuation correction follow the approach in van Wijk et al. (2008), and are reported in Table 5.5.

Table 5.4: Compositions in oxides in volume percentage used for seismic wave velocity estimations in the upper mantle from van Wijk et al. (2008).

Composition name	**MgO**	**FeO**	**CaO**	$\mathbf{Al_2O_3}$	$\mathbf{SiO_2}$
Pyrolite (Sun, 1982)	48.53	5.72	3.50	1.80	38.66

Table 5.5: Parameters for anelastic attenuation correction, following approach in van Wijk et al. (2008).

Depth	$\mathbf{Q_0}$	**a**	ω	**g**	$\mathbf{Q_k}$
0-200km	0.1	0.15	0.02Hz	40	1000

Figure 5.16*a* shows the predicted P and S wave velocities for Model E1 immediately after lithosphere removal, as well as their anomalies. The velocity anomalies (Figure 5.16*b*) are calculated by computing the percentage difference between the seismic wave velocity (P or S) at each point in the domain with the average velocity (P or S) in its corresponding depth. This shows that a drip event should leave a region of thinned lithosphere, which has a clear low velocity anomaly of up to -5% for P-waves and -7.5% for S-waves, with minimum values of

7.6 and 4.1 km/s, respectively. Figure 5.16a also includes contours delimiting regions where the pressure and temperature conditions are above the mantle solidus and thus, the seismic wave velocities could be lower than the predicted values if melt is present.

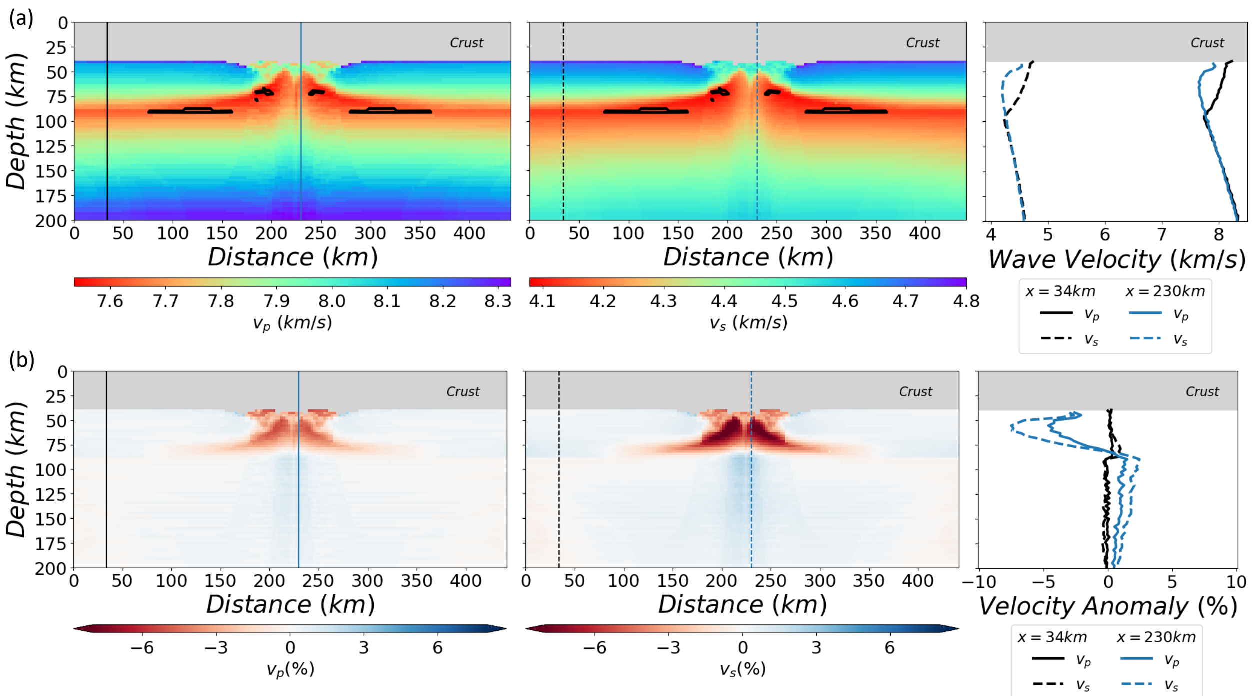

Figure 5.16: (a) Seismic wave velocity predictions from the preferred model (model E1) at t = 23 Ma (right after removal), using the PerpleX code (Connolly, 2005), showing P-wave structure (left), S-wave structure (centre), and vertical profiles at the side (x = 34 km) and centre (x = 230 km) of the model domain. Black contours enclose regions where the P-T conditions are above the dry peridotite solidus, which could have lower velocities. (b) P and S wave velocity anomalies and profiles at the side (x = 34 km) and centre (x = 230 km) of the modelling domain.

5.5 Discussion

5.5.1 Model Summary

The SNSM in northern Colombia is an unusual mountain that is characterized by high topography and a positive Bouguer gravity anomaly. The numerical models in this chapter test the idea that these observations may be explained by a lithosphere drip event, initiated by previous crustal thickening. All models show that eclogitization and subsequent crustal root removal produce a rapid increase in the gravity anomaly while mantle upwelling provides additional support for the load of the initial topography.

In model E1 (the preferred model), the magnitudes of the surface topography and Bouguer gravity anomaly are the closest to the observations in the SNSM, suggesting that a rheologically stronger lower crust can hold the load of the mountain for longer times after lithosphere removal, and that the gravitational effect of both the shallow high-density rocks of the exhumed basement and absence of crustal root are required to account for the observed positive gravity anomaly. Figure 5.14 shows that the initial gravity anomaly of model E1 is negative (about -100 mGal) even with the presence of denser upper-crustal rocks, indicating that the effect of the thick low-density crustal root dominates. After the lithosphere removal event, the Bouguer gravity becomes positive (+103 mGal) and remains positive for almost 30 Ma while it progressively decreases. On the other hand, for model sets B and C, even though the gravity anomaly right after removal is positive (about +30 mGal) (Figure 5.3*b*), it is still well below the SNSM observations, indicating that higher density upper-crustal rocks are also required. The non-isostatic topography (Figure 5.14*a*) confirms that high elevation in model E1 right after removal is mostly related to dynamic effects, such as mantle upwells, which are localized in the elevated region.

The models also provide insights into how lithosphere rheology affects the dynamics and surface expressions. The preferred models use a wet olivine rheology in the mantle lithosphere (WO). This results in rapid removal, where detachment occurs 8-10 Ma after complete eclogitization, facilitating the coexistence between high elevations and positive gravity anomalies. Similarly, a weaker eclogite rheology enhances the rate of removal and the associated high elevations and positive gravity anomalies. Results from set E show that even though there is uncertainty about eclogite rheology, this parameter only affects the timescales of crustal root removal. A relatively weak rheology for the crust and mantle is consistent with the fact that the SNSM is located near a convergence plate margin, where lithosphere hydration and weakening may be expected.

Stresses transferred from regional compression constitute an additional force that could produce uplift and provide support. Model set F examines this effect, although it should be noted that the models do not include any pre-existing faults and weak zones; if these are present adjacent to the SNSM, the magnitude of transferred to the mountain may be less than modelled here. The models in section 4.6 show that high compression velocities (>1.5 mm/yr) would thicken the crust during the drip without giving enough time for eclogitization, and thus preventing the full removal of the crustal root and limiting any increase in the gravity anomaly. Conversely, compression velocities within the range presented in this chapter (≤1.5 mm/yr) are low enough to allow for full crustal root removal, allowing for a positive gravity anomaly. Lateral compression only produces significant uplift at later modelling times (>40 Ma), which suggests if there is continental compression in northern Colombia, either it is accommodated in the region surrounding the SNSM or lithosphere removal in the SNSM has occurred recently (in the last 10 Ma).

Crustal root thickness before the proposed lithosphere removal event is uncertain. Model set F shows that this strongly affects the magnitudes of the surface observables. In models with lateral compression, the surface elevation at the time of the peak in Bouguer gravity anomaly (i.e., the time of lithosphere removal) is largest for an intermediate initial crustal root thickness (30 km) with low compression rate (0.5 mm/yr or less). This suggests that the root that preceded the removal episode in the SNSM could have had a similar amplitude. The effect of horizontal compression and initial thickening on the resultant observables is also applicable to other regions where lithosphere removal has been proposed (e.g., Bao et al., 2014; Saleeby et al., 2012). These models highlight that lithosphere removal can produce a wide variation of surface effects, depending on the initial configuration and tectonic context.

5.5.2 Implications From Surface Heat Flow and Elastic Thickness

In the preferred model (E1), surface heat flow immediately after removal is of 46 $\frac{mW}{m^2}$, and only reaches the values of 60-80 $\frac{mW}{m^2}$ reported by Quintero et al. (2019) for the SNSM after approximately 15 Ma. This implies that if lithosphere removal has occurred in the SNSM, both the gravity anomaly and surface topography have to be sustained for at least 15 Ma to match the observations of heat flow. However, heat flow measurements in the study region are sparse and have large uncertainties, and additional data should be collected.

Elastic thickness is another measurement that provides constraints on lithosphere structure. Previous studies suggest an elastic thickness of 30-40 km in the SNSM (e.g., Arnaiz-Rodríguez and Audemard, 2014; Tassara et al., 2007). This is consistent with a cool lithosphere (e.g., Hyndman et al., 2009) and suggests a relatively low surface heat flow (<60 $\frac{mW}{m^2}$), as predicted by model E1 when the Bouguer gravity anomaly is maximum (after lithosphere removal). This means that there is a discrepancy between elastic thickness and surface heat flow estimations (possibly resulting from their large uncertainties) that should be examined in future work, to provide a consistent constrain for the lithosphere structure in the SNSM.

If the elastic thickness is as large as estimated by Arnaiz-Rodríguez and Audemard (2014) and Tassara et al. (2007), the elastic strength of the lithosphere provides an additional support for the load of the massif. If that is the case, both the elastic support and the upward stresses from the sublithospheric mantle could allow for uplift, rather than subsidence, after removal. The elastic strength would also prevent crustal thickening following the removal event, and therefore, the positive gravity anomaly could be sustained for a longer time. The current models do not include elasticity, but this is something that should be explored in future work.

5.5.3 Lithosphere Removal in the Eocene (50-40 Ma)

As argued above, a subset of the numerical models predicts surface observations (elevation, Bouguer gravity anomaly and surface flow) that are consistent with those observed in the SNSM today. From this, it appears that a local lithosphere removal event may explain the SNSM observations. I propose two possible times for the removal event: an older event in the Paleogene (50-40 Ma) or a recent event (within the last 2 Ma).

The first possibility is that lithosphere removal occurred before the slab flattening that has been proposed to explain the cessation of Paleocene-Eocene magmatic activity (e.g., Taboada et al., 2000). In principle, because there are not enough constrains to assert a specific timing for a lithosphere removal episode, it could have occurred anytime after the Paleogene. However, the hypothesis of an event before slab flattening (50-40 Ma ago) has the advantage that at that time, the underthrusting Caribbean slab could not block lithospheric foundering.

In this case, the current high elevations require that elastic stresses, mantle upwelling and support from the present-day Caribbean slab have acted for a long time. As shown in section 5.4.3, lithosphere removal induces melting and therefore a removal event may be recorded in surface magmatism (e.g., Kay and Mahlburg Kay, 1993; Mahlburg Kay et al., 1994). Duque-Trujillo et al. (2019) argue that Paleocene-Eocene magmatic events do not correspond to typical Andean-type subduction magmatism because they were localized, low-volume and short term (±10 Ma). They propose that the melting of thickened lower crust could produce the required parental magma, instead of a typical subduction system. The models in this study show that crustal root removal takes place in timescales close to 10 Ma (time between onset and full removal of the crustal root), and that lower-crustal and shallow sublithospheric mantle melts can be generated by decompression and subsequent heating after removal (Figure 5.15), suggesting that if it occurred during the Paleocene-Eocene, its role in melt production could have been important because it provides a heating mechanism and different melt sources. It should also be noted that if a removal event occurred within the Paleocene-Eocene arc, the arc itself may have also contributed to the removal process. Ducea et al. (2021b) argue that melt extraction at an arc contributes to root densification by creating a lower layer of high-density "arclogite" rocks. These have been shown to promote gravitational removal (e.g., Jull and Kelemen, 2001).

5.5.4 Recent Lithosphere Removal (<2 Ma)

The problem with an Eocene removal event is that the surface expressions must persist for >40 Ma, and the models in this study show only a short-lived period of high elevation and positive Bouguer gravity anomaly. Therefore, the other possibility is that removal occurred recently. Here, I propose that a removal event within the last 2 Ma can explain the observations.

Villagómez et al. (2011) argue that there has been very recent uplift in this region (in the last 2 Ma) on the basis of the absence of measurable exhumation episodes in the last 16 Ma, the highly erosive climate in the SNSM, and the current high topography. However, in most of the models in this study (including the preferred model E1) lithosphere removal is followed by surface subsidence suggesting that the upward force of the buoyant sublithospheric mantle is not sufficient to overcome the load of the mountain and to induce uplift right after the removal of its root. Instead, upward forces from the sublithospheric mantle are only enough to delay the subsidence of the mountain providing some support. Arnaiz-Rodríguez and Audemard (2014) suggests that elastic strength in the crust is enough to sustain the SNSM massif. If that is the case, dynamic forces from the mantle could produce uplift. For instance, calculations of the non-isostatic contribution to topography (e.g., Figure 5.12), show that the model dynamics produces a maximum uplift rate of 0.37 mm/yr for model E1, at the onset of the drip (t=21 Ma). If it is assumed that the modelled data after removal (i.e., t=23 Ma for model E1) corresponds to the present, the latter implies the occurrence of maximum uplift rates ±2 Ma ago, consistently with the timing of the recent uplift proposed by Villagómez et al. (2011).

The models in this study show that both the high Bouguer gravity anomaly and surface topography have to be sustained for at least 15 Ma to match the observations of heat flow reported by Quintero et al. (2019) (see section 5.5.2). This suggests that lithosphere removal within the last 2 Ma would be consistent with a lower surface heat flow (e.g., 50-60 $\frac{mW}{m^2}$) compared to the values reported (60-80 $\frac{mW}{m^2}$). On the other hand, the elastic thickness estimated in the SNSM (30-40 km) (e.g., Arnaiz-Rodríguez and Audemard, 2014; Tassara et al., 2007) suggests a cool lithosphere and a relatively lower surface heat flow (<60 $\frac{mW}{m^2}$) (e.g., Hyndman et al., 2009), which according to the models, is consistent with lithosphere removal in the last 2 Ma. Additional local elastic thickness estimations and heat flow data are required to reduce the large uncertainties in current measurements and provide better constrains.

If lithosphere removal took place any time after the Eocene (e.g., in the last 2 Ma), the characteristics of the Paleocene-Eocene magmatism could provide evidence indicating the presence of a partially densified crustal root by the Paleogene, as evidence for a subsequent removal. Duque-Trujillo et al. (2019) report that that the most recent magmatism in the SNSM produced the Paleocene Leuco-granites and the Eocene Santa Marta Batholith (SMB). There, it is shown that the protolith of the leuco-granites had a mafic composition, under the stability field of amphibole, garnet and rutile, which according to Ducea et al. (2021a), are all common minerals within arclogite assemblages. Also, Duque-Trujillo et al. (2019) report that the SMB has substantial ultramafic garnet-free cumulates, from which some have been classified as pegmatitic pyroxenites, perhaps showing evidence of a densified lower crust outside the stability field of garnet, which could be gravitationally unstable. These mafic intrusions should be studied further regarding the possibility of lithosphere removal.

Additional evidence that favours the recent lithospheric drip hypothesis comes from seismic observations in this area. For instance, seismic wave tomographies reported by Poveda et al. (2018) and Syracuse et al. (2016) consistently show low shear wave velocities (<3.8 km/s) in the region of the mountain at depths between 30 to 35 km which, according to the crustal thickness map in Poveda et al. (2018), is right below or close to the Moho (Figure 5.17). These values are consistent with the shear wave velocity estimations from our preferred model (model E1), reported in Figure 5.16*a*.

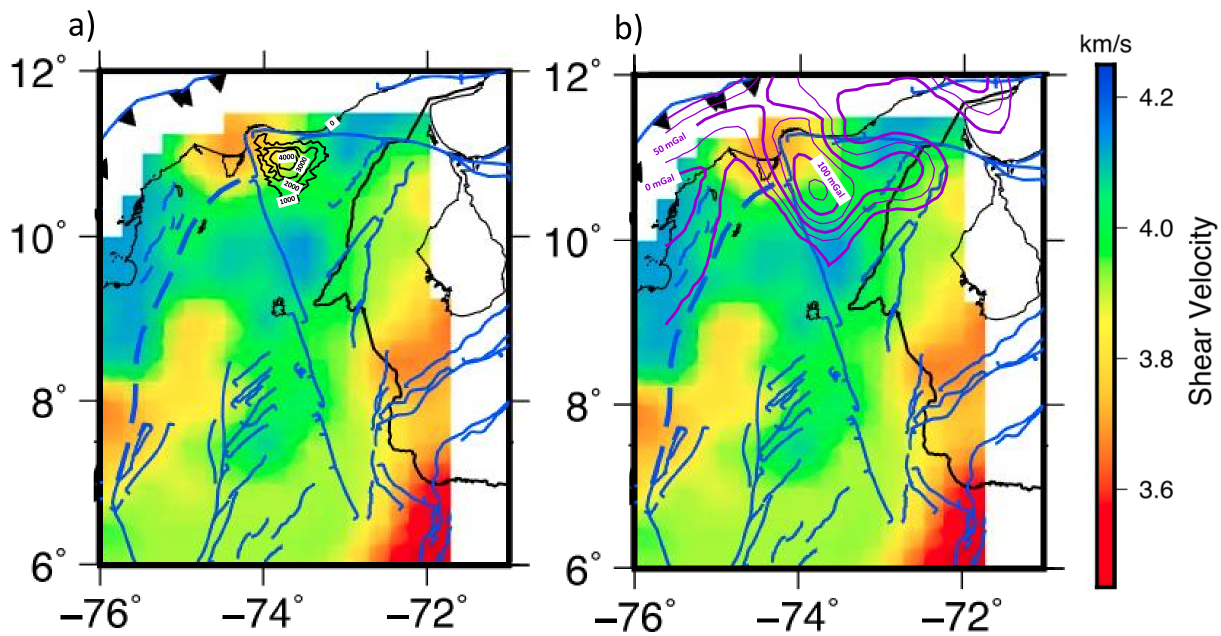

Figure 5.17: Shear wave velocity maps at a depth of 35 km modified from Poveda et al. (2018). Blue solid lines show major faults and the dashed blue line indicates the Romeral suture. The seismic velocity maps show a local low velocity under the SNSM consistently with model predictions in Figure 5.16. a) Shear velocities at a depth of 35 km with topographic contours (black) in the region of the SNSM only. b) Shear velocities at a depth of 35 km with contours (purple) of the Bouguer gravity anomaly above 0 mGal.

5.5.5 Model Limitations

The models presented in this chapter explore the dynamics of a lithosphere drip and how this is recorded in surface observations, including topography, Bouguer gravity anomaly, surface heat flow, melting, and seismic velocities. The models are two-dimensional cross-sections based on the structure of the SNSM. However, the SNSM is a localized mountain and thus a 3D geometry may be more appropriate. This is examined in Chapter 6.

In addition, the models do not include elasticity in the numerical formulation. This is important because due to the high elastic thickness and the relatively narrow width of the massif, elastic strength should provide significant support for the SNSM. Also, models do not test the effect of eclogitization rate, and instead, the phase change occurs instantaneously once the pressure and temperature conditions for the reaction are achieved. This assumes that there is enough hydration in the crustal root such that the time taken for a full reaction is negligible compared to the timescales of the models but depending on rock composition and hydration it could be significant. Moreover, the models do not include magma migration and the effect of melts on density and rheology. This might be significant because the presence of melts could significantly weaken the crust enhancing its deformation. These are parameters that should be investigated further in future work.

Finally, the models address only the dynamics of the continental lithosphere, and do not include the subducting Caribbean slab. Seismic studies in northwestern South America (e.g., Cornthwaite et al., 2021; Londoño et al., 2020; Taboada et al., 2000; Van Der Hilst and Mann, 1994; Vargas, 2020) show that the Caribbean plate subducts or underthrusts the South American plate at a shallow angle (<30°) near the Colombian coast, and then steepens at some point into the continent. However, there are uncertainties in the slab location and depth. For instance, Vargas (2020) proposes that the Caribbean plate may transition from a flat subduction close to the Caldas Tear (5°-8°N), to a steeper subduction under the SNSM. It is unclear how the presence of the Caribbean plate may affect lithosphere removal, especially if the removal event occurred in the last 2 Ma. On one hand, the Caribbean plate may hinder the foundering of a crustal root; on the other hand, subduction may induce a lateral drag that promotes removal (e.g., Currie et al., 2015). Future models should include Caribbean plate subduction in order to assess its effect on the dynamics and structure of the overlying continent, including the SNSM.

5.6 Summary and Conclusions

The SNSM is an anomalous high-elevation region of northern Colombia where there is a high and positive Bouguer gravity anomaly, suggesting an excess of mass. Previous studies have proposed that this could be produced by an unexpectedly thin crust (e.g., Case and Macdonald, 1973; Montes et al., 2005). However, considering that the SNSM formed a thick continental arc in the Jurassic (∼64 km thick) (e.g., Ramírez et al., 2020), that it experienced an arc-continent collision in the early Paleocene (e.g., Cardona et al., 2010), and is currently experiencing oblique convergence at a rate of 10-20 mm/year (e.g., Freymueller et al., 1993), it is not clear what could have produced a localized crustal thinning right under the SNSM massif, resulting in a ∼35 km thick crust (e.g., Sanchez-Rojas and Palma, 2014).

One hypothesis is that the SNSM observations may be explained by lithosphere removal, whereby a perturbation in the mantle lithosphere (generated by previous shortening) triggered a localized mantle lithosphere drip in which the lower crust is heated and crustal root eclogitization is induced. Eclogitization of the crustal root is characterized by an increase in density (reaching 3550 km/m^3) that results in its gravitational removal right after the mantle lithosphere drip. In the models presented, crustal root removal results in a locally thinner crust (∼38 km) underlain by buoyant sublithospheric mantle, producing a simultaneous high (and positive) Bouguer gravity anomaly with an elevated topography.

This chapter presented 2D thermal-mechanical numerical models to quantitatively examine the dynamics of the lithosphere and the associated surface expressions, especially surface topography, Bouguer gravity anomaly and surface heat flow. The models systematically examine how variations in crust and mantle lithosphere rheology, eclogite rheology, upper crust density, lateral compression, and initial perturbation affect the dynamics of a lithosphere drip and the surface observables. From the models, the following conclusions can be drawn:

- The timescales of lithosphere removal are significantly affected by the local mantle lithosphere rheology. In models with a wet (and thus weak) olivine rheology, mantle lithosphere drip and crustal root removal occurs within 25 Ma, while in models with a dry (and thus strong) olivine rheology it takes about 70 Ma.

- The timescales of the removal episode are also influenced by the eclogite rheology. For instance, an increase in eclogite viscosity of one order of magnitude can result in a ∼14 Ma delay in crustal root removal.

- Lower crustal rheology has a minor effect on the timescales of lithosphere removal and the effect is only noticeable if the process is slow (∼70 Ma) (i.e., when the mantle lithosphere rheology is dry and strong). In this case, the strong lower-crustal rheology of dry Maryland diabase can delay the removal by about 4 Ma with respect to the weak rheology of mafic granulite.

- If there is a weak lower crust all along the domain, there is less coupling between the lower crust and the upper mantle lithosphere. This can result in lithospheric delamination after crustal root removal (such as in models C3 and B3).

- Gravitational crustal root removal produces surface subsidence because of the pull of the drip, and the subsequent absence of isostatic support. However, a strong lower crustal rheology (e.g., dry Maryland diabase) provides more support and sustains the topography for longer with respect to a weak rheology (e.g., mafic granulite). For example, the average elevation of the mountain descends below 4 km at least 9 Ma later if lower crustal rheology is strong (i.e., dry Maryland diabase).

- Crustal root removal is followed by a peak in the Bouguer gravity anomaly which is a consequence of the resultant thinner crust (∼38 km) and the rise of the sublithospheric mantle right under the Moho (which produces a local excess of mass). Then, the Bouguer gravity anomaly progressively decreases because the topographic load sinks and spreads generating a downward deflection of the mid-crust interface, and because the density of the lower crust is progressively reduced (locally) owing to its increase in temperature. If upper crustal density is uniform (e.g., models in sets B and C), the peak in gravity anomaly is positive but low magnitude (e.g., 20-30 mGal).

- The observed magnitudes of the Bouguer gravity anomaly in the SNSM (>+100 mGal) require the gravitational effect of both, the high density shallow rocks of the Grenvillian basement (e.g., Sanchez and Mann, 2015), and crustal root removal resulting in a thinner crust (~38 km), such as in model set E.

- The preferred model is E1 because its conditions facilitate the coexistence of a high and positive Bouguer gravity anomaly and a high elevation (103 mGal and 3.3 km). These conditions are a weak local mantle lithosphere rheology that produces a fast removal (within 25 Ma) with less time for subsidence, a strong lower-crustal rheology that provides more support for the load of the initial topography, and high-density upper crustal rocks in the perturbed region that produce a significant contribution to the Bouguer gravity anomaly.

- After crustal root removal the topography is held by non-isostatic forces such as the upwelling of the sublithospheric mantle following the drip, and lateral lithosphere strength. In the preferred model (E1) the latter forces produce a maximum non-isostatic topography of 3.5 km at 23 Ma and maximum uplift rate of 0.37 mm/yr, at 21 Ma.

- The upwelling of hot sublithospheric mantle produces a delayed increase in surface heat flow because of the timescales required for crustal heating. In the preferred model (E1) this suggest that it would take at least 15 Ma after removal to increase surface heat flow to the observed magnitudes reported by Quintero et al. (2019) (e.g., 60-80 $\frac{mW}{m^2}$). Further heat flow data collection is required due to the large uncertainties in current available data.

- Upwelling of the sublithospheric mantle after lithosphere removal (by ~23 Ma in model E1) can produce decompression melting in the mantle and subsequent melting in the lower crust due to the increase in temperature. This means that evidence of lithosphere removal could be preserved in the magmatic rock record depending on its timing.

- Sublithospheric mantle upwelling after lithosphere removal (in model E1) can produce a low velocity anomaly of up to -5% for P-waves and -7.5% for S-waves, with minimum velocities of 7.6 and 4.1 km/s, respectively. This anomaly is located right under the Moho in the region that experienced removal which in the models is at about 38 km depth. This is close to the low shear seismic velocities reported by Poveda et al. (2018) at a depths between 30 to 35 km in the SNSM region (∼3.8 km/s).

- High lateral compression rates (>0.5 mm/yr but ≤1.5 mm/yr) reduce surface topography because they enhance plastic strain producing weak zones that promote subsidence, and they reduce the Bouguer gravity anomaly because they produce crustal thickening (∼6 km). Hence, low compression rates (≤0.5 mm/yr) favor the occurrence of a simultaneous high topography and Bouguer gravity anomaly, producing a better fit with the observations.

- When the initial crustal thickness is high (e.g., 40 km) the surface elevation is higher. Conversely, when the initial crustal thickness is low (e.g., 20 km) surface elevations are lower. The gravity anomaly is higher when the initial thickness is intermediate (e.g., 30 km) because when the crust is thicker, the gravity anomaly is lower, but at the same time there is more eclogitization and a larger portion of the lower crust is removed (i.e., greater increase in the gravity anomaly). Hence there is a better fit with the observations (high bouguer gravity anomaly and topography) at an intermediate initial crustal root thickness (30 km).

In principle, the load of the SNSM massif could be currently sustained by either support from the buoyant Caribbean slab, elastic stresses/flexural rigidity, or dynamic mantle upwelling. Evidence from seismic wave tomographies and the magmatic record suggest that lithosphere removal could have occurred either during the Paleocene-Eocene, possibly affecting regional magmatism, or very recently (in the last 2 Ma), potentially explaining a recent uplift episode.

For instance, the models show that lower-crustal and shallow sublithospheric mantle melts can be generated by decompression and subsequent heating after lithosphere removal. Consequently, if lithosphere removal occurred in the Eocene, it could explain why magmatism was localized, low-volume and short term (±10 Ma) (Duque-Trujillo et al., 2019), and why it does not correspond to typical Andean-type subduction magmatism.

However, the preferred interpretation is a more recent event (in the last 2 Ma) because the models show that the peak in the bouguer gravity anomaly after lithosphere removal is short-lived. This is supported by seismic wave tomographies in Poveda et al. (2018) which show low shear wave velocities ($\sim$3.8 km/s) at a depths between 30 to 35 km in the SNSM region. Because the models show that lithosphere removal produces surface subsidence, the associated non-isostatic forces can only produce uplift, explaining the recent uplift proposed by Villagómez et al. (2011), if forces that are not considered in the models contribute to the support of the massif (e.g., elastic strength, Caribbean-slab dynamics). In any case, the models presented demonstrate that a gravitational removal event is a viable explanation for many of the uncommon observations in the SNSM.

Chapter 6: Lithosphere Removal in 3D

6.1 Introduction

Early studies of lithosphere removal and drips triggered by convective instabilities used numerical and analytical solutions in 2D domains (e.g., Houseman et al., 1981; Houseman and Molnar, 1997; Neil and Houseman, 1999), even though many geological examples have a 3D nature (e.g., Arizaro Basin (DeCelles et al., 2015), Congo Basin (Downey & Gurnis, 2009)). More recent models have examined the effects of non-linear and temperature-dependent material properties (e.g., Currie et al., 2015; Göğüş and Pysklywec, 2008; Wang and Currie, 2017), but the majority of these studies have also been limited to 2D domains, owing to the high computational cost of 3D models, especially for complex, multi-layered systems. There have only been a few 3D studies of lithosphere drips, using numerical or analogue techniques (e.g., Houseman and Gemmer, 2007; Pysklywec and Cruden, 2004). These suggest that, relative to 2D drips, 3D lithosphere drips occur faster, produce greater topographic deflections, and may generate significant changes in crustal and surface deformation, such as an increase in the magnitudes of horizontal strain.

The region of study in this thesis is Sierra Nevada de Santa Marta (SNSM), which is a triangular-shaped mountain region that is separated from the rest of the Andes and is not oriented along a line, as is common for mountain ranges (Figure 1.1*a*). Consequently, this is a localized topographic feature where 3D effects may be important. The models in chapters 3, 4, and 5) examined drips in a 2D domain, which assumes no changes in the material model along strike. This chapter presents 3D models of lithosphere removal addressed to understand 3D dynamics, to constrain the differences between 2D and 3D drips, and to identify how 3D effects may affect the surface observables (surface topography, Bouguer gravity anomaly and surface heat flow).

For these models, it is assumed that the drip originates from a perturbation in the mantle lithosphere, and there is no previous episode of crustal thickening. This is an important difference from the models in the previous chapters that included crustal thickening and eclogitization. This choice was made in order to reduce the complexity and computational requirements of the models. With only a mantle lithosphere perturbation, the 3D model runs require 600 processors for more than 4 weeks. These models can therefore be used as the basis for future 3D models with both a crust and mantle lithosphere perturbation.

This chapter includes a comparison between two equivalent models only changing the modelling geometry (2D and 3D). Then, a series of 3D models explores the effects of crustal viscosity, lithospheric elasticity, and crustal viscoplastic rheology on the surface expressions of lithosphere drips. Analytic calculations (in 2D) by Neil and Houseman (1999) show that the crustal strength can modify the surface response, as a low-viscosity crust can undergo crustal contraction and uplift. The 3D models presented here examine whether this behaviour occurs for a 3D geometry. The models also test the effect of lithosphere elasticity, using an Earth-like shear modulus, in order to determine if it produces larger topographic deflections in a 3D geometry, as seen in the 2D models of Kaus and Becker (2007). Finally, plastic deformation is tested to identify if alterations to strain magnitudes induced by the 3D geometry, produce significant changes in the effect of plastic strain-weakening.

6.2 Modelling Setup

The modelling domain is a 3D box (Figure 6.1a) with a width (y) and length (x) of 800 km and a depth (z) of 660 km. The setup consists of an upper crust (20 km thick), lower crust (20 km thick), and mantle lithosphere (60 km thick); these overlie the sublithospheric mantle that extends to the base of the model. The upper 200 km of the domain have element sizes of 6.25 km in both horizontal directions and 5.16 km in the vertical direction. Below 200 km depth, the element size is 12.5 km in both horizontal directions and 10.3 km in the vertical direction.

The initial temperature conditions in the lithosphere use a conductive geotherm based on the assigned lithosphere thickness (100 km), with a surface heat flow of 53.6 $\frac{mW}{m^2}$, a thermal conductivity of 2.25 $\frac{W}{mK}$, an upper crustal heat production of $1.0 \times 10^{-6} \frac{W}{m^3}$, lower crustal heat production of $0.4 \times 10^{-6} \frac{W}{m^3}$ and no heat production in the mantle materials. The continental geotherm intersects a mantle adiabat with adiabatic gradient of 0.4 $\frac{K}{km}$, and temperature potential of 1573 K, at the base of the lithosphere (100 km).

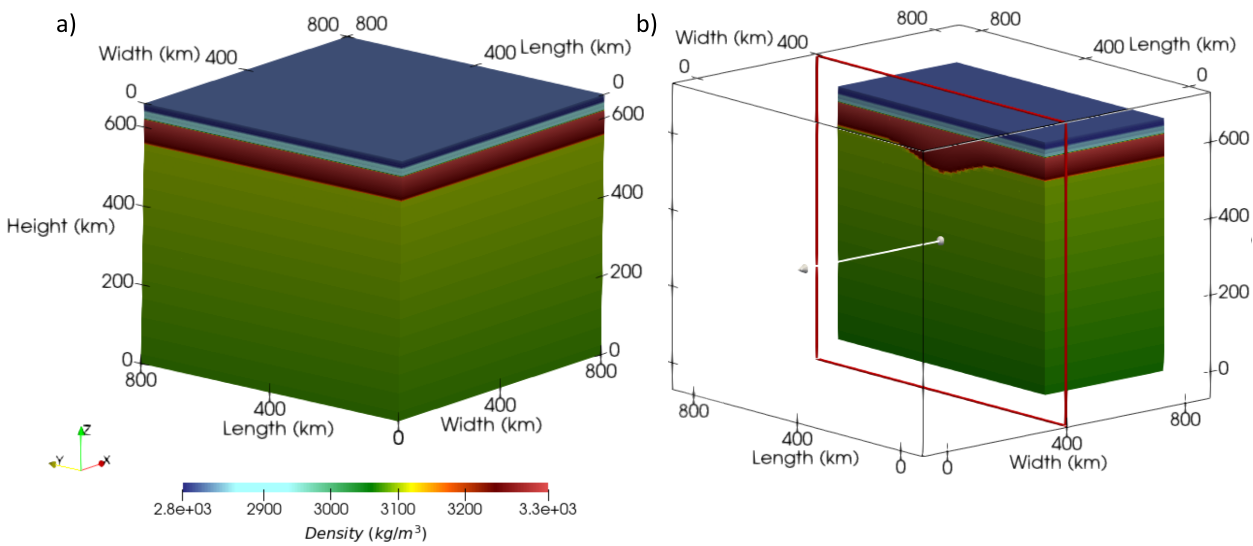

Figure 6.1: a) Density structure of the 3D modelling setup showing the full domain. b) Cross-section of the 3D density structure at a distance of 400 km along the y-axis. This shows the Gaussian-shaped mantle lithosphere perturbation with radial symmetry, centred in the middle of the domain (at x=400 km and y=400 km).

Figure 6.2 shows the detailed modelling structure along the slice at x=400 km, as indicated in Figure 6.1*b*. To initiate the drip, a region of thickened mantle lithosphere is placed in the middle of model, with its centre at the middle of the domain (at x=400 km and y = 400 km). The perturbation has a Gaussian shape (radial symmetry) with a half width of 200 km and amplitude of 50 km, as shown in Figure 6.1*b*. Within the perturbed region, the geotherm linearly stretched to match the increased thickness.

During the model run, the lateral boundary conditions (i.e., left, right, front and back sides) are free slip, the bottom boundary condition is no-slip (assuming coupling between the high-viscosity lower mantle and the upper mantle), and the top boundary has a free surface allowing for topographic deflections. The thermal boundary conditions use the initial temperature (Figure 6.2*c*) in all boundaries as fixed values in which the maximum temperature is of 1837 K (at a depth of 660 km), and the minimum temperature is of 273 K (at 0 km).

The material properties are given in tables 6.1, and 6.2. In the reference model, each layer has a constant viscosity, with values of 10^{25} $Pa \cdot s$, 10^{21} $Pa \cdot s$, and 10^{20} $Pa \cdot s$, for the whole crust, mantle lithosphere, and sublithospheric mantle, respectively. Later models examine variations in rheology, including a lower crustal viscosity, the inclusion of elasticity, and laboratory-based crustal viscoplastic rheologies (table 6.3).

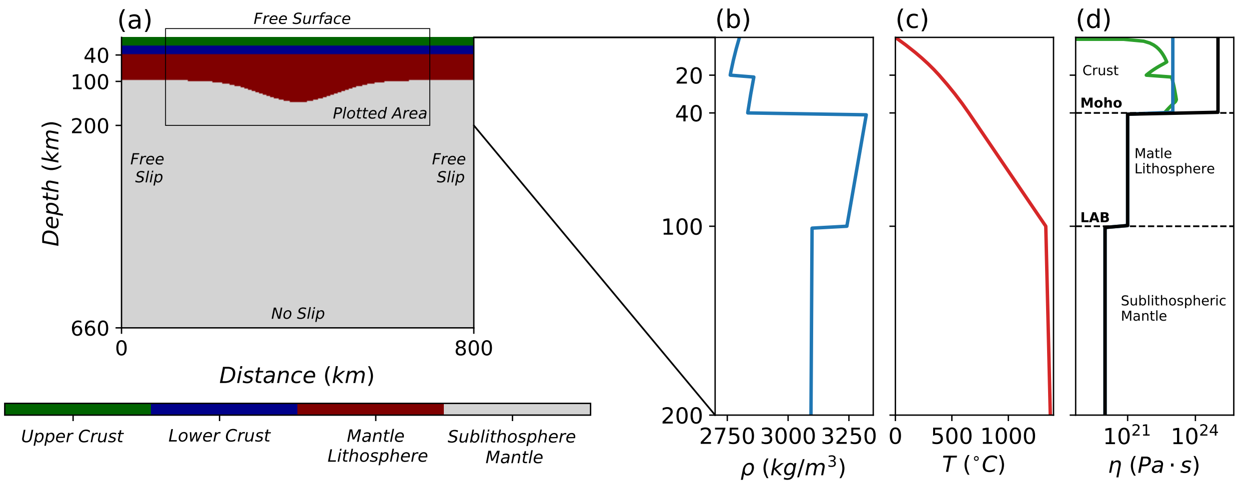

Figure 6.2: (a) 2D cross-section of the modelling set up for the 3D models, along the plane indicated in Figure 6.1*b*. (b) Density structure. (c) Initial temperature conditions. (d) Reference viscosity structure (black), crustal viscosity for model G3 (blue), and visco-plastic crustal rheology for model G5 at a constant strain rate of 1×10^{-15} s^{-1} (green), using wet quartzite (Gleason & Tullis, 1995) and dry Maryland diabase (Mackwell et al., 1998), for the upper and lower crust, respectively. Plots in a, b, and c show the non-perturbed initial structure at the sides of the instability. (Within the perturbed region, the continental geotherm is stretched in the mantle lithosphere instability keeping the LAB temperature constant)

Table 6.1: Material parameters for the models presented in this chapter.

Layer	**Reference Density** $(kg\ m^{-3})$	**Viscosity** $(Pa \cdot s)$	**Heat Production** $(W\ kg^{-1})$
Upper Crust	2800	1×10^{25}	3.57×10^{-10}
Lower Crust	2900	1×10^{25}	1.38×10^{-10}
Mantle lithosphere	3300	1×10^{21}	0.0
Sub-lithospheric Mantle	3250	1×10^{20}	0.0

Table 6.2: Common parameters used for all models.

Parameter	**Value**	**Units**
Specific heat (C_p)	1250	$J\ kg^{-1}\ K^{-1}$
Thermal conductivity (k)	2.25	$Wm^{-1}\ K^{-1}$
Thermal expansion coefficient (α)	3.5×10^{-5}	K^{-1}
Adiabatic gradient	0.4	$K\ km^{-1}$
Adiabatic temperature potential	1573	K

The density is temperature-dependent and uses a thermal expansion coefficient of $3.5 \times 10^{-5}\ \frac{1}{K}$. The reference densities of the upper crust, lower crust, mantle lithosphere, and sublithospheric mantle are 2800 kg/m^3, 2900 kg/m^3, 3300 kg/m^3 and 3250 kg/m^3, respectively. In contrast with models in the previous chapters of this thesis, the mantle lithosphere in these models has a higher reference density than the sublithospheric mantle, meaning that its gravitational instability is not only produced by its cooler temperatures, but is also generated by a compositional difference. This follows the approach used by Göğüş and Pysklywec (2008). While the compositional density difference between the mantle lithosphere and the rest of the upper mantle is a topic of discussion, its effect on drip dynamics is mostly important for the timescales of the instability growth. The purpose of these models is not to explore the timescales of lithosphere removal, but rather to study differences between 2D and 3D drips and the characteristics of crustal deformation in 3D geometries. Therefore, the higher reference density in the mantle lithosphere is used to promote lithosphere dripping and allow the drips to occur within 5 Ma, which decreases the computation time.

Table 6.3: List of models presented in this chapter with the corresponding parameter modifications with respect to the reference (setup in Figure 6.2).

Model	Parameter modification	Figure No.
Reference 2D		
G1	Reference setup in Figure 6.2	6.3*a*
Reference 3D		
G2	As G1 but 3D setup as in Figure 6.1, with radial symmetry	6.3*b*
3D Models		
G3	As G2 but crustal viscosity of $10^{23} Pa \cdot s$	6.7*a*
G4	As G2 but with lithosphere elasticity with shear modulus of $10^{10} Pa$	6.7*b*
G5	As G2 but with viscoplastic[a] crustal rheologies Upper crust: wet quartzite (Gleason & Tullis, 1995) Lower crust: dry Maryland diabase (Mackwell et al., 1998) Friction Angle: $15° - 2°$ Cohesion: $20 - 2$ MPa	6.7*c*

[a] The crust has viscoplastic rheologies with strain weakening when plastic strain changes from 0.5 to 1.5. This is applied by changing the friction angle and cohesion from 15°-2° and 20-2 MPa, respectively.

6.3 Results

6.3.1 2D vs. 3D Mantle Lithosphere Drips

This section compares 2D and 3D drips. Model G1 is the reference 2D model, which is setup to match the structure through the centre of the 3D models (i.e., the y=400 km slice in Figure 6.1*a*). Model G2 is the reference 3D model which has the full setup explained previously (Figures 6.1, and 6.2), which includes a 3D gravitational instability with radial symmetry. Both models use the same material parameters and boundary conditions.

Owing to the different model geometries, the 2D results are compared to a slice from the 3D models at $y = 400$ km (through the centre of the perturbation). The surface topography and heat flow are directly extracted from the 3D model along the top of this slice. The

Bouguer gravity anomaly from the 3D models corresponds to the anomaly produced by the 2D density structure of the $y = 400$ km slice, to compare to the equivalent anomaly in the 2D model.

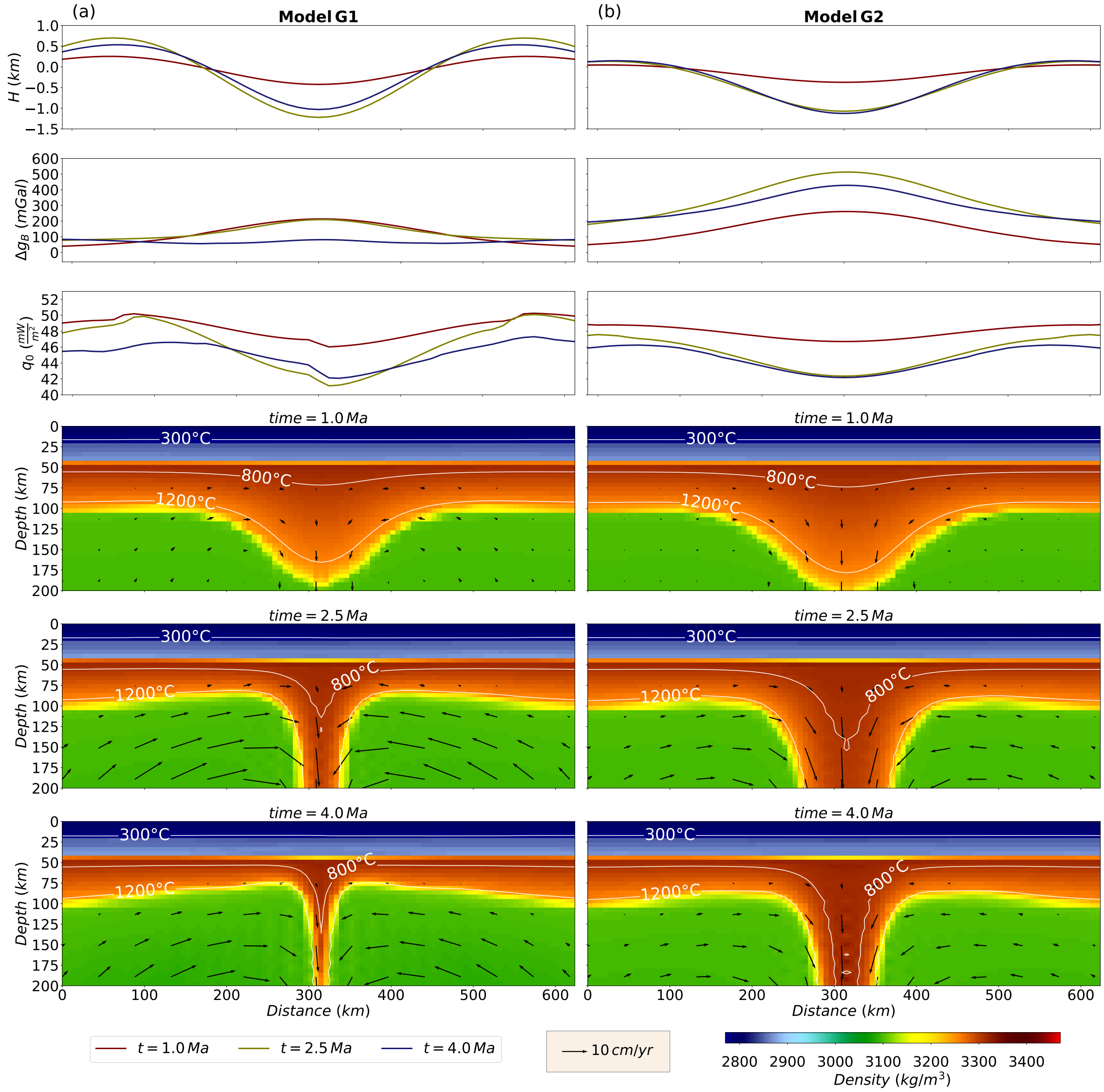

Figure 6.3: Modelling results for (a) 2D model G1, and (b) 3D model G2, including snapshots of density structures and profiles of surface topography (H), Bouguer gravity anomaly (Δg_B) and surface heat flow (q_0), at times before, during and after the main lithosphere removal episode. These models compare the results between a 2D and 3D drip.

The model evolution is shown in Figures 6.3, and 6.4. In both models, the high-density mantle lithosphere is gravitationally unstable and sinks in to the sublithospheric mantle. The 3D drip is slightly faster. For example, at 1 Ma, the drip is at a depth of ∼200 km in the 3D model, compared to ∼180 km in the 2D model. Because the model has constant viscosity materials, there is no drip detachment, and rather, the drip progressively sinks. Once it reaches the bottom of the model domain, it spreads towards the sides (Figure 6.5). As the drip sinks, some mantle lithosphere material is entrained from the sides and sinks at the centre. The drip thickness is reduced in time as the amount of entrained lateral material decreases.

The time evolution of surface observables of models G1 and G2 is shown in Figure 6.4. As expected, the gravitationally unstable mantle lithosphere produces subsidence above the drip and an increase in the Bouguer gravity anomaly, owing to the growing size of the high-density drip. The 2D drip (model G1) produces significantly more subsidence (maximum of 1.79 km vs 1.21 km), and a higher average subsidence rate (0.64 mm/yr vs 0.44 mm/yr). This is also evident in the topographic profiles in Figure 6.3, which show that subsidence in the centre is accompanied by uplift at the sides. This lateral uplift is larger in the 2D model (e.g., ∼0.6 km higher ridges at 2.5 Ma). In both models, there is subsidence until the drip reaches the bottom boundary, and then there is uplift due to the relaxation of the downward pull of the drip. Even though there is more subsidence in model G1, both models converge to the same surface elevation in the centre (about -800 m) after the post-drip uplift phase.

Another important difference between models G1 and G2 is that the 3D drip is always substantially thicker than the 2D drip (Figure 6.3). This is a consequence of the additional mantle lithosphere material in the 3rd dimension, as the surrounding material in all directions around the instability is entrained and pulled towards the drip. This likely contributed to the enhanced sinking rate in the 3D model. This also results in a significantly higher Bouguer gravity anomaly because of the accumulation of denser mantle lithosphere in the central region. The 3D model has a maximum gravity anomaly of +530 mGal, compared to a maximum of +250 mGal in the 2D model. Also, the increase in the Bouguer gravity anomaly persists for longer in the 3D model (G2) because at the end of the model run time (5 Ma) the anomaly in model G2 is still higher than its initial value, while in the 2D model (G1), the gravity anomaly descends below its initial value after only 2.9 Ma. Note that because the gravity calculations presented correspond to the 2D anomaly of a slice in the 3D domain of model G2 (at $y = 400$ km), the 3D gravity anomaly could be lower than reported.

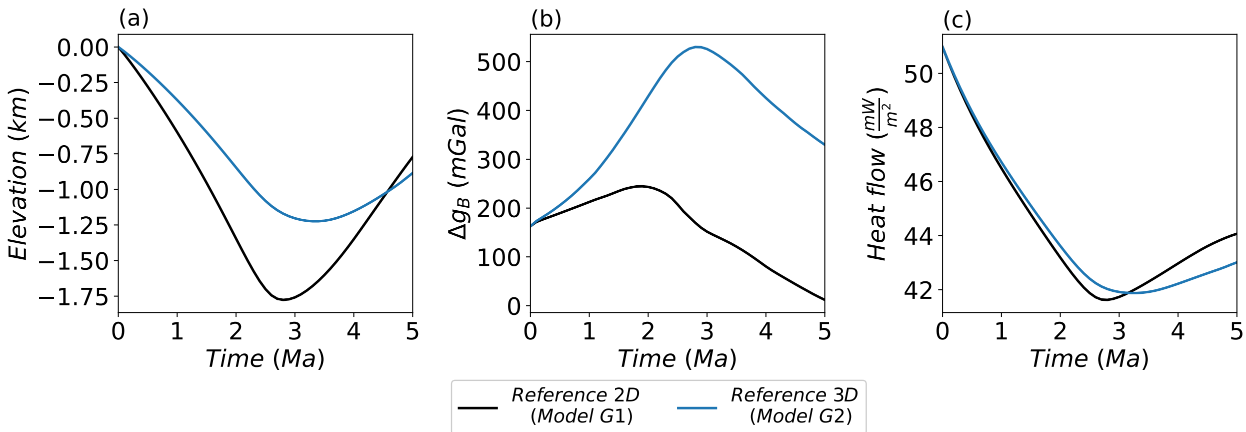

Figure 6.4: Time variation of surface observables averaged over a 50 km width centred over the mantle lithosphere instability, comparing the observables produced using a 2D and a 3D model geometry. (a) Surface topography. (b) Bouguer gravity anomaly (Δg_B). (c) Surface heat flow.

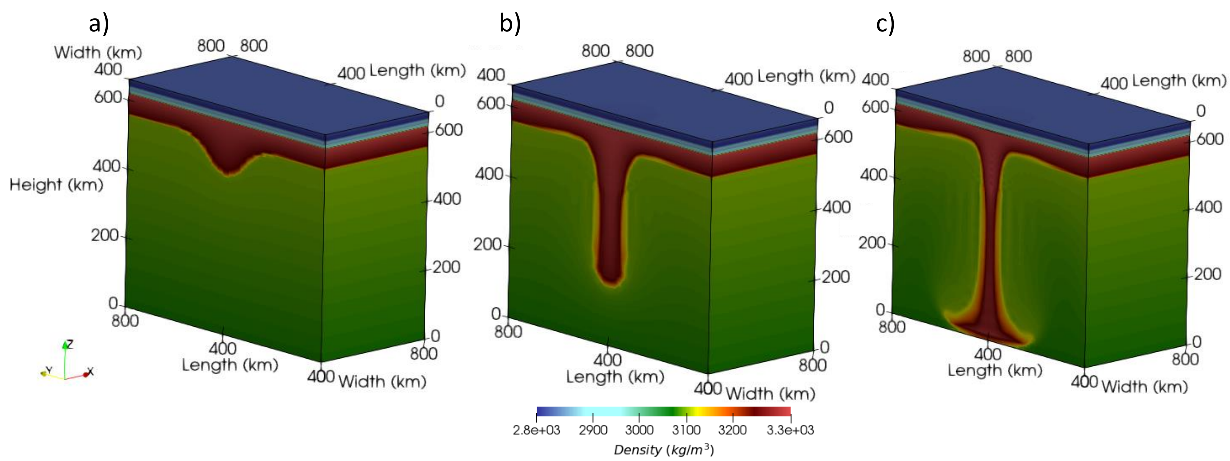

Figure 6.5: Cross-section at $y = 400$ km of the reference 3D model (G2) showing the full density structure at a model runtime of (a) 1 Ma, (b) 2.5 Ma, and (c) 4 Ma. Time (Ma) corresponds to the modelled time from the beginning to the end of the simulation.

The general behaviour of surface heat flow is different from the models of previous chapters. Models G1 and G2 show a fully viscous drip of the mantle lithosphere, where there is no removal of crustal material and the sublithosphere mantle does not contact the crust. Instead, the drip induces lithosphere thickening in the central region, leading to a decrease in surface heat flow of about 9 $\frac{mW}{m^2}$ in the first 2.5 Ma. However, as the tail of the drip and the mantle lithosphere in the central region get thinner, the sublithosphere mantle rises at the sides, and there is a progressive increase in surface heat flow. This behaviour is the same for both the 2D and 3D models, differing only in the magnitude of the final increase of surface heat flow (an increase of about 2.4 $\frac{mW}{m^2}$ in model G1, and 1.2 $\frac{mW}{m^2}$ in model G2, locally on top of the drip). The slightly lower value for the 3D model is produced because the drip is consistently thicker. The surface heat flow profiles in Figure 6.3*a* exhibit sharp steps in the sides and in the centre of model G1. These steps are a consequence of sharp deformation in the elements due to numerical errors. This steps produce a small fluctuation in temperature and result in a minor alteration in surface heat flow (<2 $\frac{mW}{m^2}$) which is negligible and does not produce any change in the dynamics of the model.

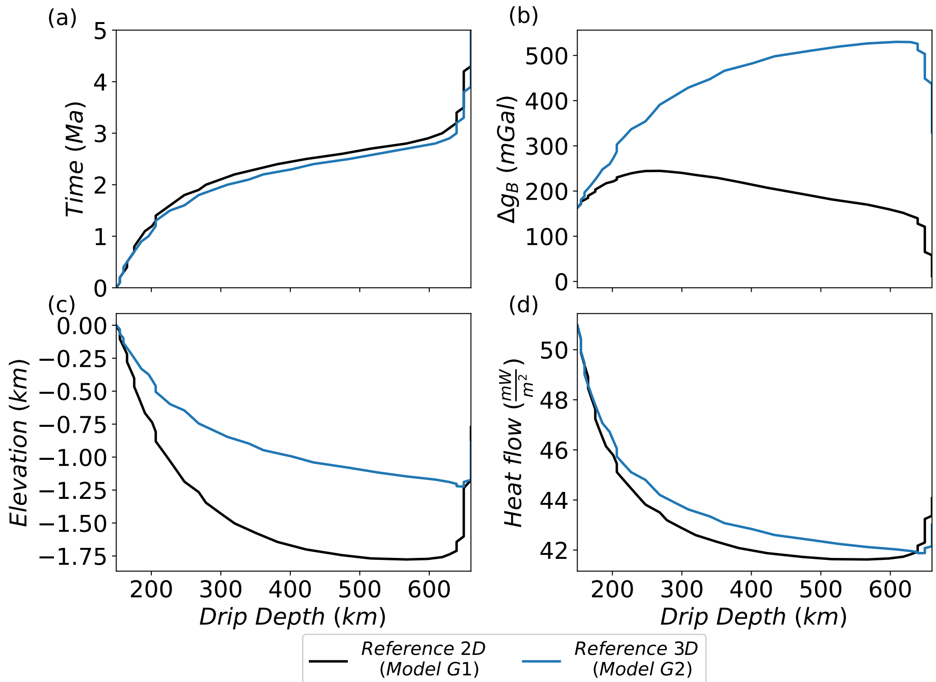

Figure 6.6: Variation of surface observables with drip depth, averaged over a 50 km width centred over the mantle lithosphere instability. The models presented show differences in the evolution of surface expressions between equivalent 2D and 3D models. a) Drip depth with time. This compares the instability growth between the models to identify if variations in the other observables are caused by differences in the timing of the dynamics. b) Bouguer gravity anomaly (Δg_B). c) Surface topography. d) Surface heat flow.

Figure 6.6 shows the evolution of surface observables as a function of drip depth in order to assess the effects of instability growth rates between 2D and 3D models. Figure 6.6*a*, confirms that the 3D drip is slightly faster, and it reaches the bottom boundary about 0.2 Ma earlier than the drip in the 2D model. However, Figures 6.6*b*-*d* show that the surface topography, gravity anomaly and surface heat flow exhibit significant differences when they are compared at same drip depths, demonstrating that the effect of the small change in drip velocity is not the main reason for the varying surface expressions . The difference in surface heat flow between the models is small (less than 1 $\frac{mW}{m^2}$), as discussed above . In contrast, there are significant differences in topography and the Bouguer gravity anomaly. For instance, when the drip reaches the bottom boundary there is a difference in elevation and gravity anomaly of 0.6 km and 370 mGal, respectively. These differences are a consequence of the 3D geometry. The Bouguer gravity anomaly is higher because the 3D drip is thicker as the amount of dense mantle lithosphere material is higher (in the central 2D slice at $y = 400$ km). The surface topography appears to be diminished in 3D because the drip is confined in a narrow region while the 2D drip assumes no variations in the material model along strike.

6.3.2 Variations in Lithosphere Rheology in 3D Models

This section examines modifications to the crustal rheology for the 3D model. Models G3, G4 and G5 have the same setup as the reference (model G2) with the parameter modifications indicated in table 6.3. In model G3, the crustal viscosity is reduced in 2 orders of magnitude (10^{23} $Pa \cdot s$). Model G4 includes lithosphere elasticity (including the crust and mantle lithosphere), with a shear modulus of 10^{10} Pa, following the formulation described in section 2.3.3. Because the relaxation time in Model G4 is about 32 Ma (crustal viscosity of 10^{25} Pa·s and shear modulus of 10^{10} Pa), which is large compared to the time scales of the model and the modelling elastic timestep ($\sim 10^{-3}$ Ma), the effective elastic viscosity is lower than the actual viscosity in almost 2 orders of magnitude ($\sim 3.1 \times 10^{23}$ Pa·s) (following equation 2.12). Model G5 uses a viscoplastic rheology in the crust, where the viscous rheologies follow the formulation described in section 2.3.1. These use the non-linear and temperature-dependent viscous rheologies of wet quartzite (Gleason & Tullis, 1995) and dry Maryland diabase (Mackwell et al., 1998) for the upper and lower crust, respectively. In this model plasticity is modelled using the Drucker Prager yield criterion which is described in section 2.3.2.

In all models , the gravitational instability of the mantle lithosphere grows into a wide drip that descends at approximately the same rate (Figure 6.7). Figure 6.8 shows the temporal variation in surface observables for models G3, G4, and G5. All models show subsidence above the drip, followed by uplift starting when the drip reaches the bottom boundary because there is relaxation of the drip-induced stresses. The final elevation in all the models is about -1 km. In addition, all models show an increase in Bouguer gravity anomaly, and a decrease in surface heat flow during the drip. The evolution of surface observables with drip depth is shown in Figure 6.9, in order to identify possible differences in the general behaviour before the time when the drip reaches the bottom. All models have a similar dripping rate (Figure 6.9*a*), but there are important differences in the surface observables, as discussed below.

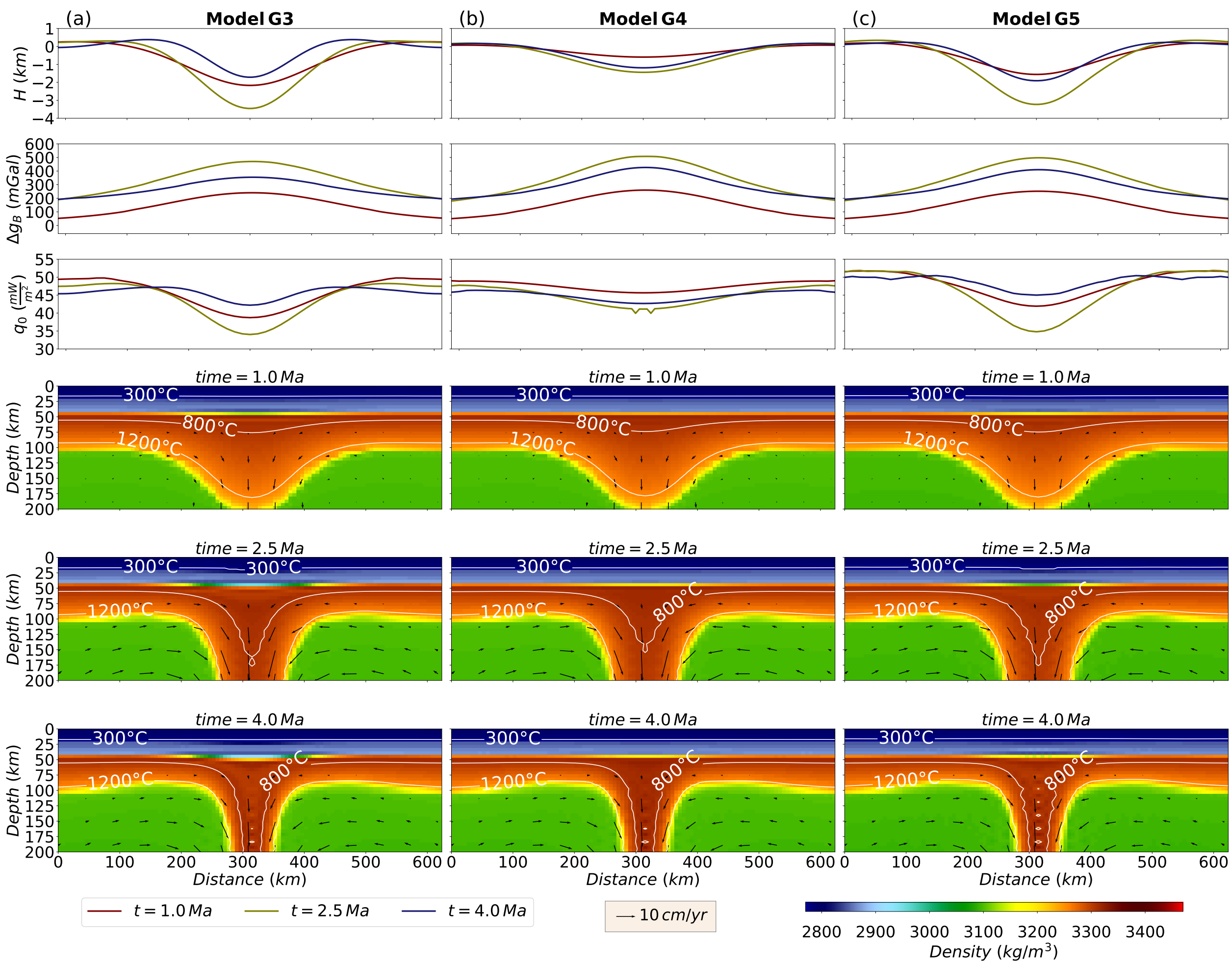

Figure 6.7: Modelling results for (a) model G3, (b) model G4, and (c) model G5, including snapshots of density structures and profiles of surface topography (H), Bouguer gravity anomaly (Δg_B) and surface heat flow (q_0), at times before, during and after the main lithosphere removal episode. Set G examines the behaviour of 3D lithosphere drips with different rheologies.

Model G3 uses a lower viscosity crust (10^{23} Pa s vs. 10^{25}Pa·s in the reference model). The reduction in crustal viscosity produces significantly more subsidence above the drip, resulting in a minimum elevation of -3.6 km (2.25 km lower than the reference). However, because the crust is weaker the lithospheric drip produces crustal contraction and thickening (∼5 km increase) and there is surface uplift induced by the isostatic response. Reduction of crustal viscosity also results in a lower Bouguer gravity anomaly (60-65 mGal lower after 3 Ma) (Figure 6.8*b*), which is also a consequence of the crustal contraction and thickening. The crustal thickening also affects the surface heat flow, which decreases to 33 $\frac{mW}{m^2}$ during the initial drip event. However, in the later stages of the model (after the drip reaches 400 km depth), the surface heat flow starts to increase, reaching 43 $\frac{mW}{m^2}$. This is likely a consequence of radiogenic heating within the thickened crustal layer, with a more abrupt increase after the drip reaches the bottom of the model.

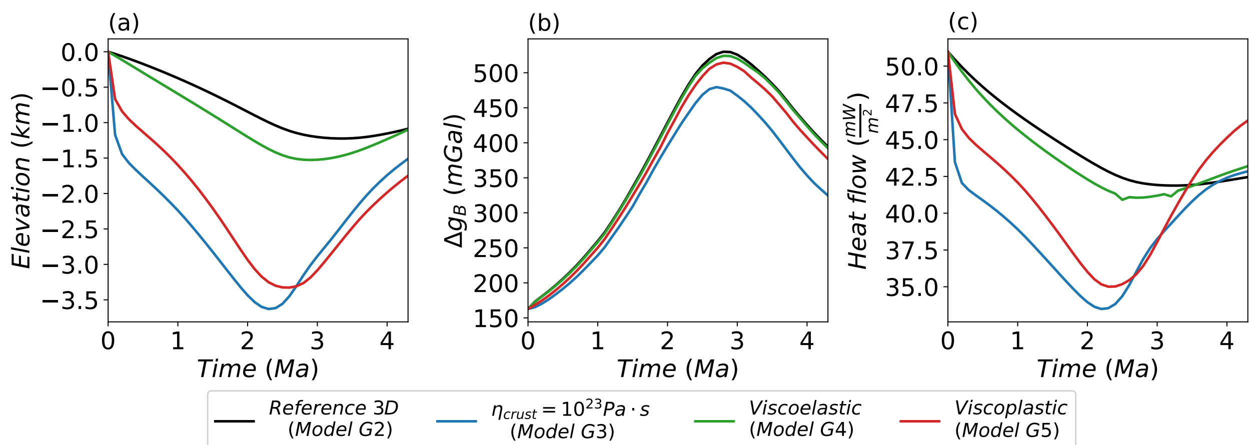

Figure 6.8: Time variation of surface observables averaged over a 50 km width centred over the mantle lithosphere instability, exploring the effect of crustal viscosity, elasticity and plasticity on surface expressions. (a) Surface topography. (b) Bouguer gravity anomaly (Δg_B). (c) Surface heat flow. Time (Ma) corresponds to the modelled time from the beginning to the end of the simulation.

Model G4 includes elasticity for all lithosphere materials. It exhibits slightly more subsidence than the reference model (the minimum elevation is 0.4 km lower). This is consistent with the behaviour reported by Kaus and Becker (2007) for 2D drip models with elasticity. The inclusion of elasticity produces no significant differences in the Bouguer gravity anomaly or surface heat flow compared to the reference model and has only a minor effect on the model results. The overall trends in surface observables are similar to those produced by the decrease in crustal viscosity (as in model G3) but with a lower magnitude. In the elastic model, the crust is weakened (the effective viscosity is lower than the actual viscosity, equation 2.12) and thus, crustal deformation is promoted. However, the elastic force tends to reverse deformation, producing an opposite effect. Consequently, the net effect of elasticity is analogous to a small weakening of the lithosphere.

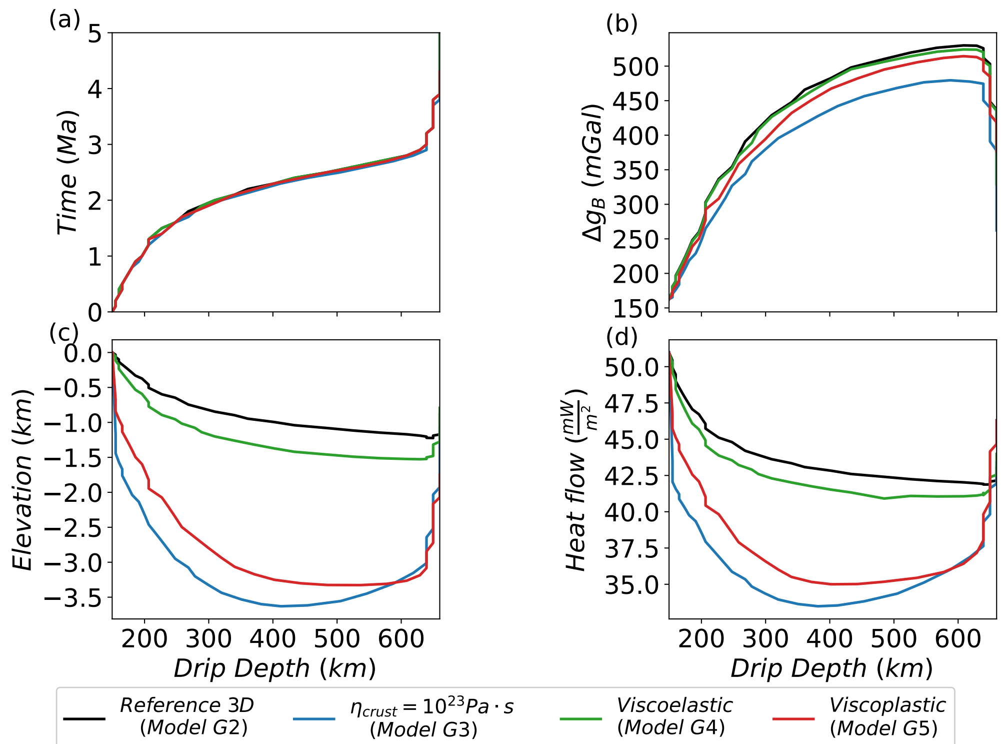

Figure 6.9: Variation of surface observables with drip depth, averaged over a 50 km width centred over the mantle lithosphere instability. The models included show the effect of viscous, elastic and plastic lithosphere deformation in 3D models. a) Drip depth with time. This compares the instability growth velocity between the models to identify if variations in the other observables is caused by alterations in the timing of the dynamics. b) Bouguer gravity anomaly (Δg_B). c) Surface topography d) Surface heat flow.

Model G5 uses a viscoplastic rheology in the crust, and constant viscosities in the mantle lithosphere and sublithospheric mantle. Because the resultant effective viscosity in the crust of this model is close to the viscosity in model G3 (i.e., 10^{23} Pa·s) (Figure 6.2*d*), the general behaviour of the surface observables of topography, Bouguer gravity anomaly and surface heat flow resembles the behaviour in model G3. The main differences are that in model G5 there is less surface subsidence associated to the drip resulting in a minimum elevation of -3.3 km (0.3 km higher than in G5), and that there is not significant crustal thickening. The reason for these differences is that the viscosity of the lower crust in model G5 is higher than in model G3, resulting from the viscous rheology of dry Maryland diabase (Mackwell et al.,

1998) and the plastic yielding criterion. Figures 6.9*b*-*d* show that compared to the results of model G3, the latter also results in a higher Bouguer gravity anomaly (e.g., ∼35 mGal higher when the drip reaches the bottom), absence of uplift before the drip reaches the bottom, and a higher surface heat flow by less than 2 $\frac{mW}{m^2}$. Even though model G5 accounts for plasticity and strain is focused on the weaker shallow crust, there is not observable brittle deformation in the model surface.

6.4 Discussion

The models in this chapter show that a 3D lithosphere drip descends more quickly than a 2D drip (full descent occurs between 0.1 to 0.2 Ma earlier) and the drip itself is wider because material can be pulled to the centre from all radial directions, rather than limited to a 2D plane. The difference in decent speed is caused by the additional negative buoyancy in the 3D drips as more mantle lithosphere material is pulled to the central region. Also, in a 3D geometry there is less resistance to the mantle lithosphere decent because the drip is localized while in 2D there is an infinitely long mantle lithosphere sheet (along 1 dimension) which lies perpendicularly to the descent direction.

This leads to differences in the surface expressions, where 3D drips produce reduced subsidence and higher 2D Bouguer gravity anomalies (in a single 2D cross-section). While the difference in the gravity anomaly along a 2D section is caused by the width of the drip (i.e., amount of dense mantle lithosphere material dripping), 3D drips produce less topographic deflections because they occur in a localized region and therefore the downward vertical stresses are largest right on top of the drip but decrease radially.

The weak crust in Model G3 shows that the crustal viscosity significantly affects the topographic evolution because there is significant uplift before the drip reaches the bottom (Figure 6.9*c* after a drip depth of 400 km). Whereas models G2, G4, and G5 exhibit no significant change in the thickness of the crust, the weaker crust in model G3 undergoes deformation and thickens by up to 4 km. The thickening of the low-density crust appears to be the main cause of the observed uplift; there may also be an additional contribution from relaxation of the downward pull of the drip once the drip reached the deep mantle. The crustal thickening is consistent with the results reported by Neil and Houseman (1999) for models with a weak crust.

Model G4 shows that the inclusion of elasticity has only a minor effect on the model evolution. Because the relaxation time for model G4 is of about 32 Ma and the elastic modelling timestep is of about 10^{-3} Ma, the crustal elastic effective viscosity is close to 3×10^{23} Pa·s (equation 2.12), which is very similar to the crustal viscosity in model G3 (10^{23} Pa·s). However, the evolution of surface observables of model G4 resembles more the evolution of model G2, which has a higher viscosity by almost 2 orders of magnitude. This shows that the contribution of elastic strength is very significant and can restrict deformation considerably even if the rheology of the lithosphere is relatively weak.

The behaviour of surface observables in model G5 is very similar to the behaviour in model G3 because the crustal viscoplastic rheologies (in model G5) result in an effective viscosity that is close to the constant viscosity of model G3 (10^{23} Pa·s). However, since the lower crust in model G5 is stronger and strain is focused in weak (and shallow) regions, there is not significant crustal thickening. Results suggest that the strain induced by a lithosphere removal episode is not sufficient to produce brittle deformation in the shallow crust. These results are significantly influenced by the plastic parameters (i.e., friction angle, cohesion, strain weakening) used in the model. Thus, further work is required to understand the extent of brittle deformation associated to lithosphere removal in a 3D model geometry.

The main motivation for the models in this chapter is to explore whether 3D effects may be important for the SNSM region. The implications of the Bouguer gravity anomaly comparisons between 2D and 3D models are not clear. On one hand, if the amount of mantle lithosphere material pulled is larger (as suggested in a 3D geometry), the Bouguer gravity anomaly produced by the drip could be higher (closer to the observations). On the other hand, since in a 3D geometry the drip is confined and localized, the full 3D Bouguer gravity anomaly could be lower than the estimated in calculations using a 2D section. Future work is necessary to quantify the Bouguer gravity anomaly magnitudes associated to lithosphere removal in a 3D geometry. Model G3 shows that drips can induce crustal contraction and thickening, resulting in surface uplift above a drip. This may have important implications for the SNSM, where high topography is observed. Further, as the crust thickens, the deep part of the crust may undergo eclogitization. This would enhance the removal process, resulting in a thin crust and lithosphere, as seen in the models in Chapter 5. This would depend on the trade off produced by crustal thickening between uplift and the Bouguer gravity anomaly. For instance, even if crustal thickening results in uplift, if the crustal root is not fully eclogitized and removed, it would result in a decrease in the Bouguer gravity anomaly. Additionally, model G2 shows that in a 3D geometry there is less drip-induced subsidence and a lower subsidence rate because drips are confined in a localized and narrow region. This may also be important for the SNSM because slower subsidence after removal would facilitate the coexistence between a high Bouguer gravity anomaly and high elevations. Future 3D models should examine a wider range of crustal viscosities and densities, including the effects of eclogitization and an initial thickening of the crust in the perturbed region.

6.5 Summary and Conclusions

The models presented in this chapter explore the effects of lithosphere drips in 3D, and the associated surface topography, Bouguer gravity anomaly and surface heat flow. By comparison with an equivalent 2D model, it is possible to distinguish effects that are directly produced by the change in modelling geometry from indirect effects resulting from different growth rates of the convective instabilities. Additionally, the set of 3D models (G3, G4 and G5) shows how the rheology of the crust alter the surface observables in 3D. These provide valuable insights into the interpretation of geological/geophysical observations in regions where a localized drip (with approximately radial symmetry) has been proposed, such as the elevated region of the SNSM, or even topographic depressions, such as the Arizaro and Congo basins. The main conclusions are:

- For the parameters considered in these models, the rate of growth of a mantle lithosphere instability is slightly larger in a 3D model compared to a 2D model (full descent occurs between 0.1 and 0.2 Ma earlier). The 3D drip is considerably thicker as it can draw in material in the radial directions. Within a 2D plane, this results in a significantly higher Bouguer gravity anomaly (280 mGal higher, or increased by 112%), due to the accumulation of more dense mantle lithosphere material in the central region.

Also, in the 3D model, the downward stresses from the drip are localized in the centre but decrease in all directions. This results in a lower amount of subsidence above the drip (there is 0.5 km of less subsidence, or it is reduced by 66%).

- When crustal viscosity is reduced in 2 orders of magnitude, maximum subsidence increases by 2.25 km, the maximum Bouguer gravity anomaly is 63 mGal lower, surface heat flow is 10 $\frac{mW}{m^2}$ lower. These differences are primarily because the vertical stresses from the drip create contraction and thickening of the overlying crust (up to 4 km). The progressive crustal thickening triggers an isostatic response which results in uplift prior to the relaxation of the downward stresses of the drip (which occurs when the drip reaches the bottom boundary). In this case, the isostatic response is not enough to fully invert the low elevation region to produce a mountain, but future work to explore the full range of topographic expressions in 3D is recommended.

- The general effect of elasticity is equivalent to a weakening of the lithosphere, as elasticity results in a reduced effective viscosity. However, elastic stresses also provide additional support to limit topographic changes. As a result, the inclusion of elasticity allows for 0.4 km more subsidence, but only minor changes in Bouguer gravity anomaly and surface heat flow.

- The use of viscoplastic rheologies in the crust results in a lower effective viscosity compared to the reference model (G2). Hence, the general behaviour of surface observables is analogue to the behaviour when crustal viscosity is lower, but with no significant crustal thickening due to the strong lower crustal rheology. This is, more surface subsidence (minimum elevation of $\sim$3.3 km), slightly lower Bouguer gravity anomaly (about 10 mGal lower than the reference), and a lower surface heat flow (minimum value of $\sim$35 $\frac{mW}{m^2}$). In the model presented drip dynamics is not sufficient to produce significant brittle shallow deformation.

- Because 3D drips tend to produce less subsidence and can allow for syn-drip uplift if the crust is weak, future work should extend these models to assess the conditions needed to explain the observations in the SNSM (e.g., high elevation of 4 to 5 km and a gravity anomaly above +130 mGal). The 3D models show that the surface subsidence rate is lower above a 3D drip and the high gravity anomalies persist for longer. Overall, the 3D models suggest that a drip can have an observable effect on the Earth's surface and provide additional support for the hypothesis that the SNSM may be associated with a gravitational removal event.

Chapter 7: Conclusions

7.1 Concluding Remarks

Gravitational removal of the deep lithosphere has been proposed to have occurred in a number of regions, including the Sierra Nevada California, the Altiplano-Puna Plateau and the Western Canadian Cordillera (e.g., Bao et al., 2014; Beck and Zandt, 2002; Saleeby et al., 2012). Early studies provided analytical solutions for gravitational instabilities using Earth-like parameters showing that lithosphere removal is expected due to the thermal structure of the Earth, whereby the cool mantle lithosphere temperatures result in a higher density than the underlying mantle (e.g., Houseman et al., 1981). More recent studies show that removal can also be induced if the lower crust has a high density due to the presence of eclogite (e.g., Jull and Kelemen, 2001). Lithosphere removal is characterized by a coupled interaction between the lithosphere and the upper mantle, and it is considered to produce observable effects on the Earth's surface. However, it is challenging to obtain physical evidence for this process because most of the deformation occurs at depth. Hence, current studies of lithosphere removal commonly use evidence from indirect geophysical measurements and geodynamic numerical models, instead of traditional geological approaches. The use of models presents the challenge of defining simplified, but geologically reasonable, modelling scenarios that capture the underlying physics, using multiple parameters which are often poorly constrained.

This thesis addresses the hypothesis that a lithosphere removal event occurred in northern Colombia, South America, and that this is responsible for the current surface expressions in the Sierra de Nevada Santa Marta (SMSM). The SNSM is an unusual triangular-shaped region of high topography, which exhibits surface elevations of up to 5.7 km and a positive Bouguer gravity anomaly above +130 mGal. The SNSM is separated from the Andes

Cordillera, it is surrounded by large faults and is constituted by multiple igneous bodies that record previous continental magmatism (e.g., Cardona et al., 2010; Duque-Trujillo et al., 2019; Ramírez et al., 2020). As well, this region has been affected by the diachronous collision of the Caribbean plate with north-western South America, and its history is part of the complex tectonic evolution in the Caribbean (e.g., Bayona et al., 2011; Spikings et al., 2015). Despite numerous studies to understand the tectonics, magmatic episodes, and the associated styles of deformation (e.g., Cardona et al., 2010; Cardona et al., 2011a; Cardona et al., 2011b; Duque-Trujillo et al., 2019; Montes et al., 2010; Ramírez et al., 2020; Villagómez et al., 2011), the origin of the SNSM remains enigmatic.

This work uses numerical models to examine the dynamics of lithosphere removal and the associated surface expressions. It includes a set of careful and exhaustive parameter tests used to formulate suitable models of lithosphere removal for the SNSM region. This constitutes a systematic study of both the numerical-computational and geological-physical implications of lithosphere removal. In both cases, results in this work provide general insights that are valuable for geosciences, geodynamic modelling, studies of lithosphere removal, and the study of the SNSM.

The models show that lithosphere and upper mantle dynamics during lithosphere removal are strongly affected by the rheological structure, clearly affecting the deformation timescales (which tend to be longer with stronger rheologies and *vice-versa*) and the magnitudes of surface expressions (e.g., surface topography, Bouguer gravity anomaly, and surface heat flow). Moreover, different rheological structures can produce different dynamics, such as lithosphere dripping or delamination (e.g., delamination is induced with weak lower crustal rheologies and creates removal over a wider area). Consequently, the models presented are applicable to multiple geologic settings. The dynamics are also dramatically affected if the material models account for plasticity and elasticity, in addition to viscous flows. Plasticity (i.e., frictional-plastic deformation) produces substantial shallow deformation and a reduction of drip-induced surface uplift, whereas elasticity can weaken the crust, producing simultaneous elastic support and accounting for reversible deformation. Hence, the use of full viscoplastic or viscoelastoplastic material models is crucial to produce realistic predictions of the surface expressions of lithosphere removal.

On the basis of the models in this thesis, it is concluded that lithosphere removal in the SNSM region is a feasible explanation for the topography and Bouguer gravity observations. The preferred 2D model shows that lithosphere dripping, induced by both an eclogitized lower crust and a mantle lithosphere perturbation, can occur on timescales of 25 Ma. This results in full crustal root removal and the development of a high-elevation mountain region (~3.3 km elevation) with a positive Bouguer gravity anomaly (~100 mGal). The conditions of the preferred model show that a rheologically strong lower crust provides more support for the load of the topographies and that a locally wet (and rheologically weaker) mantle lithosphere reduces the dripping timescales such that there is less subsidence at the time of full crustal root removal. The latter rheological configuration is compatible with the observations in the SNSM because it facilitates the coexistence of a high Bouguer gravity anomaly and a high topography. An important result from the models is that the high elevation is supported by non-isostatic forces, including mantle upwelling and lateral lithosphere strength. On the other hand, 3D models show that a radially symmetric drip is wider and descends at a slightly higher speed. This can produce up to 66% less subsidence, compared to an equivalent 2D drip, suggesting that the topography in the 2D models of Chapter 5 could be closer to the observations (>5 km) if the models are extended to 3D. These model predictions are compatible with observations from the SNSM. Using the 2D numerical models, it is proposed that a removal event occurred either in the Eocene (~40 Ma ago) or in the last 2 Ma. The recent event is the preferred time because the preferred 2D models suggest that lithosphere removal produces a short-lived peak in the Bouguer gravity anomaly with values around +100 mGal, which last for ~1.5-2 Ma.

This thesis presents the first detailed numerical models of the geodynamics in northern Colombia, the Caribbean, and the SNSM. The models focus on continental lithosphere dynamics, exploring lithosphere removal as a possible explanation for the SNSM. The models provide quantitative predictions of seismic wave velocities and melt production patterns, in addition to the surface topography, Bouguer gravity anomaly, and surface heat flow. These predictions provide valuable constraints for the evolution of the SNSM and its surrounding basins, which can be applied to hydrocarbon exploration/modelling (e.g., thermal structure, stress variations). As well, the models show that lithosphere removal may induce deformation within the crust. Future geological and geophysical studies can use these predictions to further examine the possibility of lithosphere removal in the SNSM and place stronger constraints on its timing and spatial extent.

7.2 Future Work

An important limitation in the 2D models of the SNSM (chapter 5) is the absence of elastic behaviour in the numerical formulation. This is important because the high elastic thickness and relatively narrow width of the massif mean that elastic stresses may contribute significantly to the support of the mountain. The 3D models of simple drips using elasticity (chapter 6) suggest that the inclusion of elasticity is equivalent to a slight weakening of the lithosphere, it is still necessary to better quantify its effect for the scenario of complete removal of a crustal root. One possibility is that the elastic strength of the crust could provide additional support to maintain the high topography of the mountain, even in the absence of a thick crustal root. If elastic support is sufficient to hold the load of the massif, the mantle dynamics can possibly result in post-removal uplift. In this case, lithosphere removal could potentially explain the recent uplift episode (in the last 2 Ma) suggested by Villagómez et al. (2011).

It should also be noted that the approach for lower crustal eclogitization in the 2D models (Chapters 4 and 5) is simplified. It assumes that there is enough hydration in the crustal root to induce a rapid phase change compared to the timescales of the models. Crustal root densification is a complex process, and there is little constrain on its rate due to its dependence on water content and rock composition (e.g., Ahrens and Schubert, 1975; Austrheim et al., 1997). Therefore, the time required for eclogitization and complete crustal root removal is uncertain, but the models show that this process is an important driver of lithosphere removal.

The models in this thesis focus on the dynamics of the continental lithosphere, assuming an initial lithosphere structure in the region of the mountain prior to the onset of lithosphere removal, including the amplitude of the crustal root and initial topography. Models in Chapter 5 show that when the crust is initially thicker, lithosphere removal is faster, subsidence rates are larger, and post-drip equilibration gravity anomalies are lower. The initial structure in the SNSM region is uncertain, but more detailed geological studies, as well as the temporal changes in the surface topography and magmatism may provide constraints for future models. As well, future models should address the effects of interactions between the Caribbean Plate and South America in more detail. Convergence between the two plates throughout the Late Cretaceous – Early Paleogene may have created compression and shortening in the region of the SNSM, and present-day subduction of the Caribbean Plate may affect the dynamics of the lithosphere drip.

Another important limitation is the 2D nature of the SNSM models in Chapters 4 and 5. The SNSM mountain region has an approximately radial symmetry and ideally, it should be studied in a 3D geometry. Models in chapter 6 show that simple 3D drips tend to produce significantly less subsidence, lower subsidence rates, and higher Bouguer gravity anomalies, with smaller differences in instability growth rate and dripping timescales. Future work should verify if the latter holds for more complex 3D models of the SNSM that include fully visco-elasto-plastic rheologies and crustal root eclogitization. This is important because the combination of geologically-realistic rheologies and 3D effects can potentially facilitate the coexistence of high Bouguer gravity anomalies, elevated regions, and high surface heat flow, such as in the region of the SNSM.

References

Ahrens, T. J., & Schubert, G. (1975). Gabbro-eclogite reaction rate and its geophysical significance. *Reviews of Geophysics*, *13*(2), 383–400. https://doi.org/10.1029/RG013i002p00383

Annen, C., & Sparks, R. S. (2002). Effects of repetitive emplacement of basaltic intrusions on thermal evolution and melt generation in the crust. *Earth and Planetary Science Letters*, *203*(3-4), 937–955. https://doi.org/10.1016/S0012-821X(02)00929-9

Arnaiz-Rodríguez, M. S., & Audemard, F. (2014). Variations in elastic thickness and flexure of the Maracaibo block. *Journal of South American Earth Sciences*, *56*, 251–264. https://doi.org/10.1016/j.jsames.2014.09.014

Austrheim, H. (1987). Eclogitization of lower crustal granulites by fluid migration through shear zones. *Earth and Planetary Science Letters*, *81*(2-3), 221–232.

Austrheim, H., Erambert, M., & Engvik, A. K. (1997). Processing of crust in the root of the Caledonian continental collision zone: The role of eclogitization. *Tectonophysics*, *273*(1-2), 129–153. https://doi.org/10.1016/S0040-1951(96)00291-0

Bangerth, W., Dannberg, J., Gassmoeller, R., & Heister, T. (2020a). ASPECT v2.2.0. Zenodo. https://doi.org/https://doi.org/10.5281/ZENODO.3924604

Bangerth, W., Dannberg, J., Gassmoeller, R., Heister, T., Et al. (2020b). ASPECT: Advanced Solver for Problems in Earth's ConvecTion, User Manual. https://doi.org/https://doi.org/10.6084/m9.figshare.4865333

Bao, X., Eaton, D. W., & Guest, B. (2014). Plateau uplift in western Canada caused by lithospheric delamination along a craton edge. *Nature Geoscience*, *7*(11), 830–833. https://doi.org/10.1038/ngeo2270

Bayona, G., Montes, C., Cardona, A., Jaramillo, C., Ojeda, G., Valencia, V., & Ayala-Calvo, C. (2011). Intraplate subsidence and basin filling adjacent to an oceanic arc–continent collision: A case from the southern caribbean-south america plate margin. *Basin Research*, *23*(4), 403–422.

Beaumont, C., Jamieson, R., & Nguyen, M. (2010). Models of large, hot orogens containing a collage of reworked and accreted terranes. *Canadian Journal of Earth Sciences*, *47*(4), 485–515.

Beck, S. L., & Zandt, G. (2002). The nature of orogenic crust in the central Andes. *Journal of Geophysical Research: Solid Earth*, *107*(B10), ESE 7–1–ESE 7–16. https://doi.org/10.1029/2000jb000124

Burov, E., & Watts, A. (2006). The long-term strength of continental lithosphere:" jelly sandwich" or" crème brûlée"? *GSA today*, *16*(1), 4.

Cardona, A., Valencia, V. A., Bayona, G., Duque, J., Ducea, M., Gehrels, G., Jaramillo, C., Montes, C., Ojeda, G., & Ruiz, J. (2010). Early-subduction-related orogeny in the northern Andes : Turonian to Eocene magmatic and provenance record in the Santa Marta Massif and Rancheria Basin , northern Colombia. *Terra Nova*, *23*(1), 26–34. https://doi.org/10.1111/j.1365-3121.2010.00979.x

Cardona, A., Valencia, V., Weber, M., Duque, J., Montes, C., Ojeda, G., Reiners, P., Domanik, K., Nicolescu, S., & Villagomez, D. (2011a). Transient Cenozoic tectonic stages in the southern margin of the Caribbean plate: U-Th/He thermochronological constraints from Eocene plutonic rocks in the Santa Marta massif and Serranía de Jarara, northern Colombia. *Geologica Acta*, *9*(3-4), 445–469. https://doi.org/10.1344/105.00000

Cardona, A., Weber, M., Duque, J., Montes, C., Ojeda, G., Reiners, P., Domanik, K., Nicolescu, S., & Villagomez, D. (2011b). Transient Cenozoic tectonic stages in the southern margin of the Caribbean plate: U-Th/He thermochronological constraints from Eocene plutonic rocks in the Santa Marta massif and Serranía de Jarara, northern Colombia. *Geologica Acta*, *9*(3-4), 1–12. https://doi.org/10.1344/105.00000

Case, I. E., & Macdonald, W. D. (1973). Regional gravity anomalies and crustal structure in Northern Colombia. *Bulletin of the Geological Society of America*, *84*(9), 2905–2916. https://doi.org/10.1130/0016-7606(1973)84⟨2905:RGAACS⟩2.0.CO;2

Ceron-Abril, J. F. (2008). *Crustal structure of the Colombian Caribbean Basin and margins.* (PhD). University of South Carolina.

Connolly, J. A. (2005). Computation of phase equilibria by linear programming: A tool for geodynamic modeling and its application to subduction zone decarbonation. *Earth and Planetary Science Letters*, *236*(1-2), 524–541. https://doi.org/10.1016/j.epsl.2005.04.033

Cornthwaite, J., Bezada, M. J., Miao, W., Schmitz, M., Prieto, G. A., Dionicio, V., Niu, F., & Levander, A. (2021). Caribbean slab segmentation beneath northwest south america revealed by 3-d finite frequency teleseismic p-wave tomography. *Geochemistry, Geophysics, Geosystems*, *22*(4), e2020GC009431.

Currie, C. A., & van Wijk, J. (2016). How craton margins are preserved: Insights from geodynamic models. *Journal of Geodynamics*, *100*, 144–158.

Currie, C. A., Ducea, M. N., DeCelles, P. G., Beaumont, C., Carrapa, B., & Kapp, P. (2015). Geodynamic models of cordilleran orogens: Gravitational instability of magmatic arc roots. *Geological Society of America Memoirs*, *212*, 1–22.

DeCelles, P. G., Carrapa, B., Horton, B., McNabb, J., Gehrels, G. E., Boyd, J., Et al. (2015). The miocene arizaro basin, central andean hinterland: Response to partial lithosphere removal. *Geol. Soc. Am. Mem*, *212*, 359–386.

Downey, N. J., & Gurnis, M. (2009). Instantaneous dynamics of the cratonic congo basin. *Journal of Geophysical Research: Solid Earth*, *114*(B6).

Ducea, M. N., Chapman, A. D., Bowman, E., & Triantafyllou, A. (2021a). Arclogites and their role in continental evolution; part 1: Background, locations, petrography, geochemistry, chronology and thermobarometry. *Earth-Science Reviews*, *214*(March 2021), 103375. https://doi.org/10.1016/j.earscirev.2020.103375

Ducea, M. N., Chapman, A. D., Bowman, E., & Balica, C. (2021b). Arclogites and their role in continental evolution; part 2: Relationship to batholiths and volcanoes, density and foundering, remelting and long-term storage in the mantle. *Earth-Science Reviews*, *214*(March 2021), 103476. https://doi.org/10.1016/j.earscirev.2020.103476

Duque-Trujillo, J. F., Orozco-Esquivel, T., Sánchez, C. J., & Cárdenas-Rozo, A. L. (2019). Paleogene magmatism of the Maracaibo Block and its tectonic significance. In F. Cediel & R. Shaw (Eds.), *Frontiers in earth sciences* (pp. 551–601). Medellín, Springer, Cham. https://doi.org/10.1007/978-3-319-76132-9_7

Elkins-Tanton, L. T. (2005). Continental magmatism caused by lithospheric delamination. *Special Paper of the Geological Society of America*, *388*(27), 449–461. https://doi.org/10.1130/0-8137-2388-4.449

Förste, C., Schmidt, R., Stubenvoll, R., Flechtner, F., Meyer, U., König, R., Neumayer, H., Biancale, R., Lemoine, J.-M., Bruinsma, S., Et al. (2008). The geoforschungszentrum potsdam/groupe de recherche de geodesie spatiale satellite-only and combined gravity field models: Eigen-gl04s1 and eigen-gl04c. *Journal of Geodesy*, *82*(6), 331–346.

Freymueller, J. T., Kellogg, J. N., & Vega, V. (1993). Plate motions in the north Andean region. *Journal of Geophysical Research*, *98*(B12), 853–863. https://doi.org/10.1029/93jb00520

Fullsack, P. (1995). An arbitrary lagrangian-eulerian formulation for creeping flows and its application in tectonic models. *Geophysical Journal International*, *120*(1), 1–23.

Gassmöller, R., Dannberg, J., Bangerth, W., Heister, T., & Myhill, R. (2020). On formulations of compressible mantle convection. *Geophysical Journal International*, *221*(2), 1264–1280.

Gerya, T. (2019). *Introduction to numerical geodynamic modelling*. Cambridge University Press.

Gleason, G. C., & Tullis, J. (1995). A flow law for dislocation creep of quartz aggregates determined with the molten salt cell. *Tectonophysics*, *247*(1-4), 1–23.

Goes, S., Govers, R., & Vacher, P. (2000). Shallow mantle temperatures under Europe from P and S wave tomography. *Journal of Geophysical Research: Solid Earth*, *105*(B5), 11153–11169. https://doi.org/10.1029/1999jb900300

Göğüş, O. H., & Pysklywec, R. N. (2008). Near-surface diagnostics of dripping or delaminating lithosphere. *Journal of Geophysical Research: Solid Earth*, *113*(11), 1–11. https://doi.org/10.1029/2007JB005123

Heister, T., Dannberg, J., Bangerth, W., & Gassm, R. (2017). High Accuracy Mantle Convection Simulation through Modern Numerical Methods . II : Realistic Models and Problems. *Geophysical Journal International*, *210*(2)arXiv arXiv:1702.05075v2, 833–851. https://doi.org/https://doi.org/10.1093/gji/ggx195

Heron, P., Pysklywec, R., Stephenson, R., & van Hunen, J. (2019). Deformation driven by deep and distant structures: Influence of a mantle lithosphere suture in the ouachita orogeny, southeastern united states. *Geology*, *47*(2), 147–150.

Houseman, G. A., Mckenzie, D. P., & Molnar, P. (1981). Convective instability of a thickened boundary layer and its relevance for the thermal evolution of continental convergent belts. *Journal of Geophysical Research*, *86*, 6115–6132.

Houseman, G. A., & Gemmer, L. (2007). Intra-orogenic extension driven by gravitational instability: Carpathian-pannonian orogeny. *Geology*, *35*(12), 1135–1138.

Houseman, G. A., & Molnar, P. (1997). Gravitational (rayleigh-taylor) instability of a layer with non-linear viscosity and convective thinning of continental lithosphere. *Geophysical Journal International*, *128*(1), 125–150.

Huismans, R., & Beaumont, C. (2007). Roles of lithospheric strain softening and heterogeneity in determining the geometry of rifts and continental margins. *Geological Society, London, Special Publications*, *282*(1), 111–138.

Hyndman, R., Currie, C., Mazzotti, S., & Frederiksen, A. (2009). Temperature control of continental lithosphere elastic thickness, te vs vs. *Earth and Planetary Science Letters*, *277*(3-4), 539–548.

Jin, Z.-M., Zhang, J., Green, H., & Jin, S. (2001). Eclogite rheology: Implications for subducted lithosphere. *Geology*, *29*(8), 667–670.

Jull, M., & Kelemen, P. B. (2001). On the conditions for lower crustal convective instability. *Journal of Geophysical Research: Solid Earth*, *106*(B4), 6423–6446. https://doi.org/10.1029/2000jb900357

Kachanov, L. M. (2004). *Fundamentals of the theory of plasticity*. Courier Corporation.

Karato, S.-i., & Wu, P. (1993). Rheology the upper mantle : Synthesis. *Science*, *260*(May), 771–778.

Katz, R. F., Spiegelman, M., & Langmuir, C. H. (2003). A new parameterization of hydrous mantle melting. *Geochemistry, Geophysics, Geosystems*, *4*(9), 1–19. https://doi.org/10.1029/2002GC000433

Kaus, B. J., & Becker, T. W. (2007). Effects of elasticity on the rayleigh–taylor instability: Implications for large-scale geodynamics. *Geophysical Journal International*, *168*(2), 843–862.

Kay, R., & Mahlburg Kay, S. (1993). Delamination and delamination magmatism. *Tectonophysics*, *219*(1-3), 177–189. https://doi.org/10.1016/0040-1951(93)90295-U

Krystopowicz, N. J., & Currie, C. A. (2013). Crustal eclogitization and lithosphere delamination in orogens. *Earth and Planetary Science Letters*, *361*, 195–207.

Leech, M. L. (2001). Arrested orogenic development: Eclogitization, delamination,and tectonic collapse. *Earth and Planetary Science Letters*, *185*(1-2), 149–159. https://doi.org/10.1016/S0012-821X(00)00374-5

Londoño, J. M., Vallejo, K., & Quintero, S. (2020). Detailed seismic velocity structure of the Caribbean and Nazca Plates beneath Valle Medio del Magdalena region of NE Colombia. *Journal of South American Earth Sciences*, *103*(August 2019). https://doi.org/10.1016/j.jsames.2020.102762

Mackwell, S. J., Zimmerman, M. E., & Kohlstedt, D. L. (1998). High-temperature deformation of dry diabase with application to tectonics on Venus. *Journal of Geophysical Research: Solid Earth*, *103*(1), 975–984. https://doi.org/10.1029/97jb02671

Mahlburg Kay, S., Coira, B., & Viramonte, J. (1994). Young mafic back arc volcanic rocks as indicators of continental lithospheric delamination beneath the Argentine Puna plateau, central Andes. *Journal of Geophysical Research*, *99*(B12), 24323–24339.

Montes, C., Bayona, G., Jaramillo, C., Ojeda, C., Molina, M., & Herrera, F. (2005). Uplift of the Sierra Nevada de Santa Marta and subsidence in the Cesar- Rancheria valley : Rigid-beam pivot model. *Sixth International Symposium of Andean Geodynamics*, (January), 520–523.

Montes, C., Guzman, G., Bayona, G., Cardona, A., Valencia, V., & Jaramillo, C. (2010). Clockwise rotation of the santa marta massif and simultaneous paleogene to neogene deformation of the plato-san jorge and cesar-rancheria basins. *Journal of South American Earth Sciences*, *29*(4), 832–848.

Müller, R. D., Royer, J. Y., Cande, S. C., Roest, W. R., & Maschenkov, S. (1999). Chapter 2 New constraints on the late cretaceous/tertiary plate tectonic evolution of the caribbean. *Sedimentary Basins of the World*, *4*(100), 33–59. https://doi.org/10.1016/S1874-5997(99)80036-7

Naliboff, J. B., Buiter, S. J., Péron-Pinvidic, G., Osmundsen, P. T., & Tetreault, J. (2017). Complex fault interaction controls continental rifting. *Nature communications*, *8*(1), 1–9.

Neil, E. A., & Houseman, G. A. (1999). Rayleigh-taylor instability of the upper mantle and its role in intraplate orogeny. *Geophysical Journal International*, *138*(1), 89–107.

Pindell, J., & Dewey, J. F. (1982). Permo-Triassic reconstruction of western Pangea and the evolution of the gulf of Mexico/Caribbean region. *America*, *1*(2), 179–211.

Pindell, J., Kennan, L., Maresch, W. V., Draper, G., & Higgs, R. (2005). Plate-kinematics and crustal dynamics of circum-Caribbean arccontinent interactions: Tectonic controls on basin development in Proto-Caribbean margins, *2394*(01), 7–52. https://doi.org/10.1130/2005.2394(01).

Pindell, J., Kennan, L., Stanek, K. P., Maresch, W. V., & Draper, G. (2006). Foundations of Gulf of Mexico and Caribbean evolution: Eight controversies resolved. *Geologica Acta*, *4*(1-2), 303–341. https://doi.org/10.1344/105.000000371

Poveda, E., Julià, J., Schimmel, M., & Perez-Garcia, N. (2018). Upper and Middle Crustal Velocity Structure of the Colombian Andes From Ambient Noise Tomography: Investigating Subduction-Related Magmatism in the Overriding Plate. *Journal of Geophysical Research: Solid Earth*, *123*(2), 1459–1485. https://doi.org/10.1002/2017JB014688

Pysklywec, R. N., & Cruden, A. R. (2004). Coupled crust-mantle dynamics and intraplate tectonics: Two-dimensional numerical and three-dimensional analogue modeling. *Geochemistry, Geophysics, Geosystems*, *5*(10).

Quandt, D., Trumbull, R. B., Altenberger, U., Cardona, A., Romer, R. L., Bayona, G., Ducea, M., Valencia, V., Vásquez, M., Cortes, E., & Guzman, G. (2018). The geochemistry and geochronology of Early Jurassic igneous rocks from the Sierra Nevada de Santa Marta, NW Colombia, and tectono-magmatic implications. *Journal of South American Earth Sciences*, *86*(November 2017), 216–230. https://doi.org/10.1016/j.jsames.2018.06.019

Quintero, W., Campos-Enriquez, O., & Hernandez, O. (2019). Curie point depth, thermal gradient, and heat flow in the Colombian Caribbean (northwestern South America). *Geothermal Energy*, *7*(1). https://doi.org/10.1186/s40517-019-0132-9

Ramírez, D. A., Correa-Martínez, A. M., Zapata-Villada, J. P., & Rodríguez, G. (2020). Tectono-magmatic implications of the Jurassic volcanic and volcanoclastic record of the Santa Marta Massif (Colombia). *Journal of South American Earth Sciences*, *104*(September), 102866. https://doi.org/10.1016/j.jsames.2020.102866

Rose, I., Buffett, B., & Heister, T. (2017). Stability and accuracy of free surface time integration in viscous flows. *Physics of the Earth and Planetary Interiors*, *262*, 90–100. https://doi.org/10.1016/j.pepi.2016.11.007

Salazar, S. S., Muñoz, Y., & Ospino, A. (2017). Analysis of geothermal energy as an alternative source for electricity in Colombia. *Geothermal Energy*, *5*(1). https://doi.org/10.1186/s40517-017-0084-x

Saleeby, J., Le Pourhiet, L., Saleeby, Z., & Gurnis, M. (2012). Epeirogenic transients related to mantle lithosphere removal in the southern Sierra Nevada region, California, part I: Implications of thermomechanical modeling. *Geosphere*, *8*(6), 1286–1309. https://doi.org/10.1130/GES00746.1

Sanchez, J., & Mann, P. (2015). Integrated structural and basinal analysis of the Cesar–Rancheria Basin, Colombia: Implications for its tectonic history and petroleum systems. *AAPG Memoir*, *108*, 431–470. https://doi.org/10.1306/13531945M1083648

Sanchez-Rojas, J., & Palma, M. (2014). Crustal density structure in northwestern south america derived from analysis and 3-d modeling of gravity and seismicity data. *Tectonophysics*, *634*, 97–115.

Schubert, G., Turcotte, D. L., & Olson, P. (2001). *Mantle convection in the earth and planets*. Cambridge University Press.

Sobolev, S. V., Zeyen, H., Stoll, G., Werling, F., Altherr, R., & Fuchs, K. (1996). Upper mantle temperatures from teleseismic tomography of French Massif Central including effects of composition, mineral reactions, anharmonicity, anelasticity and partial melt. *Earth and Planetary Science Letters*, *139*(1-2), 147–163. https://doi.org/10.1016/0012-821x(95)00238-8

Spacesystems, & ASTER Science Team. (2019). ASTER global digital elevation model v003 [data set] [NASA EOSDIS Land Processes DAAC. Accessed 2021-01-07] from https://doi.org/10.5067/ASTER/ASTGTM.003.

Spikings, R., Cochrane, R., Villagomez, D., Van der Lelij, R., Vallejo, C., Winkler, W., & Beate, B. (2015). The geological history of northwestern South America: From Pangaea to the early collision of the Caribbean Large Igneous Province (290-75 Ma). *Gondwana Research*, *27*(1), 95–139. https://doi.org/10.1016/j.gr.2014.06.004

Sun, S.-S. (1982). Chemical composition and origin of the earth's primitive mantle. *Geochimica et Cosmochimica Acta*, *46*(2), 179–192.

Syracuse, E. M., Maceira, M., Prieto, G. A., Zhang, H., & Ammon, C. J. (2016). Multiple plates subducting beneath Colombia, as illuminated by seismicity and velocity from the joint inversion of seismic and gravity data. *Earth and Planetary Science Letters*, *444*, 139–149. https://doi.org/10.1016/j.epsl.2016.03.050

Taboada, A., Rivera, L. A., Fuenzalida, A., Cisternas, A., Philip, H., Bijwaard, H., Olaya, J., & Rivera, C. (2000). Geodynamics of the northern Andes. *Tectonics*, *19*(5), 787–813.

Talwani, M., Worzel, J. L., & Landisman, M. (1959). Rapid gravity computations for two-dimensional bodies with application to the mendocino submarine fracture zone. *Journal of geophysical research*, *64*(1), 49–59.

Tassara, A., Swain, C., Hackney, R., & Kirby, J. (2007). Elastic thickness structure of South America estimated using wavelets and satellite-derived gravity data. *Earth and Planetary Science Letters*, *253*(1-2), 17–36. https://doi.org/10.1016/j.epsl.2006.10.008

Telford, W. M., Geldart, L., & Sheriff, R. (1990). *Applied geophysics* (2nd ed., Vol. 69). Cambridge University press.

Tschanz, C. M., Marvin, R. F., Cruz, J. B., Menhnert, H. H., & Cebula, G. T. (1974). Geologic Evolution of the Sierra Nevada de Santa Marta, Northeastern Colombia. *Geological Society of America Bulletin*, *85*(2), 273–284. https://doi.org/https://doi.org/10.1130/0016-7606(1974)85⟨273:GEOTSN⟩2.0.CO;2

Van Der Hilst, R., & Mann, P. (1994). Tectonic implications of tomographic images of subducted lithosphere beneath northwestern South America. *Geology*, *22*(5), 451–454. https://doi.org/10.1130/0091-7613(1994)022⟨0451:TIOTIO⟩2.3.CO;2

van Wijk, J., van Hunen, J., & Goes, S. (2008). Small-scale convection during continental rifting: Evidence from the Rio Grande rift. *Geology*, *36*(7), 575–578. https://doi.org/10.1130/G24691A.1

Vargas, C. A. (2020). Subduction Geometries in Northwestern South America. In J. T. Gómez & A. O. Pinilla-Pachon (Eds.), *The geology of colombia* (pp. 397–422). Bogotá, Servicio Geológico Colombiano, Publicaciones Geológicas Especiales 38. https://doi.org/https://doi.org/10.32685/pub.esp.38.2019.11

Vargas, C. A., Alfaro, C., Briceño, L. A., Alvarado, I., & Quintero, W. (2009). Mapa geotérmico de colombia - 2009 [Paper in Spanish] Geothermal Map of Colombia-2009. *Asociación Colombiana de Geólogos y Geofisicos del Petróleo (ACGGP)*, (3), 1–5.

Villagómez, D., Spikings, R., Mora, A., Guzmán, G., Ojeda, G., Cortés, E., & Lelij, R. V. D. (2011). Vertical tectonics at a continental crust - oceanic plateau plate boundary zone : Fission track thermochronology of the Sierra Nevada de Santa Marta , Colombia. *Tectonics*, *30*(4). https://doi.org/10.1029/2010TC002835

Wang, H., & Currie, C. A. (2017). Crustal deformation induced by mantle dynamics: Insights from models of gravitational lithosphere removal. *Geophysical Journal International*, *210*(2), 1070–1091. https://doi.org/10.1093/gji/ggx209

Wang, H., Currie, C. A., & Zhan, Y. (2014). Surface Expressions of Rayleigh-Taylor Instability in Continental Interiors. *Acta Geologica Sinica - English Edition*, *88*(3), 1004–1016. https://doi.org/https://doi.org/10.1111/1755-6724.12253

Wang, Y. F., Zhang, J. F., Jin, Z. M., & Green, H. W. (2012). Mafic granulite rheology: Implications for a weak continental lower crust. *Earth and Planetary Science Letters*, *353-354*, 99–107. https://doi.org/10.1016/j.epsl.2012.08.004

Warren, C. J., Beaumont, C., & Jamieson, R. A. (2008). Deep subduction and rapid exhumation: Role of crustal strength and strain weakening in continental subduction and ultrahigh-pressure rock exhumation. *Tectonics*, *27*(6).

Zhang, J., & Green, H. W. (2007). Experimental investigation of eclogite rheology and its fabrics at high temperature and pressure. *Journal of Metamorphic Geology*, *25*(2), 97–115. https://doi.org/10.1111/j.1525-1314.2006.00684.x

Appendix

A Tests of Advection Mechanisms

A1. Model Results

This section includes the results of models N4 and N5 which are supplementary models for set N in chapter 3, testing the effect of the numerical advection mechanism with a higher crustal viscosity ($\eta_{crust} = 10^{25}$ Pa·s). Model N4 (Figure A1*a*) uses compositional fields in ASPECT, and model N5 (Figure A1*b*) uses active particles in ASPECT.

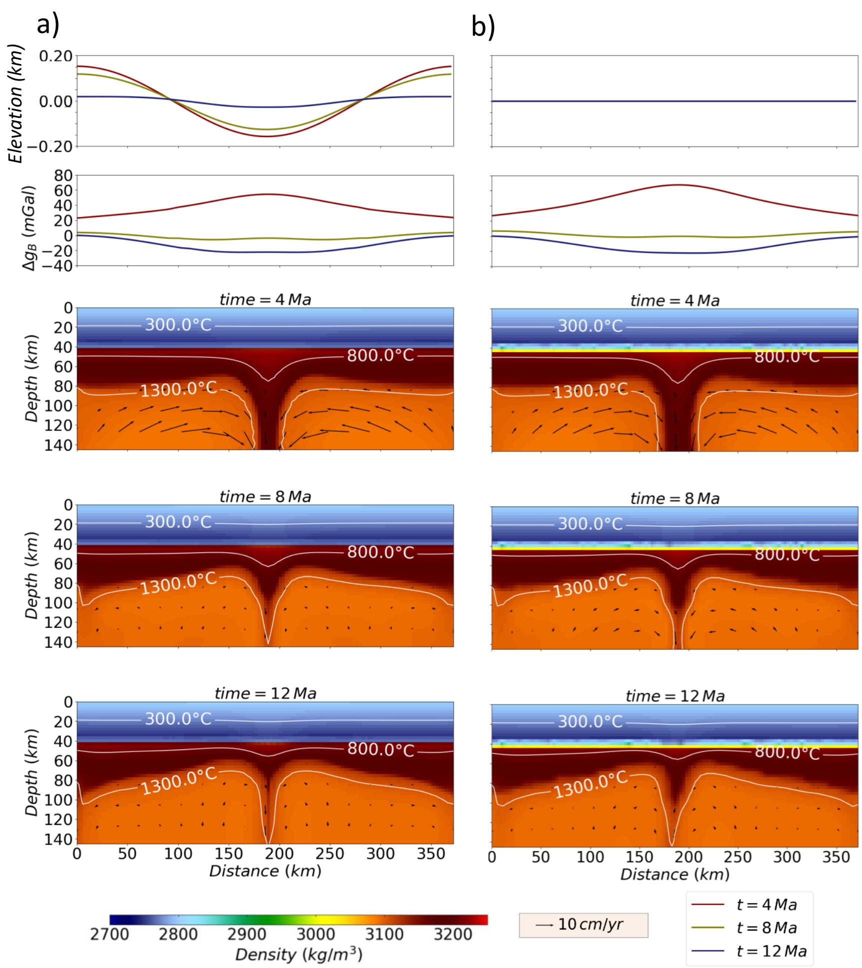

Figure A1: Model results for preliminary drips with high crustal viscosity ($10^{25} Pa \cdot s$) using (a) the solution of the advection equation over compositional fields in the ASPECT code (model N4), and (b) the active particles advection method in the ASPECT code (model N5). Plots for each model include profiles of surface elevation (top plot), Bouguer gravity anomaly Δg_B (second plot), and cross-sections of density structure (lower three plots), at 4, 8 and 12 Ma, showing the evolution of the drip. The surface in (b) is fixed because the use of a free surface with active particles is not supported in ASPECTv2.2.0. so the top boundary has free slip conditions.

A2. Surface Observables

This section shows the evolution of surface observables of elevation and Bouguer gravity anomaly (Δg_B) for models N4 and N5 (Figure A2).

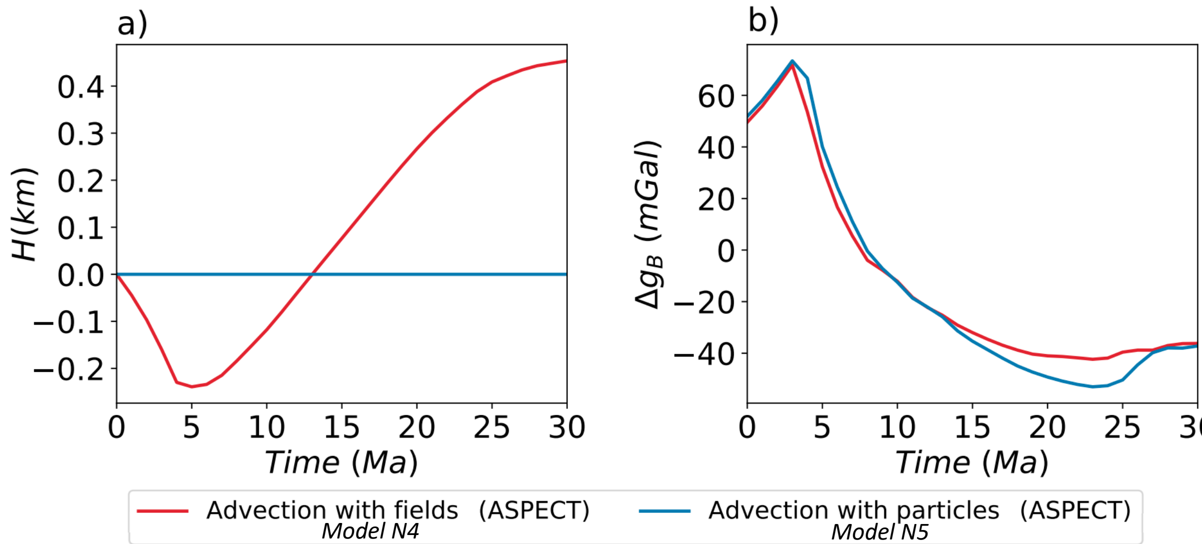

Figure A2: Time variation of surface observables, averaged over a 100 km width above the perturbation for models N4 and N5 including (a) surface elevation (H), and (b) Bouguer gravity anomaly (Δg_B). Topography is not reported for model N5 because the use of a free surface with active particles is not supported in ASPECTv2.2.0.

B Model Plots for Set F

This section includes individual model Figures for modelling set F (discussed in section 5.3.9). It consists of a group of models that systematically test the effects of variations in initial crustal thickness and lateral compression rates.

B1. No Lateral Compression

Models in Figure B1 show the effect of crustal root thickness (R) when there is no lateral compression.

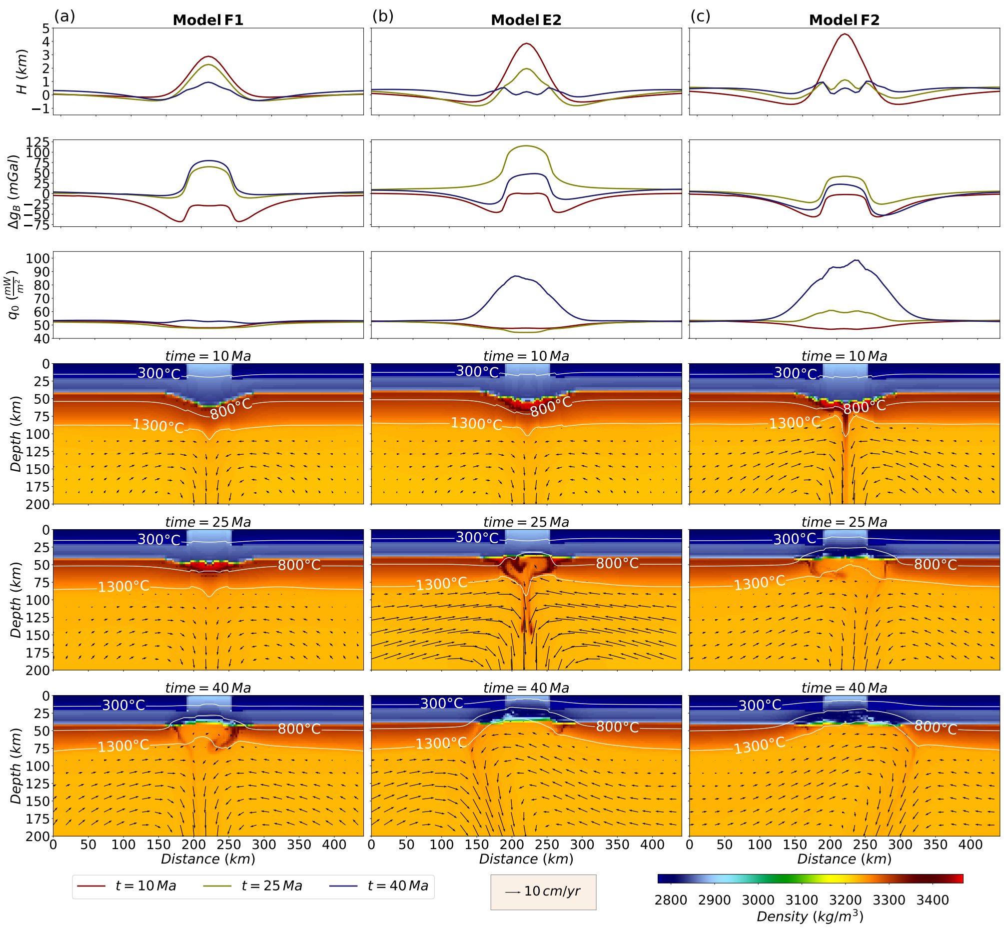

Figure B1: Modelling results for (a) model F1 (R = 20 km), (b) model E2 (R = 30 km) (As a reference) and (c) model F2 (R = 40 km), including snapshots of density structures and profiles of surface elevation (H), Bouguer gravity anomaly (Δg_B) and surface heat flow (q_0), at times before, during and after the main lithosphere removal episode. These models explore the effect of different crustal root amplitudes (R) when there is no lateral compression.

B2. Lateral Compression at 0.5 mm/yr

Models in Figure B2 show the effect of crustal root thickness (R) with a lateral compression rate of 0.5 mm/yr.

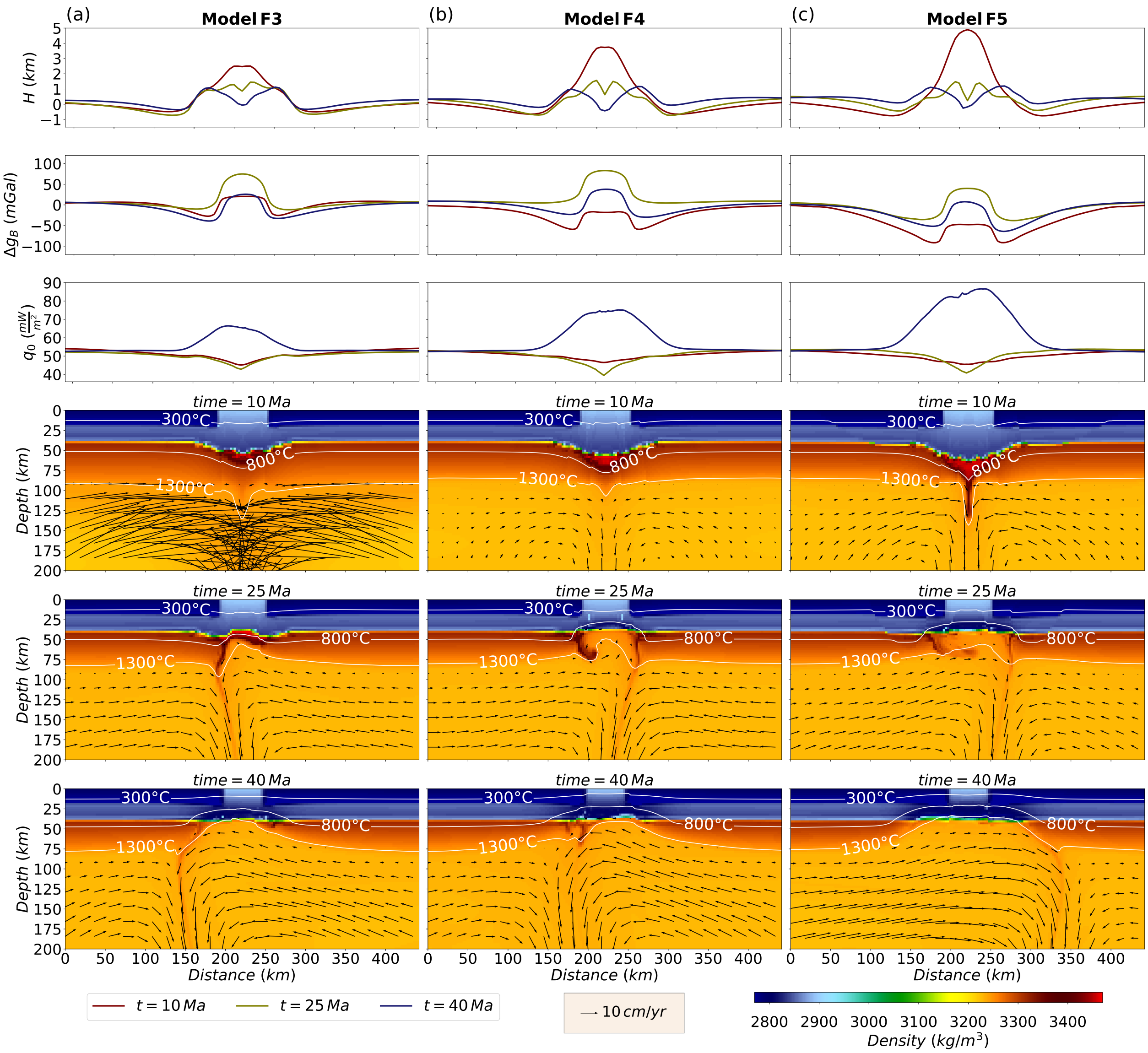

Figure B2: Modelling results for (a) model F3 ($R = 20$ km), (b) model F4 ($R = 30$ km) and (c) model F5 ($R = 40$ km), including snapshots of density structures and profiles of surface elevation (H), Bouguer gravity anomaly (Δg_B) and surface heat flow (q_0), at times before, during and after the main lithosphere removal episode. These models explore the effect of different crustal root amplitudes (R) when the lateral compression rate is of 0.5mm/yr.

B3. Lateral Compression at 1.0 mm/yr

Models in Figure B3 show the effect of crustal root thickness (R) with a lateral compression rate of 1.0 mm/yr.

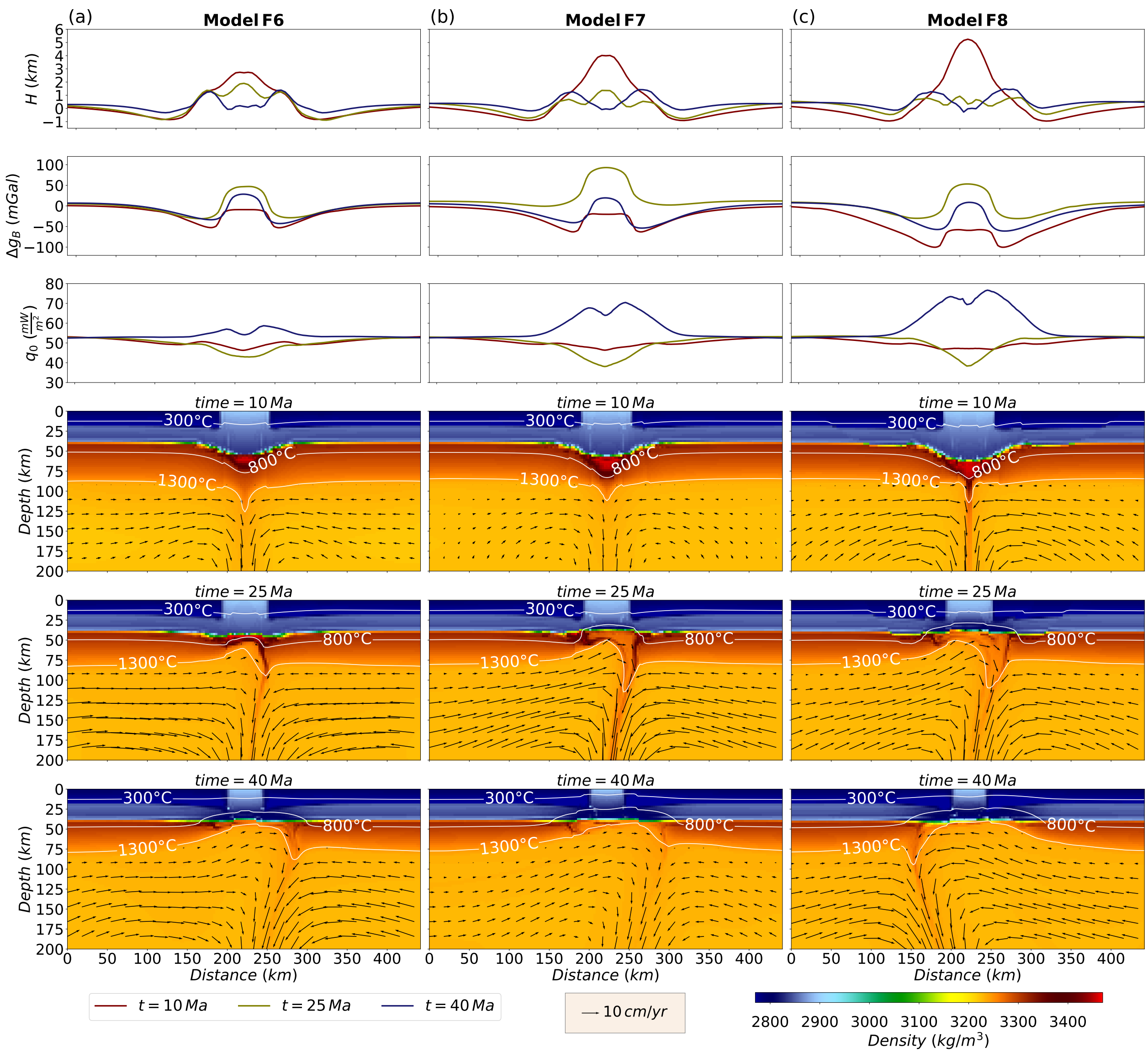

Figure B3: Modelling results for (a) model F6 ($R = 20$ km), (b) model F7 ($R = 30$ km) and (c) model F8 ($R = 40$ km), including snapshots of density structures and profiles of surface elevation (H), Bouguer gravity anomaly (Δg_B) and surface heat flow (q_0), at times before, during and after the main lithosphere removal episode. These models explore the effect of different crustal root amplitudes (R) when the lateral compression rate is of 1.0mm/yr.

B4. Lateral Compression at 1.5 mm/yr

Models in Figure B4 show the effect of crustal root thickness (R) with a lateral compression rate of 1.5 mm/yr.

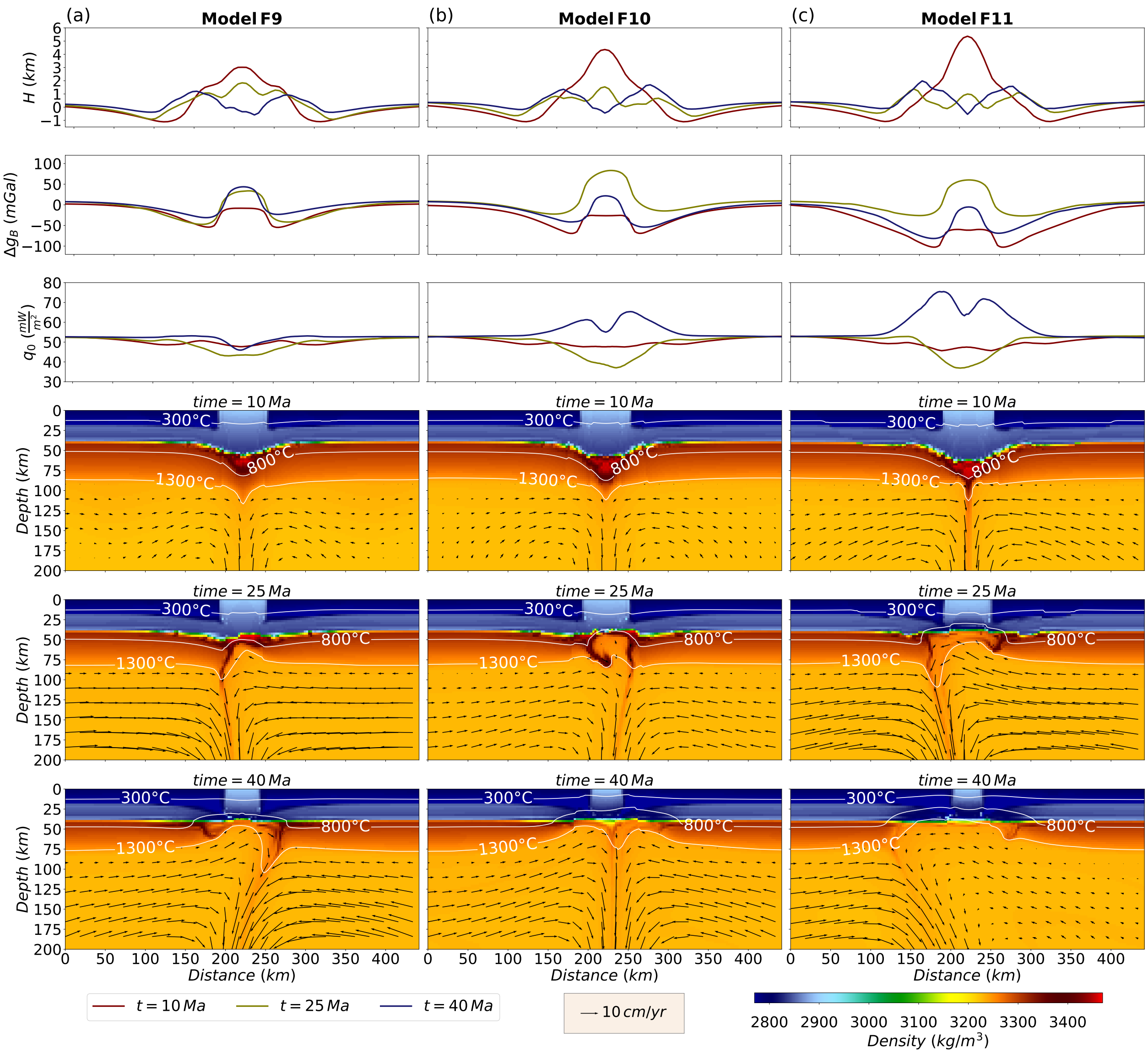

Figure B4: Modelling results for (a) model F9 ($R = 20$ km), (b) model F10 ($R = 30$ km) and (c) model F11 ($R = 40$ km), including snapshots of density structures and profiles of surface elevation (H), Bouguer gravity anomaly (Δg_B) and surface heat flow (q_0), at times before, during and after the main lithosphere removal episode. These models explore the effect of different crustal root amplitudes (R) when the lateral compression rate is of 1.5mm/yr.

B5. Evolution of Surface Observables for Set F

This section includes Figure B5, which shows the evolution of surface elevation, Bouguer gravity anomaly (Δg_B), and surface heat flow for set F.

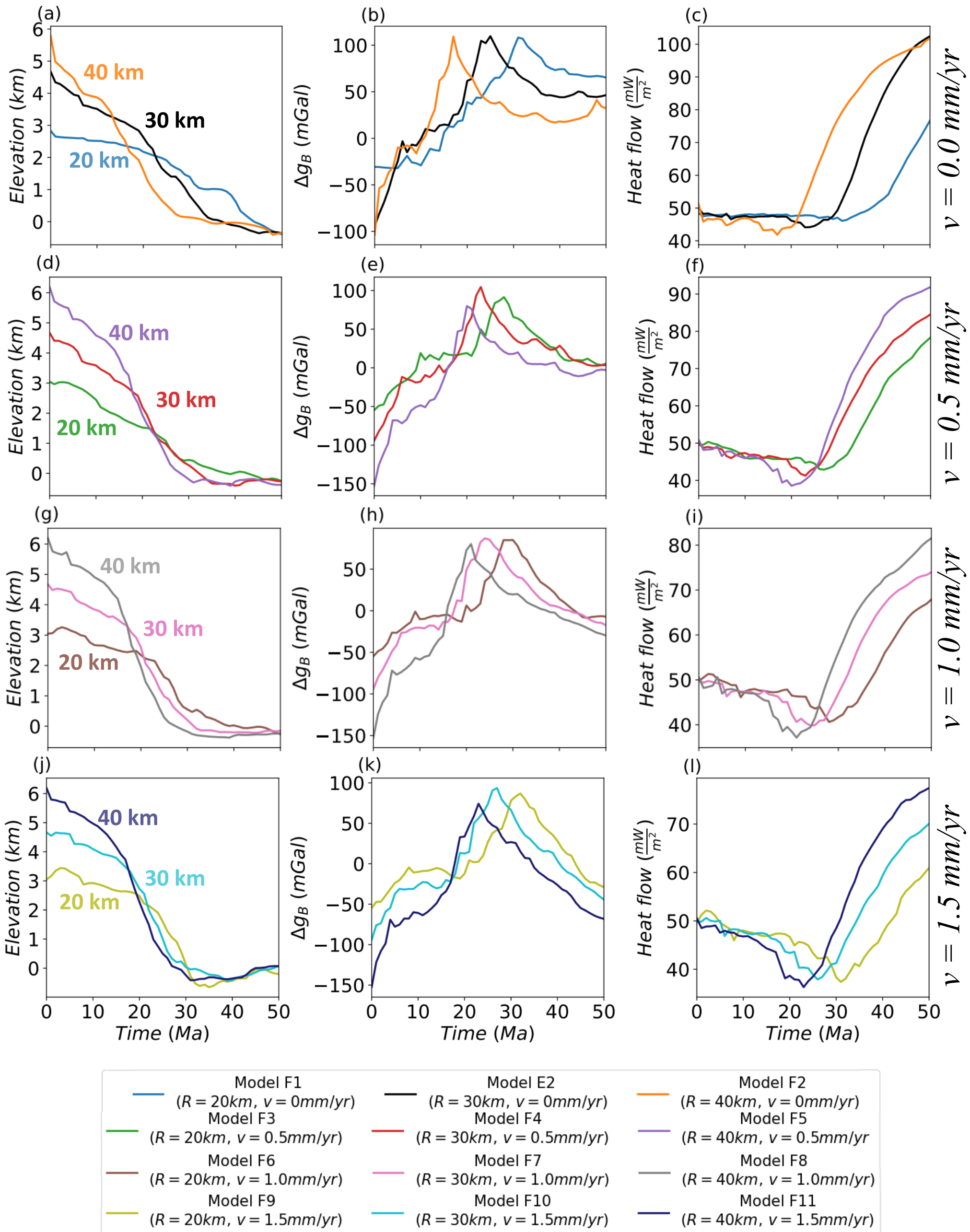

Figure B5: Time variation of surface observables, averaged over a 50 km width centred in the mountain, for modelling set F, testing lateral compression rates (v) and different crustal root amplitudes (R). Results of model E2 are shown as a reference (black). (a,d,g,j) Surface elevation. (b,e,h,k) Bouguer gravity anomaly (Δg_B). (c,f,i,l) Surface heat flow.